OXFORD UNIVERSITY PRESS | The IMA Journal of Applied Mathematics

Incipient mixing by Marangoni effects in slow viscous flow of two immiscible fluid layers

Journal:	*The IMA Journal of Applied Mathematics*
Manuscript ID:	IMAMAT-2014-176.R1
Manuscript Type:	Original Papers
Date Submitted by the Author:	n/a
Complete List of Authors:	penfold, robert; institute of food research, food and health programme rickett, lydia; sainsbury laboratory, Blyth, Mark; University of East Anglia, Mathematics Purvis, Richard; University of East Anglia, School of Mathematics Cooker, Mark; University of East Anglia, Mathematics
Keyword:	liquid-liquid interface, linear stability analysis, generalized eigenvalue problem, collocation method, avoided crossing, exceptional point

IMA Journal of Applied Mathematics (2014) Page 1 of 37
doi:10.1093/imamat/dri017

Incipient mixing by Marangoni effects in slow viscous flow of two immiscible fluid layers

LYDIA RICKETT[1,3], ROBERT PENFOLD[2], MARK G. BLYTH[1], RICHARD PURVIS[1],
MARK J. COOKER[1]

[1] *School of Mathematics, University of East Anglia, Norwich NR4 7TJ, UK.*

[2] *Institute of Food Research, Norwich Research Park, Norwich NR4 7UA, UK.*

[3] *The Sainsbury Laboratory, Norwich Research Park, Norwich NR4 7UH, UK.*

[Received on October 28, 2014]

[Received on 28 October 2014]

Ignoring inertia, a deformable interface separating two fluid films is considered, subject to nonuniform tension driven by the solutal Marangoni effect in the presence of a scalar concentration field. Detailed description of adsorption kinetics is abrogated by a simple ansatz directly relating interfacial tension and bulk solute concentration. Consequently, the formal mathematical treatment and some of the results share features in common with the Rayleigh–Bénard–Marangoni thermocapillary problem. Normal mode perturbation analysis in the limit of small interface deformations establishes the existence of unstable response for low wavenumber excitation. In the classification of Cross and Hohenberg (1993, Rev. Mod. Phys., **65**, 851–1112), both Type-I and Type-II behaviour are observed. By considering the zero wavenumber situation exactly, it is proved that all eigenvalues are purely imaginary with non-positive imaginary part; hence, a Type-III instability is not possible. For characteristic timescales of mass diffusion much shorter than the relaxation time of interfacial fluctuations (infinite crispation number): the response growth rate is obtained explicitly; only a single excitation mode is available and a complete stability diagram is constructed in terms of the relevant control parameters. Otherwise, from a quiescent base state, an infinite discrete spectrum of modes is observed that exhibit avoided crossing and switching phenomena, as well as exceptional points where stationary state pairs coalescence into a single oscillatory standing wave pattern. A base state plane Poiseuille flow, driven by an external pressure gradient, generally exaggerates the response: growth rates of instabilities are enhanced and stable decay is further suppressed with increasing base flow speed; but the inherent symmetry breaking destroys stationary and standing wave response. Results are obtained in this most general situation by implementing a numerical Chebyshev collocation scheme. The model was motivated by hydrodynamic processes supposed to be involved in gastric digestion of humans.

Keywords: liquid-liquid interface, Gibbs elasticity, Stokes flow, linear stability analysis, generalised eigenvalue problem, collocation method, avoided crossing, exceptional point

1. Introduction

To understand the bio-availability and delivery of nutrients and medicines from processed foods and pharmaceutical preparations, a detailed mechanistic model of digestion is needed. The human gastrointestinal tract, from the mouth to the anus, is a coupled sequence of specialized organs, each of which has a distinctive digestive function. In particular, the stomach performs biochemical tasks involving complex salts, strong mineral acid and proteolytic enzymes to produce chyme (soft solid, partially digested food) (Kong & Singh, 2008). The stomach also offers a prominent line of defense against pathogenic microorganisms, but more importantly it is the primary site of mechanical action where ingested material is subjected to a complicated unsteady shear flow, dominated by frictional dissipation rates with relatively negligible inertial forces (Pal et al., 2007). For the purpose of developing a simple mathematical model of this action, we shall adopt here the following working definition: “digestion” means the incipient mixing associated with the linear temporal instability of the interface between two immiscible liquids. Agitated away from equilibrium, the morphological evolution of interfacial patterns and the dynamics of viscous interfacial flow are driven by the physical mechanisms of heterogeneous mixing (Pozrikidis, 1997). Despite the absence of inertia-driven turbulence, a combination of chaotic advection and diffusion can promote mixing in Stokes flows (Thiffeault et al., 2011) that are governed by time-reversible equations of motion. With deformable boundaries, a “geometric” mixing mechanism has also been suggested exploiting anholonomy of the system so that flow variables do not recover their original values on negotiating a closed loop in the parameter space (Cartwright et al., 2012).

Developed at the Institute of Food Research (UK), the Dynamic Gastric Model (DGM) is an in-vitro system that automatically simulates human digestion for the first time from a realistic physiological perspective by accounting for the physical, mechanical and biochemical environment experienced in the stomach (Mercuri et al., 2011). To establish a reliable predictive relationship between DGM output and physiological stomach behaviour, some quantitative analysis of the device function is required. Motivated by this need, the present work establishes conditions relevant to the hydrodynamics of digestion insofar as they may lead to mixing and may be a precursor for turbulence.

The application of Orr-Sommerfeld perturbation analysis (Drazin, 2002; Charru, 2011) for parallel fluid flows has a rich, mature and growing literature. Linear response theory leads to a generalised eigenvalue problem which has a nontrivial solution only if the temporal and spatial frequencies are linked by a dispersion relation. In the most general problem, the large number of control parameters (at least six) spawns a host of potentially unstable modes governed by diverse mechanisms of different physical origin. The viscosity-induced interfacial mode instability of two superposed and bounded fluid layers was first discussed by Yih (1967). Subsequently designated as “the thin-layer effect” (Hooper, 1985), a spatially confined film of more viscous fluid is unstable to long waves at all positive Reynolds numbers. For the converse situation of a confined film of lower viscosity, the flow is stable in the limit of weak interfacial tension (Renardy, 1987). The thin-layer effect is also observed for multiple fluid layer configurations in plane Poiseuille flow (Anturkar et al., 1990). Neglecting interfacial tension entirely, Charru & Hinch (2000) have neatly rationalised Yih’s small wavenumber analysis together with a second instability at low Reynolds number and high frequency (Hooper & Boyd, 1983) that is present between two shearing unbounded fluids. This latter phenomenon has been confirmed by numerical volume-of-fluid studies in the nonlinear regime (Coward et al., 1997; Li & Renardy, 2000) and might be regarded as a viscous analogue of the Kelvin-Helmholtz instability. Hinch (1984) proposed a detailed mechanism and concluded that some small inertial contribution is necessary in order that advection by the main shear flow can drive the disturbance vorticities in each fluid out-of-phase and so allow the induced velocity fields to amplify the interfacial perturbation. By considering the energy budget in low Reynolds number expansions, Albert & Charru (2000) have confirmed that interfacial instability arises from inertia influencing disturbances, at both small and large wavenumber.

It is perhaps because of this conclusion that the stability of superposed liquid layers in strict Stokes flow (at zero Reynolds number) has received far less attention. Pozrikidis (1997) has implemented a boundary integral method to investigate the interfacial behaviour subject to *finite* amplitude perturbations. He showed that sufficiently large amplitude disturbances cause permanent interfacial deformation with a morphology that depends sensitively on the viscosity ratio. In a very recent study of

Poiseuille flow of layered *miscible* fluids in the Stokes regime, Talon & Meiburg (2011) have reported that diffusion has a destabilising effect very similar to that induced by inertia at finite Reynolds number. Miscibility influences stability by extending the interface into a three dimensional domain with finite width and is typically modelled (Sahu et al., 2009a,b) by a smooth viscosity distribution coupled to a convective-diffusion equation for a scalar concentration field of "friction inducing solute". Formally, this is very similar to our present treatment of Marangoni effects (Johnson & Narayanan, 1997) where spatial variations of interfacial tension are produced, for example, by a temperature field or by a nonuniform distribution of surfactants. This artifice will simplify the differential geometry and obviate a detailed chemical kinetic mechanism of the interfacial adsorption process (Palmer & Berg, 1972; Reichenbach & Linde, 1981; Slavtchev et al., 1998, 2006) that is highly complicated in typical applications, notably the digestion mechanism of the stomach. In consequence too, we note a formal correspondence between this approach and the analysis of thermal Marangoni effects. As a rich example of spontaneous pattern formation in nonequilibrium dynamical systems, the classical Rayleigh–Bénard convective instability (Koschmieder, 1974) of a single fluid layer subject to a transverse temperature gradient has been long studied (Normand et al., 1977) but continues to attract attention (Bodenschatz et al., 2000). By superposing a second layer of immiscible fluid, many new and qualitatively different phenomena arise from the competition of individual layer instabilities (Andereck et al., 1998). By assuming "exchange of stabilities" (Drazin & Reid, 2004), a linear stability analysis of the thermal Marangoni effect was tackled by Zeren & Reynolds (1972), and subsequently extended by Zhao et al. (1995) to account for interfacial deformation. Rasenat et al. (1989) completed a more general treatment to demonstrate that steady convection could be driven either by buoyancy or by Marangoni forces.

Frenkel and Halpern (Frenkel & Halpern, 2002; Halpern & Frenkel, 2003) have identified a new non-inertial interfacial instability which was investigated further by Blyth & Pozrikidis (2004a). This is driven by the Marangoni traction that arises from the presence of adsorbed surfactant and velocity shear in two-layer planar flows of Couette-Poiseuille type. A physical mechanism is also proposed where the imbalance of interfacial tension drives flow from troughs to peaks and reinforces the deformation. Notably, in contrast to the interfacial mode of inertial flows, a viscosity jump is not required for instability. Moreover, explicit analytic expressions are obtained for the wave speed and growth rate. Corresponding phenomena are also predicted for surfactant-laden interfaces in gravity driven flow on an inclined plane (Gao & Lu, 2007; Blyth & Pozrikidis, 2004b) and for radially stratified films in concentric two-fluid Taylor–Couette flow (Peng & Zhu, 2010), where there is a complicated interaction of instability mechanisms. The effect of inertia coupled with the Marangoni instability has also been studied by normal-mode analysis (Frenkel & Halpern, 2005; Blyth & Pozrikidis, 2004c) and numerical methods (Pozrikidis, 2004) applicable beyond the linear regime. A wider range of unstable wavenumbers is the chief consequence. After observing that linear analysis of Stokes flow has established insoluble surfactant is unable to destabilise a sheared interface between two semi-infinite fluids, Pozrikidis & Hill (2011) have recently questioned the necessity of a bounded fluid domain to realise the Marangoni instability. They concluded that one wall is required to engage the Marangoni mechanism, but the presence of a second wall may stabilise the flow.

Section 2 sets out the physical arguments to establish the appropriate governing equations and boundary conditions. A full mathematical treatment is developed in Section 3, culminating in a dispersion relation. Two special cases are considered in Section 4 before the general solution is presented in Section 5. Results are collected and discussed in Section 6, and the paper concludes in Section 7 with some perspective on applications and future work. Section 9 is an appendix containing comprehensive mathematical details and formal proofs of some results in the text.

2. Mathematical model specification

2.1 *Coordinate frame, constitutive relation and nondimensionalisation*

Under isothermal conditions, consider the unidirectional creeping flow of two incompressible Newtonian fluids (indexed by the labels $j = 1,\, 2$), driven by a constant axial pressure gradient $-\tilde{G}_p$ (with $\tilde{G}_p \geqslant 0$) through an infinite channel bounded by stationary parallel walls fixed at separation $2\tilde{h}$. It is natural to adopt a Cartesian system $(\tilde{x},\, \tilde{y},\, \tilde{z})$ with the longitudinal coordinate $-\infty < \tilde{x} < \infty$ and the transverse coordinate $-\tilde{h} \leqslant \tilde{y} \leqslant \tilde{h}$. Unit vectors in each coordinate direction are denoted $\mathbf{i}$, $\mathbf{j}$ and $\mathbf{k}$, respectively. Interfacial disturbances are supposed small and are manifest in two spatial dimensions only so that all the relevant dynamical quantities are independent of the lateral coordinate $\tilde{z}$. The fluid labelled 1 is confined between the lower wall at $\tilde{y} = -\tilde{h}$ and the interface, whose flat equilibrium position is $\tilde{y} = \tilde{\alpha}$ where $\tilde{\alpha}$ is a constant. Each of the bulk fluids is characterised by a dynamic viscosity $\tilde{\mu}_j$ and a diffusion coefficient $\tilde{D}_j$ for solute species. We observe the Boussinesq approximation and suppose that all $\tilde{\mu}_j$ and $\tilde{D}_j$ are constant and remain unaffected by variations in bulk solute concentration. Furthermore, there is no stratification in mass density $\tilde{\rho}_1 = \tilde{\rho}_2 = \tilde{\rho}$ and the system is assumed free of external body forces, so buoyancy effects are neglected.

The deformable interface located at $\tilde{y} = \tilde{\eta}\left(\tilde{x},\, \tilde{t}\right)$, is a free material boundary with a Newtonian response: explicit effects of interfacial rheology are neglected. Nevertheless, the associated equilibrium interfacial tension is a sensitive function of the local environment, with a complicated dependence on temperature and the presence of solutes in either of the adjoining fluid phases. Spatial inhomogeneities of the interfacial tension can arise from fluctuations in the physical adsorption of surfactants and advective interfacial transport, or from localised chemical activity at the interface. For simplicity, we posit a scalar field $\tilde{\chi}_j = \tilde{\chi}_j\left(\tilde{x},\, \tilde{y},\, \tilde{t}\right)$ to represent the concentration of some surface active species dissolved in fluid j, that is subject to advection and diffusion in the three-dimensional bulk phases only. It is here that our ansatz deviates from other studies of the solutal Marangoni effect (Li & Pozrikidis, 1997; Frenkel & Halpern, 2002; Halpern & Frenkel, 2003; Frenkel & Halpern, 2005; Blyth & Pozrikidis, 2004a; Pozrikidis, 2004; Blyth & Pozrikidis, 2004c; Gao & Lu, 2007; Pozrikidis & Hill, 2011) where the surfactant is assumed insoluble in bulk, confined strictly to the interface and governed by an appropriate two-dimensional transport equation.

We undertake a temporal linear stability analysis of steady base state flow with a uniform interfacial tension and concentration fields

$$\tilde{\chi}_j^{(0)} = \tilde{\chi}_j^{(0)}\left(\tilde{y}\right) \ \ , \ \ j \in \{1,\, 2\} \ \ , \tag{2.1}$$

that depend only on the transverse coordinate across the channel. For small perturbations of the base state flow, the change in the interfacial tension is proportional to the induced departure of the bulk concentration from $\tilde{\chi}_j^{(0)}$, and proportional to a contribution that arises from displacement of the interface within the static field. We adopt the linear interfacial equation of state

$$\tilde{\gamma} = \tilde{\gamma}\left(\tilde{x},\, \tilde{y},\, \tilde{t}\right) = \tilde{\gamma}_0 \left(1 - \mathrm{Mg} \times \left(\frac{\tilde{\chi}_j\left(\tilde{x},\, \tilde{y},\, \tilde{t}\right) - \tilde{\chi}_j^{(0)}\left(\tilde{\alpha}\right)}{\tilde{\chi}_2^{(0)}\left(\tilde{h}\right) - \tilde{\chi}_1^{(0)}\left(-\tilde{h}\right)}\right)\right) \ \ , \tag{2.2}$$

with the understanding that physical meaning is attached to this field $\tilde{\gamma}$ only for $\tilde{y} = \tilde{\eta}$. The dimensionless interaction parameter Mg measures the change in interfacial tension with respect to the local concentration of surface active solutes and is related to the dilatational (Gibbs) elasticity that couples the dynamic boundary conditions on interfacial stress and surfactant flux (Edwards et al., 1991). Typically

Mg	=	$\frac{\tilde{\chi}_2^{(0)}(\tilde{h}) - \tilde{\chi}_1^{(0)}(-\tilde{h})}{\tilde{\gamma}_0}\left(\frac{\partial\tilde{\gamma}}{\partial\chi_j}\right)$	Dilatational elasticity of interface
Cr	=	$\frac{\tilde{\mu}_1\tilde{D}_1}{\tilde{h}\tilde{\gamma}_0}$	Crispation number
Eu	=	$\frac{\tilde{h}^2\tilde{G}_p}{\tilde{\gamma}_0}$	Euler number
Δ_χ	=	$\frac{\tilde{h}\tilde{\gamma}_0}{\tilde{\mu}_1^2}\left(\tilde{\chi}_2(\tilde{h}) - \tilde{\chi}_1(-\tilde{h})\right)$	Overall solute concentration difference
λ	=	$\frac{\tilde{\mu}_2}{\tilde{\mu}_1}$	Dynamic viscosity ratio
Λ	=	$\frac{\tilde{D}_2}{\tilde{D}_1}$	Solute diffusivity ratio
δ	=	$\frac{\tilde{h}-\tilde{\alpha}}{\tilde{h}+\tilde{\alpha}}$	Fluid film thickness ratio

Table 1. The seven dimensionless control parameters that feature in this analysis.

$\mathrm{Mg} > 0$ and the spontaneous physical adsorption of material at the interface will lower the surface free energy relative to the bulk phases. We also interested, however, in the more complex situation where changes of interfacial tension are driven by chemical activity. For example, denaturation, cross-linking or gelation of proteins at the interface may lead to *increases* of tension compared with the bare surface. Within the ansatz (2.2), this behaviour could be modelled by choosing $\mathrm{Mg} < 0$, that is the solutal analogue of the anomalous thermocapillary effect (Braverman et al., 2000).

To accommodate the analysis of a quiescent base state with a vanishing pressure gradient $\tilde{G}_p = 0$, suitable units of mass, length and time are

$$[M] = \frac{(\tilde{h}\tilde{\mu}_1)^2}{\tilde{\gamma}_0} \ , \ [L] = \tilde{h} \ , \ [T] = \frac{\tilde{h}\tilde{\mu}_1}{\tilde{\gamma}_0} \ . \tag{2.3}$$

Accordingly, the dynamics depends on at most seven dimensionless control parameters listed in Table 1. From now on, all dimensionless quantities will be indicated by the absence of tilde decoration.

2.2 *Governing equations*

In the effective two-dimensional geometry, we have the Stokes stream functions $\psi_j = \psi_j(x,\, y,\, t)$ satisfying biharmonic equations

$$\nabla^4\psi_j = \left(\frac{\partial^4}{\partial x^4} + 2\frac{\partial^4}{\partial x^2\partial y^2} + \frac{\partial^4}{\partial y^4}\right)\psi_j = 0 \ , \tag{2.4}$$

that determine the velocity fields $\mathbf{u}_j = u_j\mathbf{i} + v_j\mathbf{j}$ with longitudinal and transverse components

$$u_j = \frac{\partial\psi_j}{\partial y} \ \text{ and } \ v_j = -\frac{\partial\psi_j}{\partial x} \ . \tag{2.5}$$

Incorporating the pressure fields $p_j = p_j(x,\ y,\ t)$, the Newtonian stress tensors are

$$\boldsymbol{\sigma}_j = \boldsymbol{\sigma}_j(x,\ y,\ t) = -p_j\mathbf{I} + \lambda_j\left(\nabla\mathbf{u}_j + \left(\nabla\mathbf{u}_j\right)^T\right)\ , \tag{2.6}$$

where $\lambda_1 = 1$ and $\lambda_2 = \lambda$. The concentration fields are subject to fluid advection and bulk diffusion, described as

$$\left(\frac{\partial}{\partial t} + \mathbf{u}_j\cdot\nabla - \mathrm{Cr}\,\Lambda_j\nabla^2\right)\chi_j = 0\ , \tag{2.7}$$

where $\Lambda_1 = 1$ and $\Lambda_2 = \Lambda$.

With the interface position at $y = \eta(x,\ t)$, the field equations (2.4) and (2.7) are supplemented by no-slip and kinematic boundary conditions:

$$\begin{aligned}
&u_1(x,\ -1,\ t) = 0\ ,\ \ u_2(x,\ 1,\ t) = 0\ , && \left(\text{no slip on walls}\right)\\
&v_1(x,\ -1,\ t) = 0\ ,\ \ v_2(x,\ 1,\ t) = 0\ , && \left(\text{stationary walls}\right)\\
&\left.\begin{aligned}&\left(u_1 - u_2\right)(x,\ \eta,\ t) = 0\\ &\left(v_1 - v_2\right)(x,\ \eta,\ t) = 0\end{aligned}\right\}\ , && \left(\begin{matrix}\text{flow continuity}\\ \text{on interface}\end{matrix}\right)\\
&\frac{\partial\eta}{\partial t} + u_j(x,\ \eta,\ t)\frac{\partial\eta}{\partial x} - v_j(x,\ \eta,\ t) = 0\ . && \left(\begin{matrix}\text{moving material}\\ \text{interface}\end{matrix}\right)
\end{aligned} \tag{2.8}$$

Given local orthogonal unit vectors perpendicular $\hat{\mathbf{n}} = \hat{\mathbf{n}}(x,\ \eta,\ t)$ (directed from fluid 2 into fluid 1) and tangent $\hat{\mathbf{t}} = \hat{\mathbf{t}}(x,\ \eta,\ t)$ to the interface, the corresponding components of the dynamic stress balances become, respectively:

$$\begin{aligned}
&\hat{\mathbf{n}}\cdot\Big(\left(\boldsymbol{\sigma}_1 - \boldsymbol{\sigma}_2\right)(x,\ \eta,\ t)\Big)\cdot\hat{\mathbf{n}} = \left(1 + \left(\frac{\partial\eta}{\partial x}\right)^2\right)^{-3/2}\frac{\partial^2\eta}{\partial x^2}\,\gamma(x,\ \eta,\ t)\ ,\\
&\hat{\mathbf{t}}\cdot\Big(\left(\boldsymbol{\sigma}_1 - \boldsymbol{\sigma}_2\right)(x,\ \eta,\ t)\Big)\cdot\hat{\mathbf{n}} = -\left(1 + \left(\frac{\partial\eta}{\partial x}\right)^2\right)^{-1/2}\left(\frac{\partial\gamma}{\partial x}(x,\ \eta,\ t) + \frac{\partial\eta}{\partial x}\frac{\partial\gamma}{\partial y}(x,\ \eta,\ t)\right)\ .
\end{aligned} \tag{2.9}$$

Finally, concentrations are prescribed on the walls, together with interfacial continuity conditions on the χ_j and the material flux according to:

$$\begin{aligned}
&\left.\begin{aligned}&\chi_1(x,\ -1,\ t) = 1\\ &\chi_2(x,\ 1,\ t) = 1 + \Delta_\chi\end{aligned}\right\}\ , && \left(\begin{matrix}\text{prescribed wall}\\ \text{concentration}\end{matrix}\right)\\
&\left(\chi_1 - \chi_2\right)(x,\ \eta,\ t) = 0\ , && \left(\begin{matrix}\text{concentration continuity}\\ \text{on interface}\end{matrix}\right)\\
&\frac{\partial}{\partial y}\left(\chi_1 - \Lambda\chi_2\right)(x,\ \eta,\ t) = 0\ . && \left(\begin{matrix}\text{concentration flux}\\ \text{continuity on interface}\end{matrix}\right)
\end{aligned} \tag{2.10}$$

3. General analysis of the mathematical model

3.1 *Base (ground) state: unperturbed flow*

For steady plane Poiseuille flow with a flat interface $\eta(x) = \alpha$, we obtain the pressure fields

$$p_j^{(0)} = p_j^{(0)}(x) = p_0 - \mathrm{Eu}\, x \ , \tag{3.1}$$

where p_0 is a constant background pressure and Eu is the Euler number (Table 1). Similarly, the velocity fields are

$$\begin{aligned} u_1^{(0)}(y) &= u_\alpha^{(0)} + \frac{\mathrm{Eu}}{2}(\alpha - y)\left(y - \frac{\delta-\lambda}{\delta+\lambda}\right) = \frac{\partial \psi_1^{(0)}}{\partial y} \ , \quad v_1^{(0)} = 0 \ , \quad (-1 \leqslant y \leqslant \alpha) \ , \\ u_2^{(0)}(y) &= u_\alpha^{(0)} - \frac{\mathrm{Eu}}{2\lambda}(y - \alpha)\left(y - \frac{\delta-\lambda}{\delta+\lambda}\right) = \frac{\partial \psi_2^{(0)}}{\partial y} \ , \quad v_2^{(0)} = 0 \ , \quad (\alpha \leqslant y \leqslant 1) \ , \end{aligned} \tag{3.2}$$

where the horizontal velocity at the interface is

$$u_\alpha^{(0)} = \frac{2\delta\,\mathrm{Eu}}{(1+\delta)(\delta+\lambda)} \ . \tag{3.3}$$

The steady concentration fields are

$$\begin{aligned} \chi_1^{(0)}(y) &= \chi_\alpha^{(0)} - G_{\chi,1}(\alpha - y) \ , \quad (-1 \leqslant y \leqslant \alpha) \ , \\ \chi_2^{(0)}(y) &= \chi_\alpha^{(0)} + G_{\chi,2}(y - \alpha) \ , \quad (\alpha \leqslant y \leqslant 1) \ , \end{aligned} \tag{3.4}$$

where the unperturbed interfacial concentration and corresponding gradients are

$$\chi_\alpha^{(0)} = \frac{\delta + \Lambda\left(1 + \Delta_\chi\right)}{\delta + \Lambda} \ , \qquad G_{\chi,1} = \frac{\Lambda(1+\delta)\Delta_\chi}{2(\delta+\Lambda)} \ , \qquad G_{\chi,2} = \frac{(1+\delta)\Delta_\chi}{2(\delta+\Lambda)} = \frac{G_{\chi,1}}{\Lambda} \ . \tag{3.5}$$

3.2 *Perturbed interface*

We introduce a plane wave perturbation of the interface

$$y = \eta(x,\, t) = \alpha + \varepsilon \Re\big(\mathscr{A} \exp\big(i(kx - \omega t)\big)\big) \ , \tag{3.6}$$

with a prescribed real and positive wavenumber k. Here, $\Re$ denotes the real part. The real order parameter $\varepsilon > 0$ is assumed small so we seek the linear response to the wave disturbance with amplitude $\mathscr{A} = O(1)$. Evolution of the disturbance in time is governed by the imaginary part $\Im(\omega)$ of the generally complex temporal frequency ω. A stable response decays towards zero $\big(\Im(\omega) < 0\big)$ while unbounded growth $\big(\Im(\omega) > 0\big)$ characterises an instability. All other dynamical variables $\Theta \in \big\{\psi_j,\, u_j,\, v_j,\, p_j,\, \chi_j\big\}$ are supposed to develop similar fluctuations directly proportional to E so that

$$\Theta = \Theta(x,\, y,\, t) = \Theta^{(0)}(y) + \varepsilon \Re\big(\Theta^{(1)}(y) \exp\big(i(kx - \omega t)\big)\big) \ . \tag{3.7}$$

To simplify notation, we identify $\mathscr{D} \equiv \mathrm{d}/\mathrm{d}y$ with the differential operator and further adopt the following definitions:

$$k_- \equiv k(1-\alpha) = \frac{2k\delta}{1+\delta} \ , \quad k_+ \equiv k(1+\alpha) = \frac{2k}{1+\delta} \ ,$$

$$c_\xi \equiv \cosh(k\xi)\ \ ,\ \ s_\xi \equiv \sinh(k\xi)\ \ , \tag{3.8}$$

where ξ is a dummy variable.

By virtue of the linear field equations (2.4), the stream function perturbations each satisfy

$$\left(\mathscr{D}^2 - k^2\right)^2 \psi_j^{(1)} = 0\ \ , \tag{3.9}$$

with general solutions of the form

$$\psi_j^{(1)} = \left(\hat{A}_j + \hat{C}_j y\right)c_y + \left(\hat{B}_j + \hat{D}_j y\right)s_y\ \ , \tag{3.10}$$

where $\hat{A}_j$, $\hat{B}_j$, $\hat{C}_j$ and $\hat{D}_j$ are constants to be determined. The linear advection-diffusion law (2.7) yields

$$\left(\mathscr{D}^2 - \left(k^2 + \frac{i}{\mathrm{Cr}\,\Lambda_j}\left(ku_j^{(0)} - \omega\right)\right)\right)\chi_j^{(1)} + \frac{ikG_{\chi,j}}{\mathrm{Cr}\,\Lambda_j}\ \psi_j^{(1)} = 0\ \ . \tag{3.11}$$

With constants $\hat{F}_j$ and $\hat{G}_j$, the general solutions

$$\chi_j^{(1)} = \chi_j^{(1)}(y;\ \omega) = \frac{2\Delta_\chi}{\mathrm{Mg}}\left(\left(\hat{F}_j\Psi_j + \hat{G}_j\Phi_j\right) - ik\,I_j\right)\ \ , \tag{3.12}$$

each comprise a complementary function of the independent homogeneous solutions $\Psi_j = \Psi_j(y)$ and $\Phi_j = \Phi_j(y)$, together with a particular integral $I_j = I_j\left(y;\ \left[\psi_j^{(1)}\right]\right)$. In this general formulation, the Ψ_j and Φ_j are unknown but will be determined explicitly for various cases discussed in Section 4. The I_j are obtained by the variation of parameters method and depend functionally on the flow perturbation:

$$\begin{gathered}
I_j = \hat{A}_j\mathscr{I}_j\left(y;\ \left[c_y\right]\right) + \hat{B}_j\mathscr{I}_j\left(y;\ \left[s_y\right]\right) + \hat{C}_j\mathscr{I}_j\left(y;\ \left[yc_y\right]\right) + \hat{D}_j\mathscr{I}_j\left(y;\ \left[ys_y\right]\right)\ \ , \\
\mathscr{I}_j\left(y;\ \left[\Xi\right]\right) = \frac{\mathrm{Mg}}{\mathrm{Cr}}\left(\frac{G_{\chi,j}}{2\Delta_\chi\Lambda_j}\right)\int^y \Xi(\xi)\left(\frac{\Psi_j(\xi)\Phi_j(y) - \Psi_j(y)\Phi_j(\xi)}{\mathscr{W}\left(\Psi_j(\xi),\ \Phi_j(\xi)\right)}\right)\mathrm{d}\xi\ \ ,
\end{gathered} \tag{3.13}$$

in which

$$\mathscr{W}\left(\Theta_1(\xi_1),\ \Theta_2(\xi_2)\right) = \det\begin{pmatrix}\Theta_1(\xi_1) & \mathscr{D}\Theta_1(\xi_2) \\ \Theta_2(\xi_1) & \mathscr{D}\Theta_2(\xi_2)\end{pmatrix}\ \ , \tag{3.14}$$

becomes the Wronskian of functions Θ_1 and Θ_2 in case $\xi_1 = \xi_2$. In general, the concentration perturbations $\chi_j^{(1)}$ and the associated quantities in (3.12) will all depend parametrically on the unknown temporal frequency ω.

Substitution of (3.7) into the boundary conditions (2.8), (2.9) and (2.10), followed by linearisation to lowest order in ε obtains:

$$\mathscr{D}\psi_1^{(1)}(-1) = 0\ \ ,\ \ \mathscr{D}\psi_2^{(1)}(1) = 0\ \ , \qquad \left(\text{no slip on walls}\right)$$

$$\psi_1^{(1)}(-1) = 0\ \ ,\ \ \psi_2^{(1)}(1) = 0\ \ , \qquad \left(\text{stationary walls}\right)$$

$$\left.\begin{aligned}
&\mathscr{D}\left(\psi_1^{(1)} - \psi_2^{(1)}\right)(\alpha) + J_{\mathbf{u}}\mathscr{A} = 0 \\
&\left(\psi_1^{(1)} - \psi_2^{(1)}\right)(\alpha) = 0
\end{aligned}\right\}\ , \qquad \left(\begin{matrix}\text{flow continuity} \\ \text{on interface}\end{matrix}\right)$$

$$
\begin{aligned}
&k\psi_j^{(1)}(\alpha)+J_\eta\mathscr{A}=0\ , && \left(\begin{array}{c}\text{moving material}\\ \text{interface}\end{array}\right)\\
&\mathscr{D}\left(\mathscr{D}^2-3k^2\right)\left(\psi_1^{(1)}-\lambda\psi_2^{(1)}\right)(\alpha)-2k^2J_{\perp\boldsymbol{\sigma}}\mathscr{A}=0\ , && \left(\begin{array}{c}\text{normal stress}\\ \text{balance on interface}\end{array}\right)\\
&\left(\mathscr{D}^2+k^2\right)\left(\psi_1^{(1)}-\lambda\psi_2^{(1)}\right)(\alpha)+2k\left(i\,\mathrm{Mg}\frac{\chi_2^{(1)}(\alpha)}{2\Delta_\chi}+J_{\|\boldsymbol{\sigma}}\mathscr{A}\right)=0\ , && \left(\begin{array}{c}\text{tangential stress}\\ \text{balance on interface}\end{array}\right)\\
&\chi_1^{(1)}(-1)=0\ ,\ \ \chi_2^{(1)}(1)=0\ , && \left(\begin{array}{c}\text{prescribed wall}\\ \text{concentration}\end{array}\right)\\
&\left(\chi_1^{(1)}-\chi_2^{(1)}\right)(\alpha)+J_\chi\mathscr{A}=0\ , && \left(\begin{array}{c}\text{concentration continuity}\\ \text{on interface}\end{array}\right)\\
&\mathscr{D}\left(\chi_1^{(1)}-\Lambda\chi_2^{(1)}\right)(\alpha)=0\ , && \left(\begin{array}{c}\text{concentration flux}\\ \text{continuity on interface}\end{array}\right)
\end{aligned}
\tag{3.15}
$$

where the “jump” terms proportional to the interfacial disturbance amplitude $\mathscr{A}$ are

$$
\begin{aligned}
J_{\mathbf{u}}&=\mathscr{D}\left(u_1^{(0)}-u_2^{(0)}\right)(\alpha)=\mathrm{Eu}\,\frac{(1-\lambda)(\lambda-\delta^2)}{\lambda(1+\delta)(\lambda+\delta)}\ ,\\
J_\eta&=ku_\alpha^{(0)}-\omega\ ,\\
J_{\perp\boldsymbol{\sigma}}&=\frac{ik}{2}\ ,\\
J_{\|\boldsymbol{\sigma}}&=i\,\mathrm{Mg}\,\frac{G_{\chi,2}}{2\Delta_\chi}=i\,\mathrm{Mg}\,\frac{(1+\delta)}{4(\delta+\Lambda)}\ ,\\
J_\chi&=G_{\chi,1}-G_{\chi,2}=\frac{(1+\delta)(\Lambda-1)\Delta_\chi}{2(\delta+\Lambda)}\ .
\end{aligned}
\tag{3.16}
$$

The homogeneous linear system (3.15) demands a singular coefficient matrix to deliver non-trivial solutions. Lengthy but straightforward calculation of the determinant leads to the dispersion relation

$$
\mathscr{L}_{k,\alpha}(\Lambda)\left(\kappa_{\mathbf{u}}J_{\mathbf{u}}+\kappa_\eta J_\eta+\kappa_{\perp\boldsymbol{\sigma}}J_{\perp\boldsymbol{\sigma}}\right)+\Lambda\mathscr{L}_{k,\alpha}(1)\kappa_{\|\boldsymbol{\sigma}}J_{\|\boldsymbol{\sigma}}=0\ ,
\tag{3.17}
$$

where the function $\mathscr{L}_{k,\alpha}$ and the coefficients $\kappa_{\mathbf{u}}$, κ_η and $\kappa_{\perp\boldsymbol{\sigma}}$ all depend parametrically on ω as detailed in Section 9.1. The relatively simple coefficient $\kappa_{\|\boldsymbol{\sigma}}$ depends only on the wavenumber k and the geometric parameter δ. Further analysis requires solutions of the advection-diffusion equation (2.7) to evaluate the integrals I_j and to determine the functional form of $\mathscr{L}_{k,\alpha}$. As well as the most general case, notable limiting situations are discussed in the following sections.

4. Special cases from the general analysis

4.1 *Case I:* Cr $\to \infty$ *with* $0 < \Lambda < \infty$

For large crispation number and $0 < \Lambda < \infty$, solute diffusion in both films is effectively instantaneous on the time scale of interfacial fluctuations. In this circumstance, the solute transport equation (2.7) then reduces to Laplace's equation and the perturbed concentration fields now satisfy a simple diffusion equation (cf. (3.11))

$$\left(\mathscr{D}^2 - k^2\right)\chi_j^{(1)} = 0 \quad , \tag{4.1}$$

regardless of any base state flow. Solutions of these homogeneous ODEs take the form (3.12) with

$$\Psi_j = c_y \ \text{ and } \ \Phi_j = s_y \quad , \tag{4.2}$$

independent of ω, and the particular integrals vanish $\left(I_j = 0\right)$. As a consequence, the concentration fields are decoupled from the fluid flows and can be solved independently to yield:

$$\chi_1^{(1)} = -J_\chi \mathscr{A}\, \frac{k\Lambda c_{1-\alpha} s_{1+y}}{\mathscr{L}_{k,\alpha}^{(0)}(\Lambda)} \quad , \qquad \chi_2^{(1)} = J_\chi \mathscr{A}\, \frac{k c_{1+\alpha} s_{1-y}}{\mathscr{L}_{k,\alpha}^{(0)}(\Lambda)} \quad , \tag{4.3}$$

where

$$\mathscr{L}_{k,\alpha}^{(0)}(\Lambda) = k\left(\Lambda c_{1-\alpha} s_{1+\alpha} + c_{1+\alpha} s_{1-\alpha}\right) > 0 \quad , \tag{4.4}$$

and the frequency parameter ω does not enter (see Section 9.1). In the case of identical mass diffusivities for both films, then $J_\chi = 0$ so that $\chi_1^{(1)} = \chi_2^{(1)} = 0$ and the base state concentration fields $\chi_j^{(0)}$ are maintained everywhere for all time regardless of perturbations to the fluid flows.

A dispersion relation of the form (3.17) is obtained:

$$\kappa_{\mathbf{u}}^{(0)} J_{\mathbf{u}} + \kappa_\eta^{(0)} J_\eta + \kappa_{\perp\boldsymbol{\sigma}}^{(0)} J_{\perp\boldsymbol{\sigma}} + \left(\frac{\Lambda \mathscr{L}_{k,\alpha}^{(0)}(1)}{\mathscr{L}_{k,\alpha}^{(0)}(\Lambda)}\right) \kappa_{\parallel\boldsymbol{\sigma}} J_{\parallel\boldsymbol{\sigma}} = 0 \quad , \tag{4.5}$$

but where the $\kappa^{(0)}$-coefficients are independent of the frequency parameter ω (see Section 9.1) that now appears only in J_η (see (3.16)). Define the functions

$$g_\xi \equiv \sinh^2(k\xi) - (k\xi)^2 \quad , \qquad \mathscr{D}g_\xi \equiv \sinh(2k\xi) - 2k\xi \quad , \qquad h_\xi \equiv \frac{g_\xi}{\mathscr{D}g_\xi} \quad , \tag{4.6}$$

with a natural extension of our earlier subscript notation (3.8). From (4.5) the disturbance growth rate is

$$\begin{aligned}
\Im(\omega) &= \frac{\mathscr{L}_{k,\alpha}^{(0)}(\Lambda)\kappa_{\perp\boldsymbol{\sigma}}^{(0)} \Im\left(J_{\perp\boldsymbol{\sigma}}\right) + \Lambda \mathscr{L}_{k,\alpha}^{(0)}(1)\kappa_{\parallel\boldsymbol{\sigma}} \Im\left(J_{\parallel\boldsymbol{\sigma}}\right)}{\mathscr{L}_{k,\alpha}^{(0)}(\Lambda)\kappa_\eta^{(0)}} \\
&= \frac{k g_{1+\alpha}}{4\kappa_\eta^{(0)}} \left(\text{Mg}\, \mathscr{M}_{k,\alpha}(\Lambda)\left(\lambda\delta^2 - \frac{g_{1-\alpha}}{g_{1+\alpha}}\right) - \mathscr{D}g_{1-\alpha}\left(\lambda + \frac{h_{1-\alpha}}{h_{1+\alpha}}\right)\right) \qquad (4.7) \\
&= \frac{k g_{1-\alpha}}{4\kappa_\eta^{(0)}}\, \lambda \left(\text{Mg}\, \mathscr{M}_{k,\alpha}(\Lambda)\delta^2 \left(\frac{g_{1+\alpha}}{g_{1-\alpha}} - \frac{1}{\lambda\delta^2}\right) - \mathscr{D}g_{1+\alpha}\left(\frac{1}{\lambda} + \frac{h_{1+\alpha}}{h_{1-\alpha}}\right)\right) \quad ,
\end{aligned}$$

where

$$\mathscr{M}_{k,\alpha}(\Lambda) = \frac{4k\Lambda\mathscr{L}^{(0)}_{k,\alpha}(1)}{(1+\delta)(\delta+\Lambda)\mathscr{L}^{(0)}_{k,\alpha}(\Lambda)} = \frac{2k_+^2\Lambda s_2}{\left(k_+\Lambda+k_-\right)\left(c_{1-\alpha}s_{1+\alpha}\Lambda+c_{1+\alpha}s_{1-\alpha}\right)} > 0 \ , \tag{4.8}$$

depends on the excitation wavenumber, the flow composition and the solute diffusivities, but is a manifestly positive quantity. Similarly, from (4.5) the real part of the temporal frequency is

$$\begin{aligned}\Re(\omega) &= ku^{(0)}_\alpha + \frac{\kappa^{(0)}_{\mathbf{u}}J_{\mathbf{u}}}{\kappa^{(0)}_\eta} \\ &= \frac{\mathrm{Eu}}{\kappa^{(0)}_\eta(1+\delta)(\delta+\lambda)}\left(\tfrac{1}{2}\left(k_+^2\mathscr{D}g_{1-\alpha}+k_-^2\mathscr{D}g_{1+\alpha}\right)\left(\lambda-\delta^2\right)(\lambda-1)+2k\kappa^{(0)}_\eta\delta\right) \ .\end{aligned} \tag{4.9}$$

Consequences of these results are discussed in Section 6.1.

4.2 *Case II:* $0<\mathrm{Cr}<\infty$ *and* $\mathrm{Eu}=0$

In the absence of a driving pressure gradient, the base state is quiescent (note especially that $J_{\mathbf{u}}=0$, while $J_\eta=-\omega$) and the governing equations for the concentration perturbations become

$$\begin{aligned}&\left(\mathscr{D}^2-K_j^2(\omega)\right)\chi^{(1)}_j+\frac{ikG_{\chi,j}}{\mathrm{Cr}\,\Lambda_j}\,\psi^{(1)}_j=0 \ , \\ &\text{where} \qquad K_j^2(\omega)=k^2+K_{0j}^2(\omega) \qquad \text{with} \qquad K_{0j}^2(\omega)=-\frac{i\omega}{\mathrm{Cr}\,\Lambda_j} \ .\end{aligned} \tag{4.10}$$

Following our earlier style, the notation is simplified by adopting the definitions:

$$C_{j,\xi}\equiv\cosh\left(K_j\xi\right) \ , \ S_{j,\xi}\equiv\sinh\left(K_j\xi\right) \ . \tag{4.11}$$

Although the ODEs (4.10) are inhomogeneous, the coefficients K_j^2 are constant in space, so explicit solutions are readily obtained. The complementary functions comprise

$$\Psi_j(y)=C_{j,y} \ \text{ and } \ \Phi_j(y)=S_{j,y} \ , \tag{4.12}$$

with the simple spatially uniform Wronskian $\mathscr{W}\left(\Psi_j(\xi),\,\Phi_j(\xi)\right)=K_j(\omega)$. A lengthy but straightforward calculation of the particular integrals leads to the dispersion relation (see Section 9.2)

$$\mathscr{L}^{(1)}_{k,\alpha}(\Lambda)\left(-\kappa^{(1)}_\eta\omega+\kappa^{(1)}_{\perp\boldsymbol{\sigma}}J_{\perp\boldsymbol{\sigma}}\right)+\Lambda\mathscr{L}^{(1)}_{k,\alpha}(1)\kappa_{\parallel\boldsymbol{\sigma}}J_{\parallel\boldsymbol{\sigma}}=0 \ , \tag{4.13}$$

where (cf. (4.4))

$$\mathscr{L}^{(1)}_{k,\alpha}(\Lambda)=K_2\Lambda C_{2,1-\alpha}S_{1,1+\alpha}+K_1C_{1,1+\alpha}S_{2,1-\alpha} \ . \tag{4.14}$$

The result (4.13) follows the general form (3.17) but with the Poiseuille flow term absent. As the frequency ω is now intimately incorporated into the arguments of transcendental functions, it is not expedient to explicitly extract the growth rate $\Im(\omega)$ or oscillation rate $\Re(\omega)$ despite the ready availability of (4.13). Nevertheless, implementation of (4.13) (MATLAB, 2013) provides a useful verification tool for other numerical solution schemes (see Section 5.2).

5. General solution

5.1 *Case III:* $0 < \mathrm{Cr} < \infty$ *and* $\mathrm{Eu} \neq 0$

The governing equations for the concentration perturbations become

$$\left(\mathscr{D}^2 - \left(K_j^2(\omega) + \frac{iku_j^{(0)}}{\mathrm{Cr}\,\Lambda_j}\right)\right)\chi_j^{(1)} + \frac{ikG_{\chi,j}}{\mathrm{Cr}\,\Lambda_j}\,\psi_j^{(1)} = 0 \ , \tag{5.1}$$

where $u_j^{(0)}$ is quadratic in y as given by (3.2). In the base state, the parabolic velocity profiles of (3.2) share a common symmetry axis located at

$$y = \bar{y} = \frac{\delta(1-\lambda)}{(1+\delta)(\delta+\lambda)} \ . \tag{5.2}$$

On applying the transformation

$$Y(y) = \left(\frac{2ik\,\mathrm{Eu}}{\mathrm{Cr}\,\Lambda_j}\right)^{1/4}\left(y-\bar{y}\right) \ , \tag{5.3}$$

the homogeneous equation corresponding to (5.1) is brought into the standard form

$$\left(\frac{\mathrm{d}^2}{\mathrm{d}Y^2} + \left(\tfrac{1}{4}Y^2 - \Upsilon_j(\omega)\right)\right)\chi_j^{(1)} = 0 \ , \tag{5.4}$$

where

$$\Upsilon_j(\omega) = \left(K_j^2(\omega) + \frac{ik\bar{u}_j^{(0)}}{\mathrm{Cr}\,\Lambda_j}\right)\left(\frac{2ik\,\mathrm{Eu}}{\mathrm{Cr}\,\Lambda_j}\right)^{-1/2} \ , \tag{5.5}$$

and we have the complementary solution in terms of a single parabolic cylinder (Weber) function (Abramowitz & Stegun, 1965)

$$\Psi_j(y) = W\left(\Upsilon_j,\, y\right) \ \text{ and } \ \Phi_j(y) = W\left(\Upsilon_j,\, -y\right) \ , \tag{5.6}$$

with the constant Wronskian $\mathscr{W} = 1$. These analytic solutions of the transport equations (5.1) lead to a very complicated implicit dispersion relation involving transcendental functions. It appears very difficult (if not impossible) to exactly solve this eigenvalue problem, or merely to establish precisely how many response modes exist. Here we shall consider a numerical scheme instead, that will resolve these issues.

5.2 *A numerical scheme: Chebyshev collocation method*

Recall the stream function perturbations $\psi_j^{(1)}$ satisfy a biharmonic field equation (3.9), that is equivalent to the Orr-Sommerfeld equation at vanishing Reynolds number, and explicit solutions are obtained in the form (3.10). Following Gottleib & Orszag (1977), the set of orthogonal Chebyshev polynomials $T_n : [-1,1] \to [-1,1]$ provides an appropriate basis for the approximation space of $\chi_j^{(1)}$ and we write the truncated expansions

$$\chi_j^{(1)}(y) = \sum_{n=0}^{N_j} a_{jn} T_n\left(y_j(y)\right) \ , \tag{5.7}$$

where the spanwise coordinate is linearly mapped onto the canonical domain:

$$\begin{aligned} y_1(y) &= (1+\delta)y+\delta \ , \ (-1 \leqslant y \leqslant \alpha) \ , \\ y_2(y) &= \frac{1}{\delta}\Big((1+\delta)y-1\Big) \ , \ (\alpha \leqslant y \leqslant 1) \ , \end{aligned} \tag{5.8}$$

with the differential transformations,

$$\mathscr{D}y_1 = 1+\delta \qquad \text{and} \qquad \mathscr{D}y_2 = 1+\frac{1}{\delta} \ . \tag{5.9}$$

The Gauss-Lobatto points,

$$y_{jn} = \cos\left(\frac{n\pi}{N_j}\right) \ , \ \big(n = 0,\ 1,\ 2,\ \dots,\ N_j\big) \ . \tag{5.10}$$

corresponding to the extrema of the highest order polynomial, are optimal for collocation (Schmid & Henningson, 2001). Altogether with the linearised boundary conditions (3.15), this set of governing equations is assembled into the system

$$\mathbf{Aw} = \omega \mathbf{Bw} \ , \tag{5.11}$$

which we recognise as a generalised eigenvalue problem for the eigenvalue ω and the associated eigenvector

$$\mathbf{w} = \big(a_{10} \quad \dots \quad a_{1N_1} \quad a_{20} \quad \dots \quad a_{2N_2} \quad \hat{A}_1 \quad \hat{B}_1 \quad \hat{C}_1 \quad \hat{D}_1 \quad \hat{A}_2 \quad \hat{B}_2 \quad \hat{C}_2 \quad \hat{D}_2 \quad \mathscr{A}\big)^T \ . \tag{5.12}$$

These N_1+N_2+11 unknowns are determined by the 13 boundary conditions along with the field evaluations at the $\big(N_1-1\big)+\big(N_2-1\big)$ "interior" collocation points corresponding to the turning points of T_{N_1} and T_{N_2}. A Matlab code (MATLAB, 2013) has been implemented using the built-in routine `eig` to solve the generalised eigenvalue problem. To consistently compare results across the wavenumber spectrum, the eigenvectors are uniformly scaled so that the disturbance amplitude of the interface becomes $\mathscr{A} = 1 \in \mathbb{R}$.

5.3 *The situation $k = 0$ and* Eu $\geqslant 0$

At zero wavenumber, it turns out that a base state flow plays no role in the eigenvalue spectrum. The governing equations (3.9) for the stream function perturbations reduce to

$$\mathscr{D}^4 \psi_j^{(1)} = 0 \ , \tag{5.13}$$

with general solutions in the form of a cubic polynomial

$$\psi_j^{(1)} = \hat{A}_j y^3 + \hat{B}_j y^2 + \hat{C}_j y + \hat{D}_j \ . \tag{5.14}$$

The concentration field perturbations are also determined by homogeneous ODEs

$$\big(\mathscr{D}^2 - K_{0j}^2(\omega)\big)\, \chi_j^{(1)} = 0 \ , \tag{5.15}$$

with general solutions (cf. (3.12))

$$\chi_j^{(1)} = \frac{2\Delta_\chi}{\mathrm{Mg}} \big(\hat{F}_j\, C_{j,y} + \hat{G}_j\, S_{j,y}\big) \ . \tag{5.16}$$

Furthermore, the interfacial stress boundary conditions are simplified considerably: in particular the tangential coupling between $\psi_j^{(1)}$ and $\chi_j^{(1)}$ is broken so that the dispersion relation is easily recovered

$$\omega\,\mathscr{L}_{0,\alpha}^{(1)}(\Lambda)\left(\frac{\lambda^2+2\delta\big(2\delta^2+3\delta+2\big)\lambda+\delta^4}{(1+\delta)^4}\right)=0\ , \tag{5.17}$$

and the non-trivial modes are determined by (cf. (4.14))

$$\mathscr{L}_{0,\alpha}^{(1)}(\Lambda)=K_0\Big(\sqrt{\Lambda}\cosh\big(K_0h_-\big)\sinh\big(K_0h_+\big)+\cosh\big(K_0h_+\big)\sinh\big(K_0h_-\big)\Big)=0\ , \tag{5.18}$$

where

$$h_-=\frac{2\delta}{(1+\delta)\sqrt{\Lambda}}=\frac{1-\alpha}{\sqrt{\Lambda}}\ ,\qquad h_+=\frac{2}{1+\delta}=1+\alpha\qquad\text{and}\qquad K_0=\sqrt{-\frac{i\omega}{\mathrm{Cr}}}\ . \tag{5.19}$$

6. Results and discussion

6.1 *Instantaneous solute diffusion* $\mathrm{Cr}\to\infty$, $0<\Lambda<\infty$ *(Case I)*

Explicit expressions for the temporal frequency in Case I (4.7 and 4.9) permit detailed analysis of the linear response. For all physical parameter values, the quantity $\kappa_\eta^{(0)}$ is strictly positive (see Section 9.3). It follows from (4.7) that the interface is generally stable ($\Im(\omega)<0$) against large wavenumber perturbations ($k\to\infty$). By considering the k-expansion

$$\Im(\omega)=\frac{\mathrm{Mg}\big(\lambda-\delta^2\big)\Lambda\delta^2}{\Big(\lambda^2+2\delta\big(2+3\delta+2\delta^2\big)\lambda+\delta^4\Big)(\Lambda+\delta)^2}\,k^2+O\big(k^4\big)\ , \tag{6.1}$$

a region of instability exists for $\mathrm{Mg}>0$ provided $\lambda>\delta^2$. Conversely, $\mathrm{Mg}<0$ requires $\lambda<\delta^2$ for this instability to appear. Hence, it is natural to define a *pseudo*-critical viscosity ratio $\lambda_c=\delta^2$. It should be emphasised here that this is a small wavenumber analysis that does not exclude the possibility of instabilities where $\Im(\omega)$ first becomes positive for some wavenumber $k_c>0$.

These response characteristics are confirmed by the family of dispersion curves plotted in Figure 1 where, given $\mathrm{Mg}=100$, panels a), b) and c) consistently exhibit a stable response for $\lambda>\delta^2$, a marginal state at $\lambda=\delta^2$ and instability for $\lambda<\delta^2$. Within the systematic classification scheme of Cross and coworkers (Cross & Hohenberg, 1993; Cross & Greenside, 2009), this is a stationary instability of Type-II universally characterised by a zero growth rate at $k=0$ and maximum amplification rate at intermediate wavenumber $0<k<\infty$. Figure 1 also demonstrates the stability criterion is independent of the mass diffusivity ratio Λ. This is unsurprising in the limit ($\mathrm{Cr}\to\infty$), since equilibration of the concentration profile is fast compared with the flow dynamics: the interface moves in a concentration field that is oblivious to the fluid flows. Despite this decoupling, the concentration field is perturbed nevertheless (see (4.3)) by a stratification of the bulk mass diffusivity (Figure 1d). Throughout Figure 1 the analytic results (Section 4.1) show excellent agreement with the approximate results using the collocation computations (Section 5.2).

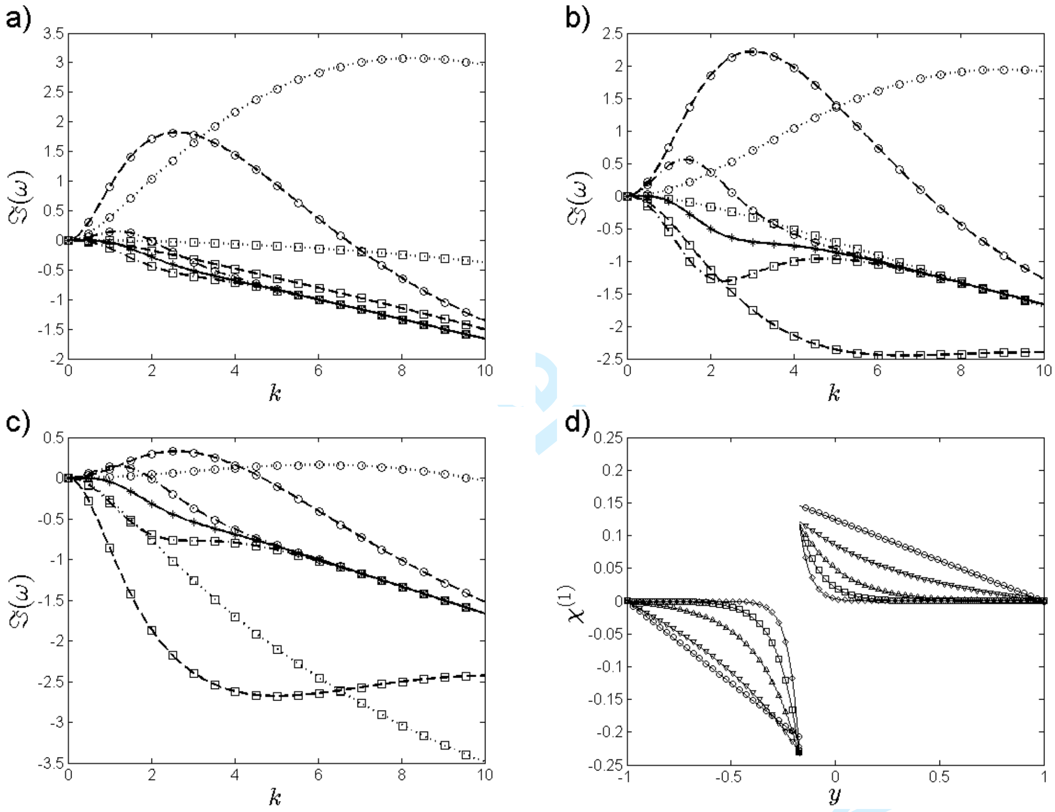

FIG. 1. Growth rate dispersion curves for Case I ($\mathrm{Cr} \to \infty$) are displayed for parameter values $\mathrm{Mg} = 100$, $\lambda = 2$ and $\Delta_\chi = 1$ with a) $\Lambda = 0.1$; b) $\Lambda = 1$ and c) $\Lambda = 10$. Results from the analytic expression (4.7), shown as lines, are compared with isolated point calculations using the numerical collocation method (denoted by symbols) described in Section 5.2 with $N_1 = N_2 = 32$. Entirely stable response is indicated by squares with the flow composition parameter δ set to $40(\cdots)$, $10(--)$ and $2(\cdot - \cdot)$. Circles identify response curves with small wavenumber instability with δ set to $1(\cdot - \cdot)$, $0.2(--)$ and $0.05(\cdots)$. The marginally stable response is plotted with asterisk symbols and a full line (——) where $\delta_c = \sqrt{\lambda} = \sqrt{2}$.

At the stability margin ($\lambda = 2$ and $\delta = \sqrt{2}$ with $\mathrm{Mg} = 100$, $\Delta_\chi = 1$ and $\Lambda = 2$), panel d) shows a corresponding comparison of concentration perturbation profiles across the slab where results from (4.3) are plotted as lines and collocation calculations are denoted by symbols with wavenumbers k set to $0.1(\bigcirc)$, $2(\bigtriangledown)$, $5(\bigtriangleup)$, $10(\square)$ and $20(\diamond)$.

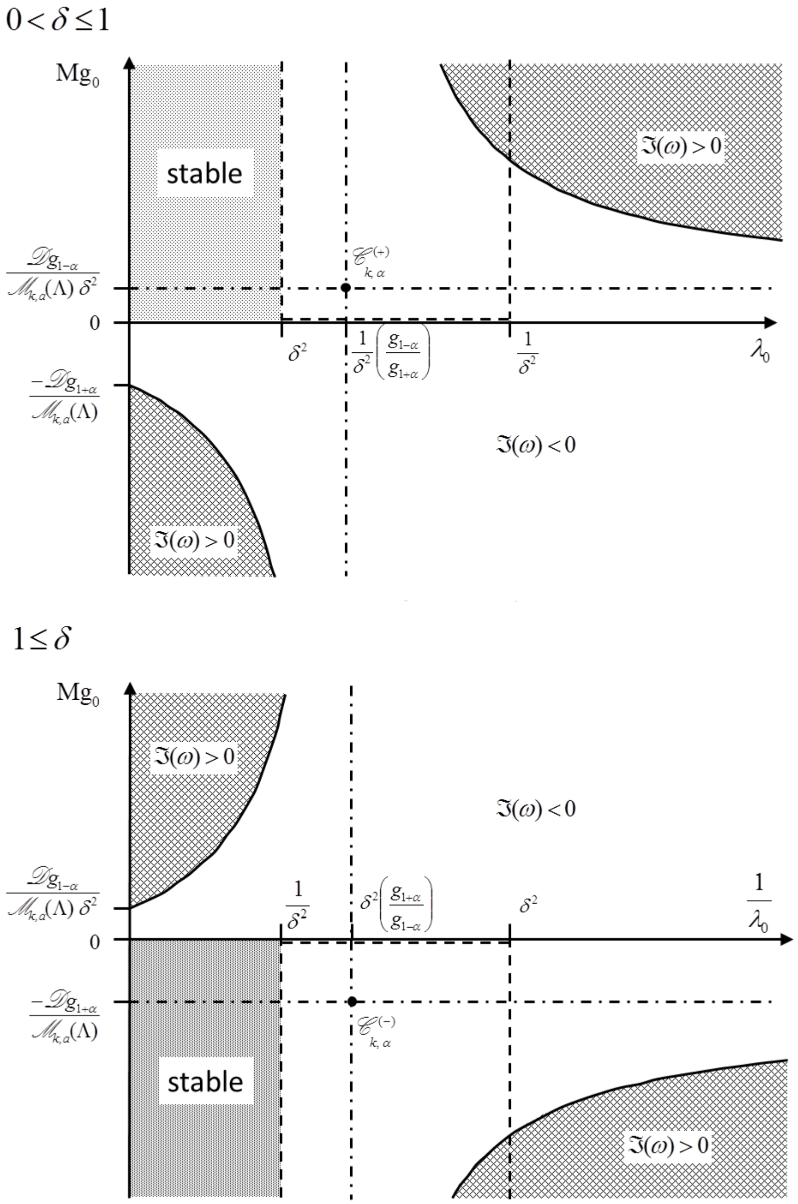

FIG. 2. Stability diagram for Case I $\left(\mathrm{Cr}\to\infty \text{ and } 0<\Lambda<\infty\right)$. Typical marginal stability boundaries $\left(\Im(\omega)=0\right)$ projected into the plane of viscosity ratio λ_0 and Gibbs elasticity Mg_0 appear as a rectangular hyperbola (——). With varying excitation wavenumber k, the asymptotes $(\cdot-\cdot)$ move about the plane but the centre $\mathscr{C}^{(\pm)}_{k,\alpha}$ is confined to the unbounded rectangular region indicated $(--)$. Provided $\lambda_0<\lambda_c=\delta^2$, a domain of stability (shaded area) can be identified where all linear perturbations decay in time.

For arbitrary wavenumber, marginal stability relations $\big(\Im(\omega)=0\big)$ are obtained directly from (4.7), and solving for the interfacial elasticity parameter yields

$$\mathrm{Mg}_0 = \frac{g_{1+\alpha}\mathscr{D}g_{1-\alpha}\,\lambda_0 + g_{1-\alpha}\mathscr{D}g_{1+\alpha}}{\mathscr{M}_{k,\alpha}(\Lambda)\big(g_{1+\alpha}\delta^2\,\lambda_0 - g_{1-\alpha}\big)} = \frac{g_{1+\alpha}\mathscr{D}g_{1-\alpha} + g_{1-\alpha}\mathscr{D}g_{1+\alpha}\,\lambda_0^{-1}}{\mathscr{M}_{k,\alpha}(\Lambda)\big(g_{1+\alpha}\delta^2 - g_{1-\alpha}\,\lambda_0^{-1}\big)} \;, \tag{6.2}$$

where Mg_0 and λ_0 are marginal values of the corresponding control parameters. Equations (6.2) describe rectangular hyperbolae, centred on a point denoted $\mathscr{C}^{(+)}_{k,\alpha}$ in the $\big(\lambda_0,\ \mathrm{Mg}_0\big)$ plane, or centred on $\mathscr{C}^{(-)}_{k,\alpha}$ in the $\big(\lambda_0^{-1},\ \mathrm{Mg}_0\big)$ plane with coordinates

$$\mathscr{C}^{(+)}_{k,\alpha} = \left(\frac{1}{\delta^2}\left(\frac{g_{1-\alpha}}{g_{1+\alpha}}\right),\ \frac{\mathscr{D}g_{1-\alpha}}{\delta^2\mathscr{M}_{k,\alpha}(\Lambda)}\right) \qquad \text{and} \qquad \mathscr{C}^{(-)}_{k,\alpha} = \left(\delta^2\left(\frac{g_{1+\alpha}}{g_{1-\alpha}}\right),\ -\frac{\mathscr{D}g_{1+\alpha}}{\mathscr{M}_{k,\alpha}(\Lambda)}\right) \;. \tag{6.3}$$

Since g is both positive and strictly increasing (see definitions (4.6)), it is easy to verify

$$\begin{gathered} 0<\delta<1 \;\Rightarrow\; 0<\alpha<1 \;\Rightarrow\; \delta^4 < \frac{g_{1-\alpha}}{g_{1+\alpha}} < 1 \;, \\ 1<\delta<\infty \;\Rightarrow\; -1<\alpha<0 \;\Rightarrow\; \frac{1}{\delta^4} < \frac{g_{1+\alpha}}{g_{1-\alpha}} < 1 \\ \text{and} \qquad \lim_{k\to\infty}\frac{\mathscr{D}g_{1\pm\alpha}}{\mathscr{M}_{k,\alpha}(\Lambda)}\,\exp\big(-2k_{\pm}\big) = 0 \;, \end{gathered} \tag{6.4}$$

so that the positions $\mathscr{C}^{(\pm)}_{k,\alpha}$ are restricted as shown in Figure 2. It follows that global temporal stability is confined to the λ_0 axis (where $\mathrm{Mg}_0=0$) and either the region $\big(\lambda_0,\ \mathrm{Mg}_0\big)\in\big(0,\ \delta^2\big)\times(0,\ \infty)$ for $0<\delta\leqslant 1$, or the region $\big(\lambda_0^{-1},\ \mathrm{Mg}_0\big)\in\big(0,\ \delta^2\big)\times(-\infty,\ 0)$ for $1\leqslant\delta$. This is consistent with the small wavenumber analysis and confirms the critical viscosity ratio $\lambda_c=\delta^2$. With a more conventional insoluble surfactant ansatz, the same result has been established in the small-k analysis of Frenkel & Halpern (2002) and the lubrication-flow model of Blyth & Pozrikidis (2004a).

A mechanical interpretation of this small wavenumber instability is illustrated in Figure 3. Large scale disturbances are suppressed by a destructive normal fluid velocity component with a π phase shift (Figure 3a and 3b), while changes in γ remain in-phase with the interface profile. At the margin of stability (Figure 3c and 3d) $v^{(1)}(y)$ swaps, on passing through the interface, from constructive in-phase to destructive out-of-phase interference with the disturbance wave. An unstable response is characterised by an in-phase normal velocity component that amplifies the interfacial disturbance (Figure 3e and 3f). In steady Stokes flow, the vorticity

$$\boldsymbol{\varpi}_j = \nabla\times\mathbf{u}_j = \left(\frac{\partial v_j}{\partial x} - \frac{\partial u_j}{\partial y}\right)\mathbf{k} = -\nabla^2\psi_j\,\mathbf{k} \;, \tag{6.5}$$

is harmonic $\nabla^2\boldsymbol{\varpi}_j=\mathbf{0}$ (cf. (2.4)) and closely related to the pressure so that $\lambda_j\big(\partial\boldsymbol{\varpi}_j/\partial x\big)=\big(\partial p_j/\partial y\big)\mathbf{k}$ and $\lambda_j\big(\partial\boldsymbol{\varpi}_j/\partial y\big)=\big(\partial p_j/\partial x\big)\mathbf{k}$. Consequently, the vorticity is discontinuous at the interface and the phase of the perturbation $\mathrm{Arg}\big(\varpi^{(1)}\big)$ changes abruptly at $y=\alpha$ from a $\pi/2$ lag in the more viscous film to a $\pi/2$ lead in the less viscous layer (Figure 3b, d and f). It appears the pressure is always destructively out of phase with the interface deformation over the whole fluid slab (data not shown). Although four convection cells are evident in the marginal state (Figure 3c and 3d), only two cells

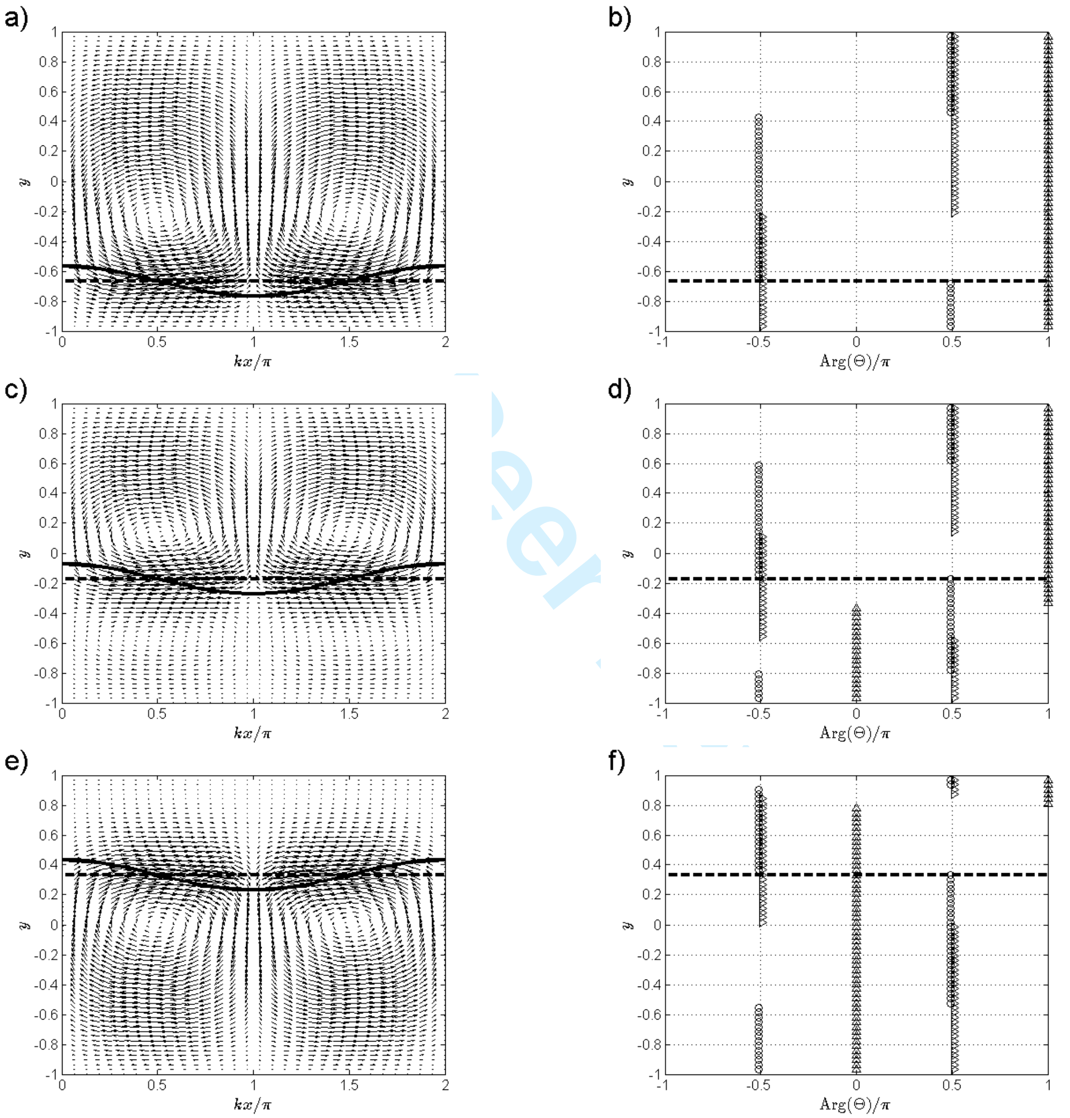

FIG. 3. Flow fields calculated by the collocation method $\left(N_1 = N_2 = 32\right)$ are shown for Case I with $\mathrm{Cr} \to \infty$. Throughout, the control parameter values $\mathrm{Mg} = 5$, $\mathrm{Eu} = 0$, $\lambda = 2$, $\Lambda = 1$, $\Delta_\chi = 1$ are set.
Panels (a), (c) and (e): direction fields associated with the fluid velocity $\mathbf{u}(x,\ y) = u(x,\ y)\mathbf{i} + v(x,\ y)\mathbf{j}$ are plotted. The superimposed lines indicate the quiescent interface position $(--)$ and a harmonic disturbance (——) of arbitrary amplitude $(\varepsilon = 0.1)$.
Panels (b), (d) and (f): show the corresponding principal arguments of the perturbed velocities and vorticity field $\Theta \in \left\{u^{(1)}(y),\ v^{(1)}(y),\ \varpi^{(1)}(y)\right\}$. The tangential $u^{(1)}$ and normal $v^{(1)}$ velocity components are denoted by $(\triangleright)$ and $(\triangle)$, respectively, and the phase of the vorticity $\varpi^{(1)}$ is indicated by ○. Again, the quiescent interface position is shown by $(--)$.
Each pair of panels indicates a stable situation ($\delta = 5$, a and b); a marginal situation ($\delta = \sqrt{2}$, c and d) and an unstable situation ($\delta = 0.5$, e and f).

develop for states lying deep in either the stable (e.g., Figure 3a and 3b) or unstable (data not shown) regimes. This contrasts with several studies of the analogous thermocapillary problem (Andereck et al., 1998) that focussed on different flow patterns, but where four cells are always generated by imposing a rigid undeformable interface.

In this special Case I, only a single response mode is excited that always remains completely decoupled from the base state flow: the growth rate $\Im(\omega)$ given by (4.7) is independent of Eu. For a quiescent base state flow the disturbance is, of course, stationary in space $\big(\Re(\omega)=0\big)$, but if a pressure gradient exists $(\mathrm{Eu}>0)$ it can be deduced from (4.9) that $\Re(\omega)>0$ (see Section 9.4) and a propagating wave develops on the interface that travels downstream with the speed

$$\begin{aligned}\frac{\Re(\omega)}{k} &= u_\alpha^{(0)} + \frac{\kappa_{\mathbf{u}}^{(0)} J_{\mathbf{u}}}{k\kappa_\eta^{(0)}} \\ &= \frac{\mathrm{Eu}}{\kappa_\eta^{(0)}(1+\delta)(\delta+\lambda)}\left(\left(\frac{k_+^2\mathscr{D}g_{1-\alpha}+k_-^2\mathscr{D}g_{1+\alpha}}{k_++k_-}\right)(\lambda-\delta^2)(\lambda-1)+2\kappa_\eta^{(0)}\delta\right) \ .\end{aligned} \tag{6.6}$$

Further, by setting $\mathrm{Eu}=\frac{1}{2}(1+\delta)(\delta+\lambda)/\delta$, or equivalently demanding the horizontal fluid velocity component satisfy $u_\alpha^{(0)}=1$, and also choosing $\delta=1$ before finally considering the limit $k\to\infty$, we recover the dispersionless result

$$\frac{\Re(\omega)}{k} = 1+\frac{2(1-\lambda)^2}{\lambda^2+14\lambda+1} \ , \tag{6.7}$$

obtained by Yih (1967) for the plane Poiseuille flow in a finite channel of two superposed fluids with equal depth and density, but different viscosities.

6.2 *Comparable diffusion rates of matter and momentum* $0<\mathrm{Cr}<\infty$ *(Case II)*

At finite crispation numbers (Case II and III), the response behaviour is qualitatively very different (see Figure 4 for example) from Case I (Section 6.1). Analysis of the $k=0$ situation (see Section 9.5) shows that the temporal frequency has zero real part $\big(\Re(\omega)=0\big)$ and non-positive imaginary part $\big(\Im(\omega)\leqslant 0\big)$. Indeed, the dispersion relation (5.18) reduces to

$$\sqrt{\Lambda}\sin\left(h_+\sqrt{-\frac{\Im(\omega)}{\mathrm{Cr}}}\right)\cos\left(h_-\sqrt{-\frac{\Im(\omega)}{\mathrm{Cr}}}\right)+\cos\left(h_+\sqrt{-\frac{\Im(\omega)}{\mathrm{Cr}}}\right)\sin\left(h_-\sqrt{-\frac{\Im(\omega)}{\mathrm{Cr}}}\right)=0 \ . \tag{6.8}$$

Formally, this defines the nodes of a wave with two harmonic components differing in both frequency and amplitude described by

$$\big(\sqrt{\Lambda}+1\big)\sin\left(\frac{2}{1+\delta}\left(1+\frac{\delta}{\sqrt{\Lambda}}\right)\sqrt{-\frac{\Im(\omega)}{\mathrm{Cr}}}\right)+\big(\sqrt{\Lambda}-1\big)\sin\left(\frac{2}{1+\delta}\left(1-\frac{\delta}{\sqrt{\Lambda}}\right)\sqrt{-\frac{\Im(\omega)}{\mathrm{Cr}}}\right)=0 \ . \tag{6.9}$$

A general closed form solution of (6.9) is intractable. If $\Lambda=1$, however, the second term vanishes in (6.9) and a simple expression, independent of δ, is obtained for the growth rate spectrum

$$\sqrt{-\frac{\Im(\omega)}{\mathrm{Cr}}}=m\,\frac{\pi}{2} \ , \qquad (m=0,\ 1,\ 2,\ldots) \ . \tag{6.10}$$

Similarly, if $\Lambda = \delta^2$, then

$$\frac{1}{1+\delta}\sqrt{-\frac{\Im(\omega)}{\mathrm{Cr}}} = m\,\frac{\pi}{4} \quad , \qquad (m = 0,\ 1,\ 2, \ldots) \ . \tag{6.11}$$

In both these special situations, the mode spacing is proportional to $(2m+1)$Cr. More generally, expansion of (6.9) to order $\mathrm{Cr}^{-3/2}$ demonstrates that the first harmonic $(m = 1)$ is always shifted from the fundamental $(m = 0)$ by an amount proprtional to Cr. This is consistent with the finding from Case I $(\mathrm{Cr} \to \infty)$ where only the single $m = 0$ response remains and all other modes have retreated to infinity.

Figure 4a compares Case II growth rate dispersion curves at control parameter values corresponding to a stable Case I response: $\lambda = 2$ and $\delta = \sqrt{40} > \sqrt{\lambda}$ with $\mathrm{Mg} = 100$, $\Lambda = 1$ and $\Delta_\chi = 1$ (Figure 1b). For $\mathrm{Cr} \geqslant 1$ the dominant mode is stable and qualitatively similar to the Case I situation. The most obvious departure from Case I is the appearance of multiple lower lying modes whose character and interactions sensitively depend on control parameters other than viscosity ratio λ and geometry δ. In particular, at $\mathrm{Cr} = 1$ an avoided crossing is evident between the fundamental and the first harmonic, but for larger crispation number the two highest stationary modes pass through an exceptional point where a pair of spatially propagating waves are excited that travel in opposite directions with phase velocities of equal magnitude. There is also evidence in Figure 4a of a second exceptional point at higher wavenumber $(k \approx 4)$ where the superposed response splits back to two standing wave modes with distinct temporal decay rates. Moreover, at $\mathrm{Cr} = 50$ (see inset of Figure 4a) the combined oscillatory mode exhibits an *instability* of Type I in the classification Cross and coworkers (Cross & Hohenberg, 1993; Cross & Greenside, 2009). In contrast with Type-II behaviour, Type-I is characterised by the onset of instability at a *nonzero* wavenumber. For standing wave modes, Figure 4a also includes direct numerical solutions of the dispersion relation (4.13) obtained with the Matlab `fsolve` routine using the Levenberg-Marquardt algorithm (Fan, 2003). The excellent agreement serves again to verify both the analysis and the collocation method implementation. Conversely, at parameter values corresponding to an unstable response in Case I, $(\lambda = 2,\ \delta = 1/\sqrt{10},\ \mathrm{Mg} = 20,\ \Lambda = 1,\ \Delta_\chi = 1)$ increasing the interfacial tension has a stabilising effect and reduces the maximum temporal growth rate as shown in Figure 4b. The diversity of response behaviour is also apparent here with multiple splittings between states having either monotone or oscillatory time dependence in the decay rate. Excitation of spatially propagating waves is confirmed in Figure 4c where nonzero $\Re(\omega)$ appears and coincides with the linear superposition of two modes to form a stationary solution in space that oscillates in time. At very high surface tension $(\mathrm{Cr} = 0.0002)$, an unstable oscillatory response can be observed as shown in Figure 4d. An example of mode *exchange* is also apparent $(k \approx 3)$ where a single stationary mode emerges to dominate a standing wave pair without passing through an exceptional point.

The previously noted (Figure 4a) avoided-crossing or level-repulsion phenomenom (Lax, 2007) is linked with the likelihood that a given operator has eigenvalues with nontrivial algebraic multiplicity (Betcke & Trefethen, 2004). Figure 5a examines the effect more closely where, at fixed interfacial tension $\mathrm{Cr} = 0.1$, growth rate dispersion curves are plotted for $5 \leqslant \mathrm{Mg} \leqslant 100$ with $\mathrm{Eu} = 0$, $\delta = \lambda = 2$, $\Lambda = 1$ and $\Delta_\chi = 1$. As the interfacial elasticity increases, two distinct avoiding modes approach more and more closely at $k \approx 2$, then merge at a single point near $\mathrm{Mg} = 7.35$ that subsequently decomposes into a pair of exceptional points at higher Mg.

Seyranian et al. (2005) have reported a theory of strong coupling between eigenvalues of a complex valued matrix with respect to the smooth variation of parameters upon which the coefficients depend. In a finite-dimensional vector space, an exceptional point (Kato, 1980) arises where two eigenvalues

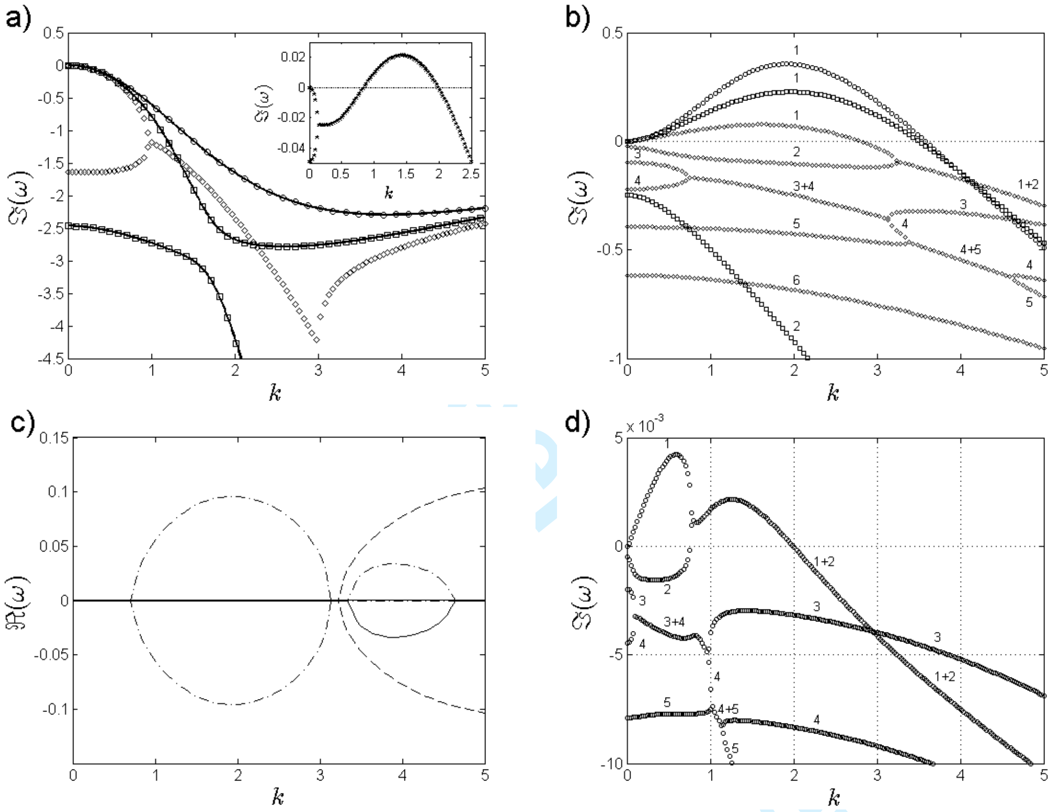

FIG. 4. Temporal frequency dispersion curves $\omega = \omega(k)$ are shown for a fluid slab of uniform mass diffusivity $(\Lambda = 1)$ and unit concentration difference on the bounding walls $\left(\Delta_\chi = 1\right)$.
Panel a): at $\mathrm{Mg} = 100$, the growth rate $\Im(\omega)$ is compared between Case I $(\mathrm{Cr} \to \infty)(\bigcirc)$ and Case II $(\mathrm{Eu} = 0)$ with finite Cr set to $1(\Box)$, $1.5(\Diamond)$ and $50(\star)$, all obtained by the collocation method (Section 5.2). Other control parameters are $\lambda = 2$ and $\delta = \sqrt{40} > \sqrt{\lambda}$ corresponding to a stable response in Case I. Solid lines correspond to evaluation of the explicit result (4.7) in Case I, and to numerical solutions of the dispersion relation (4.13) in Case II.
Panel b): at $\mathrm{Mg} = 20$, the growth rate $\Im(\omega)$ is compared between Case I $(\mathrm{Cr} \to \infty)(\bigcirc)$ and Case II $(\mathrm{Eu} = 0)$ with finite Cr set to $0.1(\Box)$ and $0.01(\Diamond)$, all obtained by the collocation method (Section 5.2). Other control parameters are $\lambda = 2$ and $\delta = 1/\sqrt{10} < \sqrt{\lambda}$ corresponding to an unstable response in Case I. Modes are identified by number and oscillatory responses are indicated by linear superposition of stationary states between a pair of exceptional points.
Panel c): the spatially propagating wave frequencies $\Re(\omega)$ are shown, corresponding to the data of panel b) for $\mathrm{Cr} = 0.01$. Modes are identified as follows: 1 and 2 $(--)$; 3 and 4 $(\cdot - \cdot)$; and 5 (——).
Panel d): shows the growth rate $\Im(\omega)$ dispersion curves, obtained by the collocation method (Section 5.2), in a situation where mass diffusion is extremely slow $\mathrm{Cr} = 0.0002$. Other control parameters are set as in panel b). Modes are identified by number. An unstable oscillatory state is observed $(k < 1)$ as well as a dominant mode exchange crossing at $k \approx 3$.

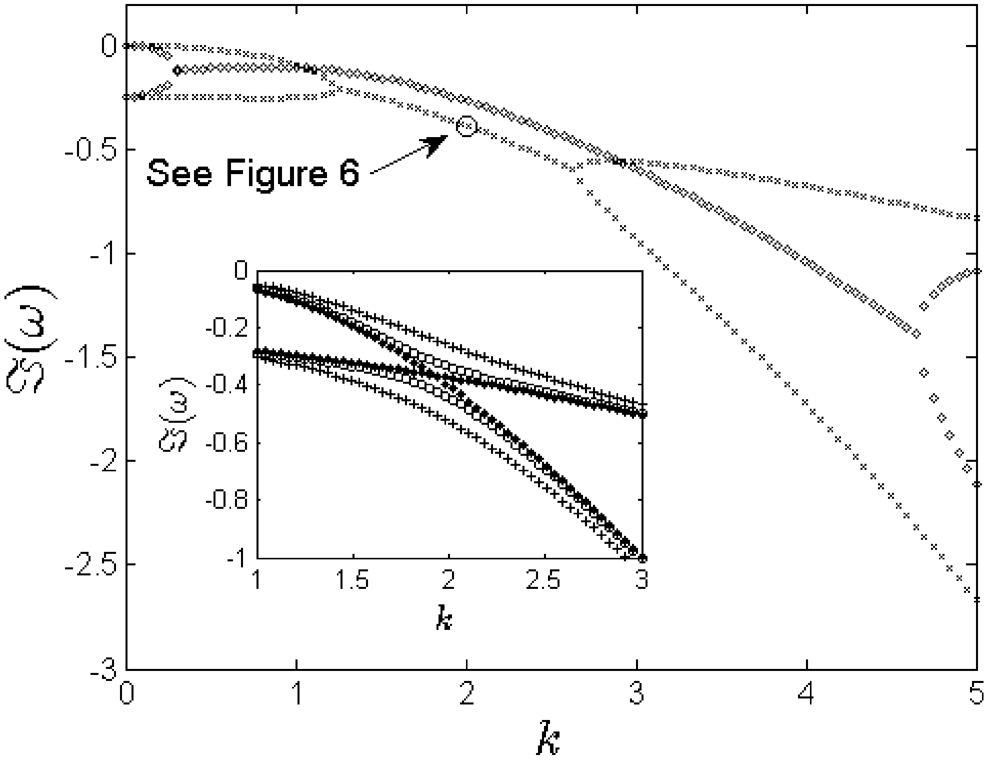

FIG. 5. Collapse of avoided crossing between stationary modes to form oscillatory mode with increasing interfacial elasticity is illustrated in panel a). Growth rate dispersion curves $\Im\big(\omega(k)\big)$ are plotted for Mg set to $5(+)$, $7(\Box)$, $7.35(\star)$, $10(\times)$ and $100(\Diamond)$. Other control parameters are $\mathrm{Ca} = 0.1$, $\mathrm{Eu} = 0$, $\delta = \lambda = 2$, $\Lambda = 1$ and $\Delta_\chi = 1$.

coalesce to give an algebraic multiplicity of 2, but a smaller geometric multiplicity of 1. Thus, the corresponding eigenvectors also merge, becoming linearly dependent and forming a nontrivial Jordan block that renders the underlying matrix defective (not diagonalizable over $\mathbb{C}$). In the situation where only a single parameter is varied (the wavenumber k for example), the two eigenvalues collide with infinite "speed" (the derivative with respect to the parameter is unbounded) and subsequently diverge in the perpendicular direction with a complete loss of information on the relationship before and after strong coupling (Seyranian et al., 2005). This phenomenon is entirely consistent with the observed behaviour (Figure 4a with $\mathrm{Cr} = 1.5$, for instance) of mode coupling between independent stationary and combined oscillatory states. Furthermore, the theory of Seyranian et al. (2005) explains characteristic properties of singularities in the surfaces representing complex resonance energy eigenvalues of quantum systems (Hernández et al., 2003) that are manifest as level repulsion in the real and imaginary parts. It remains unclear how the details of this analysis relate to avoided crossings and mode exchanges of $\Im(\omega)(k)$ in stationary states where $\Re(\omega) = 0$.

In the absence of a bulk buoyancy mechanism, and allowing for distortion of the interface, counter-rotating fluid cells are consistently observed in the stationary states (see Figure 3, for example) but the oscillatory standing wave state periodically changes the sense of rotation. The temporal evolution of this pattern is illustrated in Figure 6 by snapshots of the fluid velocity direction field over one cycle. The corresponding interfacial disturbance is also indicated and shows that the flow reversal is associated with instants where the interface adopts its unperturbed flat profile. Note that, for clarity here, the exponential decay of the disturbance in this stable response has been artifically suppressed where the spatial amplitude would otherwise be damped out within a fraction of one temporal cycle.

6.3 *Effect of base state flow* $\mathrm{Eu} > 0$ *(Case III)*

Figure 7a demonstrates the effect of a base state flow in a relatively simple situation with no mode interaction (cf. Figure 4b). The growth rates of instabilities are enhanced with increasing Eu, while a stable response is further suppressed. For the particular parameter set corresponding to Figure 4b, which is unstable in Case I, with $\mathrm{Cr} = 0.1$ it appears that the marginal stability boundary is not sensitive to changes in base state flow. At the interface, a spatially propagating wave is excited that always moves faster than the fluid $\Re(\omega)/k > u_\alpha^{(0)}$. Interestingly, we note that the second stable mode travels almost entirely without dispersion, at least over the wavenumber range $0 < k < 5$. For a more complicated situation involving mode interactions, Figure 7b shows that the symmetry-breaking base state flow destroys the standing wave of the oscillatory state. The excited propagating waves are dispersive, and the dominant mode response is always more slowly moving than the base state flow at the interface.

7. Conclusion

To investigate necessary conditions for the onset of turbulent mixing in a two-layer fluid system, the present work considers the influence of a scalar concentration field on the linear stability of a fluid interface subject to small deformations, as a means to study incipient mixing under the regime of Stokes flow. The bulk concentration field is convected by the fluid flow and acts to nonuniformly alter the interfacial tension that, in turn, induces flow by the solutal Marangoni mechanism. This treatment of the solutal Marangoni effect is formally analogous to the thermocapillary effect, which arises when an interface is exposed to a spatially-varying temperature field. In both scenarios, Marangoni tractions

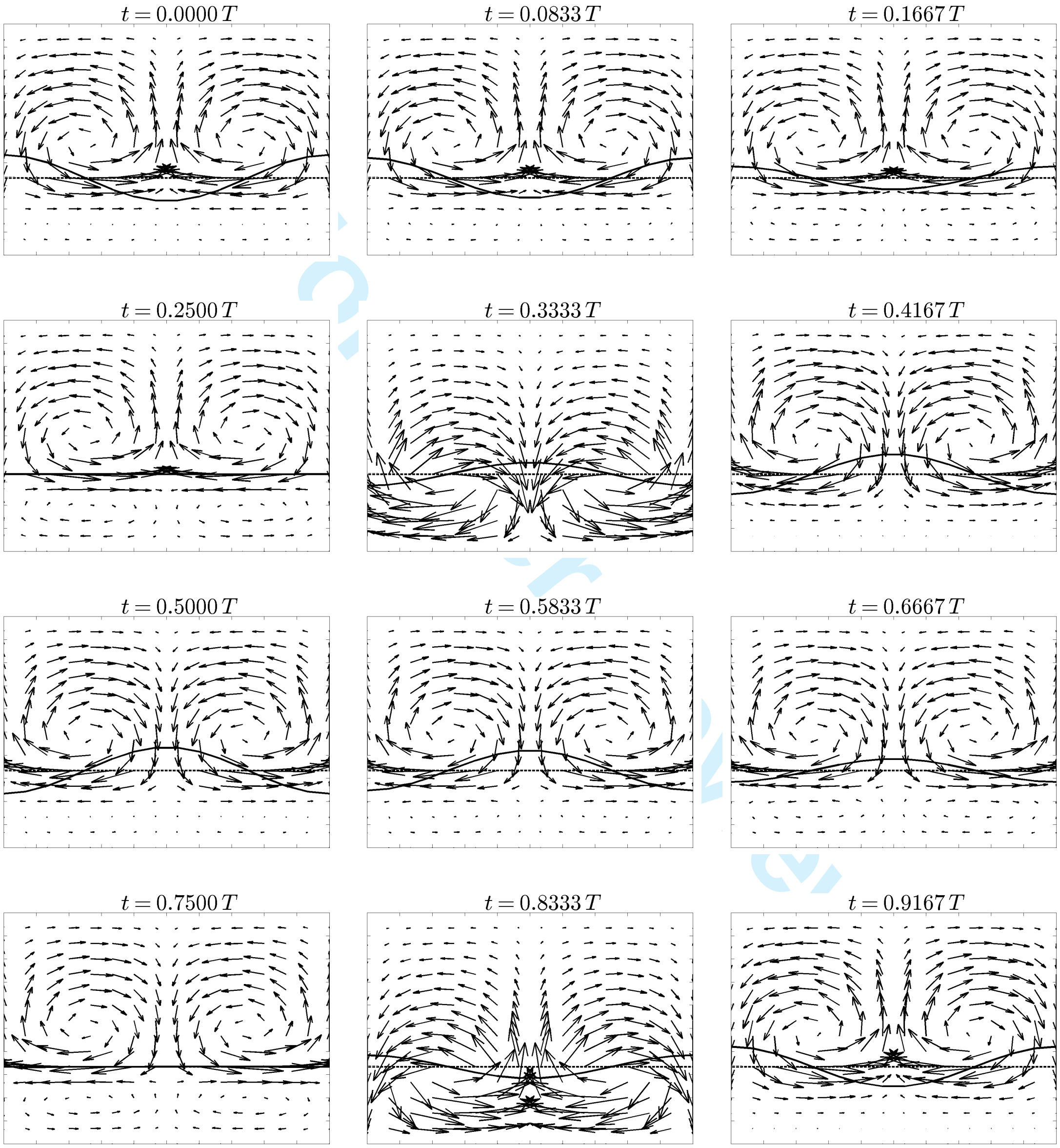

FIG. 6. Temporal evolution of flow pattern in the oscillatory state (identified in Figure 5 at parameter values, $\mathrm{Cr} = 0.1$, $\mathrm{Mg} = 10$, $\mathrm{Eu} = 0$, $\delta = 2$, $\lambda = 2$, $\Lambda = 1$ and $\Delta_\chi = 1$, at the excitation wavenumber $k = 2$. The direction field associated with the fluid velocity $\mathbf{u}(x,\ y) = u(x,\ y)\mathbf{i} + v(x,\ y)\mathbf{j}$ is plotted at time instants t expressed as fractions of the period $T = 2\pi/|\Re(\omega)|$. The superimposed lines indicate the quiescent interface position $(--)$ and the corresponding harmonic disturbance (——) of arbitrary amplitude $(\varepsilon = 0.1)$. For illustrative purposes, the exponential temporal decay of the disturbance has been suppressed, so that $\Im(\omega)$ is artificially set to zero. Axis labels have been discarded for clarity, though the abscissa ranges over $0 \leqslant kx/\pi \leqslant 2$ and the ordinate ranges over $-1 \leqslant y \leqslant 1$ throughout (cf. Figure 3).

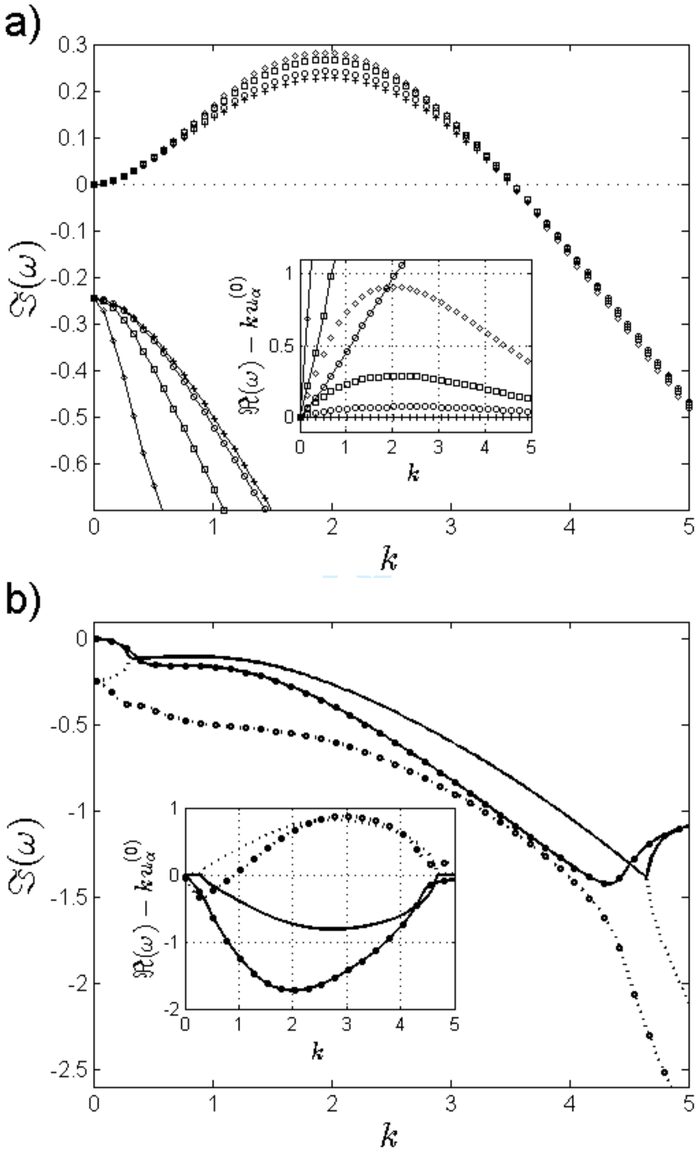

FIG. 7. Temporal frequency dispersion curves $\omega = \omega(k)$ are shown for a fluid slab of uniform mass diffusivity $(\Lambda = 1)$ and unit concentration difference on the bounding walls $\left(\Delta_\chi = 1\right)$ at crispation number $\mathrm{Cr} = 0.1$.
Panel a): the growth rate $\Im(\omega)$ is compared between Case II $(\mathrm{Eu} = 0)(+)$ and Case III with nonzero Eu set to 3(○), 10(□) and 30(◇), all obtained by the collocation method (Section 5.2). The dominant mode $(m = 1)$ is indicated by symbols alone, while the secondary mode $(m = 2)$ is denoted by symbols with solid lines. The inset shows the corresponding effective velocity $c_{\mathrm{rel}}/k = \Re(\omega) - ku_\alpha^{(0)}$ of the spatially propagating wave relative to the base state fluid speed on the interface. Other control parameters are $\lambda = 2$ and $\delta = 1/\sqrt{10} < \sqrt{\lambda}$ corresponding to an unstable response in Case I with $\mathrm{Mg} = 20$ (cf. Figure 4b).
Panel b): a similar growth rate comparison between Case II $(\mathrm{Eu} = 0)$ (no symbols) and Case III $(\mathrm{Eu} = 50)$(○) is shown. The dominant mode $(m = 1)$ is indicated by solid lines (——), while the dotted line $(\cdots)$ refers to the secondary mode $(m = 2)$. Other control parameters are $\lambda = \delta = 2$ (corresponding to a stable response in Case I) with $\mathrm{Mg} = 100$ (cf. Figure 5).

develop because of the local interfacial tension dependency on the strength of the ambient scalar field through a suitable constitutive relation. Zeren & Reynolds (1972) presented a linear stability analysis for the analogous thermocapillary problem, which also included the effect of buoyancy, but which assumed that the deformation of the interface was negligible. Interfacial deformation has been accounted for in more recent work by Tavener & Cliffe (2002) using a finite-element method. In the present work, three distinct cases were studied, and we summarise these below.

In Case I, the solute diffusion is supposed to be instantaneous (crispation number $\mathrm{Cr} \to \infty$), but a finite Gibbs elasticity $(0 < \mathrm{Mg} < \infty)$ permits interfacial displacements to generate a solutal Marangoni effect. Perturbations of the velocity and concentration fields are decoupled in this limit, so that the dispersion relation $\omega = \omega(k)$ between temporal response frequency ω and spatial excitation frequency k is obtained analytically. Furthermore, the stability behaviour is not sensitive to the mass diffusivity ratio Λ, effectively reducing the number of control parameters so that a complete stability diagram can be established. Only a single response mode is allowed where the interface is always stable to large k perturbations, but a region of unstable solutions exists at small wavenumber under certain conditions: that is a Type II instability in the classification of Cross & Hohenberg (1993). The extent of these regions is found to be independent of the base-state flow field. For $\mathrm{Mg} > 0$, the interface is Type II unstable when the viscosity ratio λ exceeds δ^2, where δ is the fluid film thickness ratio. Conversely, for $\mathrm{Mg} > 0$, unstable response is possible when $\lambda < \delta^2$. By determining the marginal stability bounds analytically, it is found that regions of global stability exist when $\mathrm{Mg} = 0$; or when $\mathrm{Mg} > 0$ and $\lambda < \delta^2$; or when $\mathrm{Mg} < 0$ and $1/\lambda < 1/\delta^2$.

Case II permits sensible interfacial tension but insists on zero Euler number $(Eu = 0)$, thereby removing the external pressure gradient and imposing a quiescent base state. Again, the dispersion relation is obtained, but the expression appears too cumbersome for analytic presentation of the stability diagram. In this case, our treatment is formally analogous to the classical linear stability analysis of the Rayleigh–Bérnard–Marangoni problem, but considers a realistic *deformable* interface leading to more complicated boundary conditions. As with the thermocapillary problem, an extremely rich discrete spectrum of modes is obtained, and several types of mode interaction are found. In particular, exceptional points exist between stationary and oscillatory standing wave solutions, but without the additional coupling between concentration and bulk mass density (that is, the solutal equivalent of the thermal buoyancy mechanism) there is no distinction between co-rotating and counter-rotating flow cells. Rather, the oscillatory state cycles between a counter-rotating pattern of four convection cells and a two-cell pattern. Furthermore, the merging of stationary states and their collapse into an avoided crossing of modes is seen as a function of control parameters, as well as evidence of resonant energy transfer and mode switching interactions between stationary and oscillatory states. Instabilities of both Type II and Type I in the Cross & Hohenberg (1993) classification are observed.

Case III is most general in that both Cr and Eu are unrestricted. A Chebyshev collocation method is implemented to solve the transport equations obeyed by the concentration perturbations. The presence of a background flow is potentially interesting because its impact on the overall system stability is not generally obvious. A surfactant induced instability such as that found in the work of Frenkel & Halpern (2002), for instance, requires a base state shear component in order for unstable solutions to develop. In our analysis, a base-state flow was neither required for unstable solutions to exist nor were the regions of instability found to be extinguished by it. The evidence suggests that an external pressure gradient driving a base state flow generally exaggerates the response: by increasing the base flow speed, unstable growth rates are enhanced, and stable decay is suppressed. By breaking the isotropic symmetry of a quiescent base state, however, standing wave solutions are no longer possible for $\mathrm{Eu} > 0$.

At zero wavenumber, the general problem also yeilds to exact analysis where an infinite discrete spectrum of purely imaginary eigenvalues is determined and the response is proven to be always stable in this limit. Consequently, Type-III instabilities (Cross & Hohenberg, 1993) are precluded in this model. Furthermore, the mode spacing increases with crispation number so that only the single trivial zero frequency mode survives in the limit Cr $\to \infty$, consistent with the Case I analysis.

Areas remaining open for further investigation include the following:

- the case of negligibly weak mass diffusion in both films where solute transport is entirely by fluid convection ($\mathrm{Cr} \to 0,\ 0 < \Lambda < \infty$) (intuition and evidence (e.g. Figure 4b) suggests that instabilities are suppressed by boundary layers developing close to the interface – a matched asymptotic analysis is required to handle change in order of the advection-diffusion equation in a non-regular limit);

- for the analogous Rayleigh–Bénard–Marangoni thermocapillary problem, the occurrence of Hopf bifurcations has been documented (Colinet & Legros, 1994) where time-dependent convection appears in a narrow transition region between stationary states. Can corresponding marginally stable bifurcation points be found in the present problem?

- what could be learned from an energy budget analysis to elucidate details of the instability mechanism (Boomkamp & Miesen, 1996; Albert & Charru, 2000; Yecko, 2008; Peng & Zhu, 2010)?

- what is the nature of the mechanism controlling the apparent transition between the appearance of two convection cells and four (see Figure 3), and how does this phenomenon relate to interfacial stability? We speculate that the interface deformation and the proximity of bounding walls are involved as recently suggested by Pozrikidis & Hill (2011).

On-going research is applying this work to exploit the capability of the Dynamic Gastric Model as a physiologically relevant screening tool for evaluating novel and existing foodstuffs, diets and pharmaceutical preparations (Rickett, 2013). This will also inform the development of more realistic prototype machines.

8. Acknowledgement

This work was partially supported by the Biotechnology and Biological Sciences Research Council through its core strategic grant to the Institute of Food Research.

9. Appendix

9.1 *General dispersion relation*

In the result (3.17) the coefficients are given by

$$
\begin{aligned}
\kappa_{\mathbf{u}} = \kappa_{\mathbf{u}}^{(0)} + k_+^2 \Big(&\big(\alpha s_1 s_{1-\alpha} - k_- s_\alpha\big)\Omega_{A2}(1) - \big(\alpha c_1 s_{1-\alpha} - k_- c_\alpha\big)\Omega_{B2}(1) \\
&- \big(s_1 s_{1-\alpha} - k_- s_\alpha\big)\Omega_{C2}(1) + \big(c_1 s_{1-\alpha} - k_- c_\alpha\big)\Omega_{D2}(1)\Big)\Lambda \\
- k_-^2 \Big(&\big(\alpha s_1 s_{1+\alpha} - k_+ s_\alpha\big)\Omega_{A1}(-1) + \big(\alpha c_1 s_{1+\alpha} + k_+ c_\alpha\big)\Omega_{B1}(-1) \\
&- \big(s_1 s_{1+\alpha} + k_+ s_\alpha\big)\Omega_{C1}(-1) - \big(c_1 s_{1+\alpha} - k_+ c_\alpha\big)\Omega_{D1}(-1)\Big)\lambda \ ,
\end{aligned}
$$

$$
\begin{aligned}
\kappa_{\perp\boldsymbol{\sigma}} = \kappa_{\perp\boldsymbol{\sigma}}^{(0)} &+ \left(s_{1+\alpha}^2 - k_+^2\right)\Big(\left(\alpha s_1 s_{1-\alpha} - k_- s_\alpha\right)\Omega_{A2}(1) - \left(\alpha c_1 s_{1-\alpha} - k_- c_\alpha\right)\Omega_{B2}(1) \\
&\qquad - \left(s_1 s_{1-\alpha} - k_- s_\alpha\right)\Omega_{C2}(1) + \left(c_1 s_{1-\alpha} - k_- c_\alpha\right)\Omega_{D2}(1)\Big)\Lambda \\
&- \left(s_{1-\alpha}^2 - k_-^2\right)\Big(\left(\alpha s_1 s_{1+\alpha} - k_+ s_\alpha\right)\Omega_{A1}(-1) + \left(\alpha c_1 s_{1+\alpha} + k_+ c_\alpha\right)\Omega_{B1}(-1) \\
&\qquad - \left(s_1 s_{1+\alpha} + k_+ s_\alpha\right)\Omega_{C1}(-1) - \left(c_1 s_{1+\alpha} - k_+ c_\alpha\right)\Omega_{D1}(-1)\Big) \ ,
\end{aligned}
$$

$$
\kappa_{\parallel\boldsymbol{\sigma}} = k_-^2\left(s_{1+\alpha}^2 - k_+^2\right)\lambda - k_+^2\left(s_{1-\alpha}^2 - k_-^2\right) \ ,
$$

$$
\begin{aligned}
\kappa_\eta = \kappa_\eta^{(0)} &+ 2\left(c_1 s_1 - k\right)\Big(\left(\alpha s_1 s_{1-\alpha} + k_- s_\alpha\right)\Omega_{A1}(-1) - \left(c_1 s_{1-\alpha} + k_- c_\alpha\right)\Omega_{D1}(-1) \\
&\qquad - \left(\alpha s_1 s_{1+\alpha} + k_+ s_\alpha\right)\Lambda\Omega_{A2}(1) - \left(c_1 s_{1+\alpha} + k_+ c_\alpha\right)\Lambda\Omega_{D2}(1)\Big) \\
&+ 2\left(c_1 s_1 + k\right)\Big(\left(\alpha c_1 s_{1-\alpha} + k_- c_\alpha\right)\Omega_{B1}(-1) - \left(s_1 s_{1-\alpha} + k_- s_\alpha\right)\Omega_{C1}(-1) \\
&\qquad + \left(\alpha c_1 s_{1+\alpha} - k_+ c_\alpha\right)\Lambda\Omega_{B2}(1) + \left(s_1 s_{1+\alpha} - k_+ s_\alpha\right)\Lambda\Omega_{C2}(1)\Big) \\
&+ (\lambda - 1)\Big[2\left(c_1 s_1 - k\right)\Big(\left(\alpha s_1 s_{1-\alpha} + k_- s_\alpha\right)\Omega_{A1}(-1) - \left(c_1 s_{1-\alpha} + k_- c_\alpha\right)\Omega_{D1}(-1)\Big) \\
&\qquad + 2\left(c_1 s_1 + k\right)\Big(\left(\alpha c_1 s_{1-\alpha} + k_- c_\alpha\right)\Omega_{B1}(-1) - \left(s_1 s_{1-\alpha} + k_- s_\alpha\right)\Omega_{C1}(-1)\Big) \\
&\quad - \left(s_{1+\alpha}^2 - k_+^2\right)\Big(\left(\alpha s_1 c_{1-\alpha} + k_- c_\alpha\right)\Omega_{A2}(1) - \left(\alpha c_1 c_{1-\alpha} + k_- s_\alpha\right)\Omega_{B2}(1) \\
&\qquad - \left(s_1 c_{1-\alpha} + k_- c_\alpha\right)\Omega_{C2}(1) + \left(c_1 c_{1-\alpha} + k_- s_\alpha\right)\Omega_{D2}(1)\Big)\Lambda \\
&\quad - \left(s_{1-\alpha}^2 - k_-^2\right)\Big(\left(\alpha s_1 c_{1+\alpha} - k_+ c_\alpha\right)\Omega_{A1}(-1) - \left(\alpha c_1 c_{1+\alpha} + k_+ s_\alpha\right)\Omega_{B1}(-1) \\
&\qquad - \left(s_1 c_{1+\alpha} + k_+ c_\alpha\right)\Omega_{C1}(-1) - \left(c_1 c_{1+\alpha} - k_+ s_\alpha\right)\Omega_{D1}(-1)\Big)\Big] \ ,
\end{aligned} \tag{9.1}
$$

where the contributions independent of the chemical fields are:

$$
\begin{aligned}
\kappa_{\mathbf{u}}^{(0)} &= -\Big(k_+^2\left(c_{1-\alpha} s_{1-\alpha} - k_-\right) + k_-^2\left(c_{1+\alpha} s_{1+\alpha} - k_+\right)\Big)\lambda \ , \\
\kappa_{\perp\boldsymbol{\sigma}}^{(0)} &= -\Big(\left(s_{1+\alpha}^2 - k_+^2\right)\left(c_{1-\alpha} s_{1-\alpha} - k_-\right)\lambda + \left(s_{1-\alpha}^2 - k_-^2\right)\left(c_{1+\alpha} s_{1+\alpha} - k_+\right)\Big) \ , \\
\kappa_\eta^{(0)} &= \mathscr{A}_{k,\alpha}(\lambda - 1)^2 + 2\mathscr{B}_{k,\alpha}(\lambda - 1) + \mathscr{C}_k \ ,
\end{aligned} \tag{9.2}
$$

$$
\begin{aligned}
\mathscr{A}_{k,\alpha} &= \left(s_{1+\alpha}^2 - k_+^2\right)\left(c_{1-\alpha}^2 + k_-^2\right) \ , \\
\mathscr{B}_{k,\alpha} &= \mathscr{A}_{k,\alpha} + \left(k_+ k_-\right)^2 + \frac{1}{4}\Big(s_{2(1+\alpha)} s_{2(1-\alpha)} - \left(2k_+\right)\left(2k_-\right)\Big) \ , \\
\mathscr{C}_k &= s_2^2 - (2k)^2 \ .
\end{aligned}
$$

Coupling terms between the flow and the chemical field involve the determinant-like functions

$$\mathscr{L}_{k,\alpha}(\Lambda) = \det \begin{pmatrix} \det \begin{pmatrix} \Psi_1(-1) & \Psi_1(\alpha) \\ \Phi_1(-1) & \Phi_1(\alpha) \end{pmatrix} & \det \begin{pmatrix} \Psi_2(1) & \Psi_2(\alpha) \\ \Phi_2(1) & \Phi_2(\alpha) \end{pmatrix} \\ \\ \mathscr{W}\big(\Psi_1(-1),\ \Phi_1(\alpha)\big) & \Lambda\, \mathscr{W}\big(\Psi_2(1),\ \Phi_2(\alpha)\big) \end{pmatrix}, \tag{9.3}$$

with $\mathscr{W}$ defined by (3.14) and

$$\Omega_{X\,j}(y) = \frac{k}{\Psi_j(y)\mathscr{L}_{k,\alpha}(\Lambda)} \det \begin{pmatrix} \Psi_{3-j}(-y) & \Psi_{3-j}(\alpha) \\ \Phi_{3-j}(-y) & \Phi_{3-j}(\alpha) \end{pmatrix}$$
$$\times \det \begin{pmatrix} \det \begin{pmatrix} \Psi_j(y) & \Psi_j(\alpha) \\ \mathscr{I}_{X\,j}(y) & \mathscr{I}_{X\,j}(\alpha) \end{pmatrix} & \det \begin{pmatrix} \Psi_j(y) & \Psi_j(\alpha) \\ \Phi_j(y) & \Phi_j(\alpha) \end{pmatrix} \\ \\ \mathscr{W}\big(\Psi_j(y),\ \mathscr{I}_{X\,j}(\alpha)\big) & \mathscr{W}\big(\Psi_j(y),\ \Phi_j(\alpha)\big) \end{pmatrix}. \tag{9.4}$$

9.2 *Case II dispersion relation*

In the result (4.13) the coefficients are given by:

$$\kappa^{(1)}_{\perp\boldsymbol{\sigma}} = \kappa^{(0)}_{\perp\boldsymbol{\sigma}} - \mathrm{Mg}\,\mathrm{Cr}\, \frac{(1+\delta)\Lambda}{2(\delta+\Lambda)}\, \frac{1}{\mathscr{L}^{(1)}_{k,\alpha}(\Lambda)} \left(\frac{k}{\omega}\right)^2 \times$$
$$\times \Bigg(S_{1,1+\alpha}\big(s^2_{1+\alpha} - k^2_+\big)\Big(K_2 k_-\big(C_{2,1-\alpha} - c_{1-\alpha}\big) + \Big(kS_{2,1-\alpha}s_{1-\alpha} - K_2\big(C_{2,1-\alpha}c_{1-\alpha} - 1\big)\Big)s_{1-\alpha}\Big)\Lambda$$
$$- S_{2,1-\alpha}\big(s^2_{1-\alpha} - k^2_-\big)\Big(K_1 k_+\big(C_{1,1+\alpha} - c_{1+\alpha}\big) + \Big(kS_{1,1+\alpha}s_{1+\alpha} - K_1\big(C_{1,1+\alpha}c_{1+\alpha} - 1\big)\Big)s_{1+\alpha}\Big)\Bigg) ,$$

$$\kappa^{(1)}_{\eta} = \kappa^{(0)}_{\eta} - \mathrm{Mg}\, \frac{(1+\delta)\Lambda}{4(\delta+\Lambda)}\, \frac{1}{\mathscr{L}^{(1)}_{k,\alpha}(\Lambda)} \left(\frac{1}{\omega}\right) \times$$
$$\times \Bigg(\big(K_1 C_{1,1+\alpha}S_{2,1-\alpha} + K_2 C_{2,1-\alpha}S_{1,1+\alpha}\big)\big(k^2_+ s^2_{1-\alpha} - k^2_- s^2_{1+\alpha}\big)\, i$$
$$+ (\lambda - 1)\Big(2kS_{1,1+\alpha}S_{2,1-\alpha}\Big(k^2_+\big(c_{1-\alpha}s_{1-\alpha} + k_-\big) + k^2_-\big(c_{1+\alpha}s_{1+\alpha} + k_+\big)\Big)$$
$$- \big(K_1 C_{1,1+\alpha}S_{2,1-\alpha} + K_2 C_{2,1-\alpha}S_{1,1+\alpha}\big)k^2_-\big(s^2_{1+\alpha} - k^2_+\big)\Big)\, i\Bigg)$$
$$- \mathrm{Mg}\,\mathrm{Cr}\, \frac{(1+\delta)\Lambda}{2(\delta+\Lambda)}\, \frac{1}{\mathscr{L}^{(1)}_{k,\alpha}(\Lambda)} \left(\frac{k}{\omega^2}\right) \times$$
$$\times \Bigg(2K_2 S_{1,1+\alpha}\Big(\Big(k\big(C_{2,1-\alpha}c_\alpha - c_1\big) + K_2 S_{2,1-\alpha}s_\alpha\Big)\big(c_1 s_{1+\alpha} + k_+ c_\alpha\big)\big(c_1 s_1 - k\big)$$

$$
\begin{aligned}
&\qquad -\Big(k\big(C_{2,1-\alpha}s_\alpha - s_1\big) + K_2 S_{2,1-\alpha}c_\alpha\Big)\big(s_1 s_{1+\alpha} - k_+ s_\alpha\big)\big(c_1 s_1 + k\big)\Big)\Lambda \\
&\quad - 2K_1 S_{2,1-\alpha}\Big(\Big(k\big(C_{1,1+\alpha}c_\alpha - c_1\big) - K_1 S_{1,1+\alpha}s_\alpha\Big)\big(c_1 s_{1-\alpha} + k_- c_\alpha\big)\big(c_1 s_1 - k\big) \\
&\qquad + \Big(k\big(C_{1,1+\alpha}s_\alpha + s_1\big) - K_1 S_{1,1+\alpha}c_\alpha\Big)\big(s_1 s_{1-\alpha} + k_- s_\alpha\big)\big(c_1 s_1 + k\big)\Big) \\
&+ (\lambda - 1)\Big(K_2 S_{1,1+\alpha}\big(s_{1+\alpha}^2 - k_+^2\big)\times \\
&\qquad \times\Big(\big(kC_{2,1-\alpha}c_{1-\alpha} - K_2 S_{2,1-\alpha}s_{1-\alpha} - k\big)c_{1-\alpha} + k_-\big(ks_{1-\alpha} - K_2 S_{2,1-\alpha}\big)\Big)\Lambda \\
&\qquad + K_1 S_{2,1-\alpha}\big(s_{1-\alpha}^2 - k_-^2\big)\times \\
&\qquad \times\Big(\big(kC_{1,1+\alpha}c_{1+\alpha} - K_1 S_{1,1+\alpha}s_{1+\alpha} - k\big)c_{1+\alpha} + k_+\big(ks_{1+\alpha} - K_1 S_{1,1+\alpha}\big)\Big) \\
&\qquad + K_1 S_{2,1-\alpha}\times \\
&\qquad \times\Big(2k^2 k_-\big(C_{1,1+\alpha} - c_{1+\alpha}\big)k_+ s_{1-\alpha} + \big(kC_{1,1+\alpha}c_{1-\alpha} + K_1 S_{1,1+\alpha}s_{1-\alpha} - kc_2\big)k_+ s_{1-\alpha} \\
&\qquad - \big(kC_{1,1+\alpha}c_{1+\alpha} - K_1 S_{1,1+\alpha}s_{1+\alpha} - k\big)\big(s_2 s_{1-\alpha} + k_- s_{1+\alpha}\big)\Big)\Big)\Big)\ .
\end{aligned}
\tag{9.5}
$$

9.3 *Proof* $\kappa_\eta^{(0)} > 0$

First note the obvious fact, if $a,\ b,\ c > 0$ then $a\lambda^2 + 2b\lambda + c > 0$ for all $\lambda > 0$. It follows that, if $b > a > 0$ and $a - 2b + c > 0$ then

$$a\lambda^2 + 2(b-a)\lambda + a - 2b + c = a(\lambda-1)^2 + 2b(\lambda-1) + c > 0 \ \text{ for all } \ \lambda > 0\ . \tag{9.6}$$

For the “jump” term J_η, the coefficient $\kappa_\eta^{(0)}$ is a quadratic function of $(\lambda - 1)$ thus

$$\kappa_\eta^{(0)} = \mathscr{A}_{k,\alpha}(\lambda-1)^2 + 2\mathscr{B}_{k,\alpha}(\lambda-1) + \mathscr{C}_k\ , \tag{9.7}$$

where

$$
\begin{gathered}
\mathscr{A}_{k,\alpha} = \big(s_{1+\alpha}^2 - k_+^2\big)\big(c_{1-\alpha}^2 + k_-^2\big)\ , \\
\mathscr{B}_{k,\alpha} = \mathscr{A}_{k,\alpha} + \big(k_+k_-\big)^2 + \frac{1}{4}\Big(s_{2(1+\alpha)}s_{2(1-\alpha)} - \big(2k_+\big)\big(2k_-\big)\Big)\ , \\
\mathscr{C}_k = s_2^2 - (2k)^2\ .
\end{gathered}
\tag{9.8}
$$

By virtue of the fact that $\xi > 0$ implies $\sinh(\xi) > \xi$, we immediately observe

$$\mathscr{B}_{k,\alpha} > \mathscr{A}_{k,\alpha} > 0\ ,\ \ \mathscr{C}_k > 0\ , \tag{9.9}$$

for all physically relevant parameter values. Furthermore we find

$$\mathscr{A}_{k,\alpha} - 2\mathscr{B}_{k,\alpha} + \mathscr{C}_k = \left(c_{1+\alpha}^2 + k_+^2\right)\left(s_{1-\alpha}^2 - k_-^2\right) > 0 \ . \tag{9.10}$$

So (9.7) satisfies the conditions for inequality (9.6). Hence, $\kappa_\eta^{(0)} > 0$ for all $\lambda > 0$ as claimed.

9.4 *Proof in Case I* $\Re(\omega) \geqslant 0$

The argument follows the same structure as Section 9.3. Recall, in case $\mathrm{Cr} \to \infty$, the real part of the temporal frequency may be written proportional to a quadratic function in $(\lambda - 1)$ thus

$$\Re(\omega) = \frac{\mathrm{Eu}}{\kappa_\eta^{(0)}(1+\delta)(\delta+\lambda)} \left(\mathscr{A}'_{k,\alpha}(\lambda-1)^2 + 2\mathscr{B}'_{k,\alpha}(\lambda-1) + \mathscr{C}'_k\right) \ , \tag{9.11}$$

where

$$\begin{gathered}\mathscr{A}'_{k,\alpha} = \mathscr{U}_{k,\alpha} + 2k\delta\mathscr{A}_{k,\alpha} \ , \ \ \mathscr{B}'_{k,\alpha} = \tfrac{1}{2}\left(1-\delta^2\right)\mathscr{U}_{k,\alpha} + 2k\delta\mathscr{B}_{k,\alpha} \ , \ \ \mathscr{C}'_k = 2k\delta\mathscr{C}_k \ , \\ \text{with} \qquad \mathscr{U}_{k,\alpha} = k_+^2\left(c_{1-\alpha}s_{1-\alpha} - k_-\right) + k_-^2\left(c_{1+\alpha}s_{1+\alpha} - k_+\right) \ . \end{gathered} \tag{9.12}$$

Evidently, $\mathscr{U}_{k,\alpha} > 0$ and we find

$$\begin{aligned} k_+^2\left(\mathscr{B}'_{k,\alpha} - \mathscr{A}'_{k,\alpha}\right) &= k_+k_-\left(\mathscr{U}_{k,\alpha} + \left(k_+ + k_-\right)\left(\left(k_+k_-\right)^2 + \left(c_{1-\alpha}s_{1-\alpha} - k_-\right)\left(c_{1+\alpha}s_{1+\alpha} - k_+\right)\right)\right) \\ &\quad + \left(k_+k_-\right)^2\left(k_+ + k_-\right)\left(k_+ - k_-\right)^2 \sum_{n=0}^{\infty} \frac{2^{2n+1}}{(2n+1)!} \sum_{m=0}^{2n} k_+^{2n-m}k_-^m \\ &> 0 \ , \end{aligned} \tag{9.13}$$

whence

$$\mathscr{B}'_{k,\alpha} > \mathscr{A}'_{k,\alpha} > 0 \ . \tag{9.14}$$

Furthermore,

$$\mathscr{A}'_{k,\alpha} - 2\mathscr{B}'_{k,\alpha} + \mathscr{C}'_k = \delta^2\mathscr{U}_{k,\alpha} + 2k\delta\left(\mathscr{A}_{k,\alpha} - 2\mathscr{B}_{k,\alpha} + \mathscr{C}_k\right) > 0 \ , \tag{9.15}$$

where the result of Section 9.3 has been used. Hence, as claimed $\mathrm{Eu} > 0$ implies $\Re(\omega) > 0$ for all $\lambda > 0$, while $\Re(\omega) = 0$ if $\mathrm{Eu} = 0$.

9.5 *Proof* $k = 0$ *implies* $\Re(\omega) = 0$ *and* $\Im(\omega) \leqslant 0$

From the dispersion relation (5.18), we will deduce restrictions on the temporal frequency ω in the situation of vanishing wavenumber ($k = 0$). First recall the definitions (5.19):

$$\begin{gathered} h_- = \frac{2\delta}{(1+\delta)\sqrt{\Lambda}} = \frac{1-\alpha}{\sqrt{\Lambda}} > 0 \ ; \ h_+ = \frac{2}{1+\delta} = 1+\alpha > 0 \\ \text{and} \qquad K_0 = \sqrt{-i\omega/\mathrm{Cr}} = \Re\left(K_0\right) + i\,\Im\left(K_0\right) \in \mathbb{C} \end{gathered} \tag{9.16}$$

In particular,

$$\Re\left(K_0\right) = \sqrt{\frac{|\omega| + \Im(\omega)}{2\ \mathrm{Cr}}} \ , \tag{9.17}$$

so that

$$\begin{aligned} &\Re\big(K_0\big)=0 \quad\Rightarrow\quad |\omega|+\Im(\omega)=0 \\ \Rightarrow\quad \Im(\omega)\leqslant 0 \quad&\text{and}\quad \big(\Im(\omega)\big)^2=\big(\Re(\omega)\big)^2+\big(\Im(\omega)\big)^2 \quad\Rightarrow\quad \Re(\omega)=0\ , \end{aligned} \tag{9.18}$$

since $|\omega|\geqslant 0$. Thus, it suffices to show that the dispersion relation (5.18) implies $\Re\big(K_0\big)=0$.

For the sake of contradiction, suppose that $\Re\big(K_0\big)\neq 0$ while (5.18) holds. Now define

$$\hat{\mathscr{L}}^{(1)}_{0,\alpha}=\frac{\mathscr{L}^{(1)}_{0,\alpha}}{K_0\cosh\big(\Re(K_0)h_-\big)\cosh\big(\Re(K_0)h_+\big)}\ , \tag{9.19}$$

so that

$$\begin{aligned} \Re\big(\hat{\mathscr{L}}^{(1)}_{0,\alpha}\big)&=T_-\big(c_-c_+-s_-s_+\sqrt{\Lambda}\big)+T_+\big(c_-c_+\sqrt{\Lambda}-s_-s_+\big)\ , \\ \Im\big(\hat{\mathscr{L}}^{(1)}_{0,\alpha}\big)&=T_-T_+\big(c_+s_-\sqrt{\Lambda}+c_-s_+\big)+\big(c_-s_+\sqrt{\Lambda}+c_+s_-\big)\ , \end{aligned} \tag{9.20}$$

where

$$T_\pm=\tanh\big(\Re(K_0)h_\pm\big)\ ,\ \ c_\pm=\cos\big(\Im(K_0)h_\pm\big)\ ,\ \ s_\pm=\sin\big(\Im(K_0)h_\pm\big)\ . \tag{9.21}$$

Since $\Re(K_0)\neq 0$ implies $T_-T_+>0$, then $\hat{\mathscr{L}}^{(1)}_{0,\alpha}=0$ demands the bracketed terms in (9.20) either both vanish or are non-zero with opposite sign, so that

$$\begin{aligned} \Re\big(\hat{\mathscr{L}}^{(1)}_{0,\alpha}\big)=0 \quad&\Rightarrow\quad \big(c_-c_+-s_-s_+\sqrt{\Lambda}\big)\big(c_-c_+\sqrt{\Lambda}-s_-s_+\big)\leqslant 0\ , \\ &\Rightarrow\quad 0\leqslant\frac{\sqrt{\Lambda}}{1+\Lambda}\Big(\big(c_-c_+\big)^2+\big(s_-s_+\big)^2\Big)\leqslant c_-s_-c_+s_+\ , \end{aligned} \tag{9.22}$$

$$\begin{aligned} \Im\big(\hat{\mathscr{L}}^{(1)}_{0,\alpha}\big)=0 \quad&\Rightarrow\quad \big(c_+s_-\sqrt{\Lambda}+c_-s_+\big)\big(c_-s_+\sqrt{\Lambda}+c_+s_-\big)\leqslant 0\ , \\ &\Rightarrow\quad c_-s_-c_+s_+\leqslant-\frac{\sqrt{\Lambda}}{1+\Lambda}\Big(\big(c_-s_+\big)^2+\big(c_+s_-\big)^2\Big)\leqslant 0\ . \end{aligned} \tag{9.23}$$

Together, the conditions (9.22) and (9.23) require

$$c_-s_-c_+s_+=0\ . \tag{9.24}$$

Now consider the magnitude

$$\begin{aligned} \big|\hat{\mathscr{L}}^{(1)}_{0,\alpha}\big|^2&=\big(c_-c_+\big)^2\big(T_-+T_+\sqrt{\Lambda}\big)^2+\big(c_-s_+\big)^2\big(T_-T_++\sqrt{\Lambda}\big)^2 \\ &\quad+\big(c_+s_-\big)^2\big(T_-T_+\sqrt{\Lambda}+1\big)^2+\big(s_-s_+\big)^2\big(T_-\sqrt{\Lambda}+T_+\big)^2\ , \end{aligned} \tag{9.25}$$

where (9.24) has been used, and observe that $\big|\hat{\mathscr{L}}^{(1)}_{0,\alpha}\big|=0$ requires

$$c_-c_+=c_-s_+=c_+s_-=s_-s_+=0\ , \tag{9.26}$$

again because $T_-T_+>0$. Finally, define

$$\Delta=\Im\big(K_0\big)\ \big(h_+-h_-\big)\ \in\ \mathbb{R}\ , \tag{9.27}$$

and deduce that

$$\begin{aligned} c_-c_+ = s_-s_+ = 0 \quad &\Rightarrow \quad \cos\Delta = 0 \ , \\ c_-s_+ = c_+s_- = 0 \quad &\Rightarrow \quad \sin\Delta = 0 \ . \end{aligned} \tag{9.28}$$

But there is no real number Δ simultaneously satisfying both conditions (9.28). Hence, by contradiction, we conclude $\Re\big(K_0\big) = 0$ as required.

REFERENCES

Abramowitz, M. & Stegun, I. A. (1965) *Handbook of Mathematical Functions*. Dover Publications, New York, ninth edition.

Albert, F. & Charru, F. (2000) Small Reynolds number instabilities in two-layer Couette flow. *Eur. J. Mech. B: Fluids*, **19**, 229–252.

Andereck, C. D., Colovas, P. W., Degen, M. M. & Renardy, Y. Y. (1998) Instabilities in two layer Rayleigh–Bénard convection: overview and outlook. *Int. J. Eng. Sci.*, **36**, 1451–1470.

Anturkar, N. R., Papanastasiou, T. C. & Wilkes, J. O. (1990) Linear stability analysis of multilayer plane Poiseuille flow. *Phys. Fluids A*, **2**, 530–541.

Betcke, T. & Trefethen, L. N. (2004) Computations of eigenvalue avoidance in planar domains. *Manchester Inst. Math. Sci., MIMS EPrint*, 2006.366.

Blyth, M. G. & Pozrikidis, C. (2004a) Effect of surfactants on the stability of two-layer channel flow. *J. Fluid Mech.*, **505**, 59–86.

Blyth, M. G. & Pozrikidis, C. (2004b) Effect of surfactant on the stability of film flow down an inclined plane *J. Fluid Mech.*, **521**, 241–250.

Blyth, M. G. & Pozrikidis, C. (2004c) Effect of inertia on the Marangoni instability of two-layer channel flow, part II: normal-mode analysis. *J. Eng. Math.*, **50**, 329–341.

Bodenschatz, E., Pesch, W. & Ahlers, G. (2000) Recent developments in Rayleigh–Bénard convection. *Ann. Rev. Fluid Mech.*, **32**, 709–778.

Boomkamp, P. A. M. & Miesen, R. H. M. (1996) Classification of instabilities in parallel two-phase flow. *Int. J. Multiphase Flow*, **22**, S67–S88.

Braverman, L. M., Eckert, K., Nepomnyashchy, A. A., Simanovskii, I. B. & Thess, A. (2000) Convection in two-layer systems with an anomalous thermocapillary effect. *Phys. Rev. E*, **62**, 3619–3631.

Cartwright, J. H. E., Gouillart, E., Piro, N., Piro, O. & Tuval, I. (2012) Geometric mixing. `http://arxiv.org/abs/1206.6894`.

Charru, F. (2011) *Hydrodynamic Instabilities*. Cambridge University Press, Cambridge.

Charru, F. & Hinch, E. J. (2000) 'Phase diagram' of interfacial instabilities in a two-layer Couette flow and mechanism of the long-wave instability. *J. Fluid Mech.*, **414**, 195–223.

Colinet, P. & Legros, J. C. (1994) On the Hopf bifurcation occurring in the two-layer Rayleigh–Bénard convective instability. *Phys. Fluids*, **6**, 2631–2639.

Coward, A. V., Renardy, Y. Y., Renardy, M. & Richards, J. R. (1997) Temporal evolution of periodic disturbances in two-layer Couette flow. *J. Comp. Phys.*, **132**, 346–361.

Cross, M. & Greenside, H. (2009) *Pattern Formation and Dynamics in Nonequilibrium Systems*. Cambridge University Press, Cambridge.

Cross, M. C. & Hohenberg, P. C. (1993) Pattern formation outside of equilibrium. *Rev. Mod. Phys.*, **65**, 851–1112.

Drazin, P. G. (2002) *Introduction to Hydrodynamic Stability*. Cambridge University Press, Cambridge.

Drazin, P. G. & Reid, W. H. (2004) *Hydrodynamic Stability*. Cambridge University Press, Cambridge, second edition.

Edwards, D. A., Brenner, H. & Wasan, D. T. (1991) *Interfacial Transport Processes and Rheology*. Butterworth-Heinemann, Boston.

Fan, J.-Y. (2003) A modified Levenberg-Marquardt algorithm for singular system of nonlinear equations. *J. Comp. Math.*, **21**, 625–636.

Frenkel, A. L. & Halpern, D. (2002) Stokes-flow instability due to interfacial surfactant. *Phys. Fluids*, **14**, L45–L48.

Frenkel, A. L. & Halpern, D. (2005) Effect of inertia on the insoluble-surfactant instability of a shear flow. *Phys. Rev. E*, **71**, 016302, 1–10.

Gao, P. & Lu, X.-Y. (2007) Effect of surfactants on the inertialess instability of a two-layer film flow. *J. Fluid Mech.*, **591**, 495–507.

Gottleib, D. & Orszag, S. A. (1977) *Numerical Analysis of Spectral Methods: Theory and Applications*. SIAM, Bristol.

Halpern, D. & Frenkel, A. L. (2003) Destabilization of a creeping flow by interfacial surfactant: linear theory extended to all wavenumbers. *J. Fluid Mech.*, **485**, 191–220.

Hernández, E., Jáuregui, A. & Mondragón, A. (2003) Unfolding a degeneracy point: crossings and anticrossings of unbound states in parameter space. *Rev. Mex. Fis.*, **49**, 60–72.

Hinch, E. J. (1984) A note on the mechanism of the instability at the interface between two shearing fluids. *J. Fluid Mech.*, **144**, 463–465.

Hooper, A. P. (1985) Long-wave instability at the interface between two viscous fluids: thin layer effects. *Phys. Fluids*, **28**, 1613–1618.

Hooper, A. P. & Boyd, W. G. C. (1983) Shear-flow instability at the interface between two viscous fluids. *J. Fluid Mech.*, **128**, 507–528.

Johnson, D. & Narayanan, R. (1997) Geometric effects on convective coupling and interfacial structures in bilayer convection. *Phys. Rev. E*, **56**, 5462–5472.

Kato, T. (1980) *Perturbation Theory for Linear Operators*. Springer-Verlag, Berlin, second edition.

Kong, F. & Singh, R. P. (2008) Disintegration of solid foods in human stomach. *J. Food Sci.*, **73**, R67–R80.

Koschmieder, E. L. (1974) Bénard convection. *Adv. Chem. Phys.*, **26**, 177–212.

Lax, P. D. (2007) *Linear Algebra and its Applications*. Wiley and Sons, New York, second edition.

Li, X. & Pozrikidis, C. (1997) The effect of surfactants on drop deformation and on the rheology of dilute emulsions in Stokes flow. *J. Fluid Mech.*, **341**, 165–194.

Li, J. & Renardy, Y. (2000) Numerical study of flows of two immiscible liquids at low Reynolds number. *SIAM Review*, **42**, 417–439.

MATLAB (2013) *Version R2013a (8.1.0.604)*. The Mathworks Inc., Natick, Massachusetts.

Mercuri, A., Passalacqua, A., Wickham, M. S. J., Faulks, R. M., Craig, D. Q. M. & Barker, S. (2011) The effect of composition and gastric conditions on the self-emulsification process of ibuprofen-loaded self-emulsifying drug delivery systems: a microscopic and Dynamic Gastric Model study. *Pharm. Res.*, **28**, 1540–1551.

Normand, C., Pomeau, Y. & Velarde, M. G. (1977) Convective instability: a physicist's approach. *Rev. Mod. Phys.*, **49**, 581–624.

Pal, A., Brasseur, J. G. & Abrahamsson, B. (2007) A stomach road or "Magenstrasse" for gastric emptying. *J. Biomech.*, **40**, 1202–1210.

Palmer, H. J. & Berg, J. C. (1972) Hydrodynamic stability of surfactant solutions heated from below. *J. Fluid Mech.*, **51**, 385–402.

Peng, J. & Zhu, K.-Q. (2010) Linear instability of two-fluid Taylor–Couette flow in the presence of surfactant. *J. Fluid Mech.*, **651**, 357–385.

Pozrikidis, C. (1997) Instability of two-layer creeping flow in a channel with parallel-sided walls. *J. Fluid Mech.*, **351**, 139–165.

Pozrikidis, C. (2004) Effect of inertia on the Marangoni instability of two-layer channel flow, part I: numerical simulations. *J. Eng. Math.*, **50**, 311–327.

Pozrikidis, C. & Hill, A. I. (2011) Surfactant-induced instability of a sheared liquid layer. *IMA J. Appl. Math.*, **76**, 859–875.

Rasenat, S., Busse, F. H. & Rehberg, I. (1989) A theoretical and experimental study of double-layer convection. *J. Fluid Mech.*, **199**, 519–540.

Reichenbach, J. & Linde, H. (1981) Linear perturbation analysis of surface-tension-driven convection at a plane interface (Marangoni instability). *J. Coll. Interface Sci.*, **84**, 433–443.

Renardy, Y. (1987) The thin-layer effect and interfacial stability in a two-layer Couette flow with similar liquids. *Phys. Fluids*, **30**, 1627–1637.

Rickett, L. (2013) *A Mathematical Analysis of Digestive Processes in a Model Stomach*. PhD thesis, University of East Anglia.

Sahu, K. C., Ding, H., Valluri, P. & Matar, O. K. (2009a) Linear stability analysis and numerical simulation of miscible two-layer channel flow. *Phys. Fluids*, **21**, 042104, 1–18.

Sahu, K. C., Ding, H., Valluri, P. & Matar, O. K. (2009b) Pressure-driven miscible two-fluid channel flow with density gradients. *Phys. Fluids*, **21**, 043603, 1–10.

Schmid, P. J. & Henningson, D. S. (2001) *Stability and Transition in Shear Flows*. Springer Verlag, New York.

Seyranian, A. P., Kirillov, O. N. & Mailybaev, A. A. (2005) Coupling of eigenvalues of complex matrices at diabolic and exceptional points. *J. Phys. A.: Math. Grn.*, **38**, 1723–1740.

Slavtchev, S., Hennenberg, M., Legros, J.-C. & Lebon, G. (1998) Stationary solutal Marangoni instability in a two-layer system. *J. Coll. Interface Sci.*, **203**, 354–368.

Slavtchev, S., Kalitzova-Kurteva, P. & Mendes, M. A. (2006) Marangoni instability of liquid-liquid systems with a surface-active solute. *Coll. Surfaces A: Physiochem. Eng. Aspects*, **282-283**, 37–49.

Talon, L. & Meiburg, E. (2011) Plane Poiseuille flow of miscible layers with different viscosities: instabilities in the Stokes flow regime. *J. Fluid Mech.*, **686**, 484–506.

Tavener, S. J. & Cliffe, K. A. (2002) Two-fluid Marangoni-Bénard convection with a deformable interface. *J. Comp. Phys.*, **182**, 277–300.

Thiffeault, J.-L., Gouillart, E. & Dauchot, O. (2011) Moving walls accelerate mixing. *Phys. Rev. E*, **84**, 036313.

Yecko, P. (2008) Disturbance growth in two-fluid channel flow: the role of capillarity. *Int. J. Multiphase Flow*, **34**, 272–282.

Yih, C.-S. (1967) Instability due to viscosity stratification. *J. Fluid Mech.*, **27**, 337–352.

Zeren, R. W. & Reynolds, W. C. (1972) Thermal instabilities in two-fluid horizontal layers. *J. Fluid Mech.*, **53**, 305–327.

Zhao, A. X., Wagner, C., Narayanan, R. & Friedrich, R. (1995) Bilayer Rayleigh-Marangoni convection: transitions in flow structures at the interface. *Proc. Roy. Soc. Lond. A*, **451**, 487–502.

List of Figures

List of Tables

IMA Journal of Applied Mathematics (2015) Page 1 of 40
doi:10.1093/imamat/dri017

Incipient mixing by Marangoni effects in slow viscous flow of two immiscible fluid layers

LYDIA RICKETT[1,3], ROBERT PENFOLD[2], MARK G. BLYTH[1], RICHARD PURVIS[1],
MARK J. COOKER[1]

[1] *School of Mathematics, University of East Anglia, Norwich NR4 7TJ, UK.*

[2] *Institute of Food Research, Norwich Research Park, Norwich NR4 7UA, UK.*

[3] *The Sainsbury Laboratory, Norwich Research Park, Norwich NR4 7UH, UK.*

[Received on March 18, 2015]

[Received on 18 March 2015]

Ignoring inertia, a deformable interface separating two fluid films is considered, subject to nonuniform tension driven by the solutal Marangoni effect in the presence of a scalar concentration field. Detailed description of adsorption kinetics is abrogated by a simple ansatz directly relating interfacial tension and bulk solute concentration. Consequently, the formal mathematical treatment and some of the results share features in common with the Rayleigh–Bénard–Marangoni thermocapillary problem. Normal mode perturbation analysis in the limit of small interface deformations establishes the existence of unstable response for low wavenumber excitation. In the classification of Cross and Hohenberg (1993, Rev. Mod. Phys., **65**, 851–1112), both Type-I and Type-II behaviour are observed. By considering the zero wavenumber situation exactly, it is proved that all eigenvalues are purely imaginary with non-positive imaginary part; hence, a Type-III instability is not possible. For characteristic timescales of mass diffusion much shorter than the relaxation time of interfacial fluctuations (infinite crispation number): the response growth rate is obtained explicitly; only a single excitation mode is available and a complete stability diagram is constructed in terms of the relevant control parameters. Otherwise, from a quiescent base state, an infinite discrete spectrum of modes is observed that exhibit avoided crossing and switching phenomena, as well as exceptional points where stationary state pairs coalescence into a single oscillatory standing wave pattern. A base state plane Poiseuille flow, driven by an external pressure gradient, generally exaggerates the response: growth rates of instabilities are enhanced and stable decay is further suppressed with increasing base flow speed; but the inherent symmetry breaking destroys stationary and standing wave response. Results are obtained in this most general situation by implementing a numerical Chebyshev collocation scheme. The model was motivated by hydrodynamic processes supposed to be involved in gastric digestion of humans.

Keywords: liquid-liquid interface, Gibbs elasticity, Stokes flow, linear stability analysis, generalised eigenvalue problem, collocation method, avoided crossing, exceptional point

1. Introduction

To understand the bioavailability and delivery of nutrients and medicines from processed foods and pharmaceutical preparations, a detailed mechanistic model of digestion is needed. The human gastrointestinal tract, from the mouth to the anus, is a coupled sequence of specialized organs, each of which has a distinctive digestive function. In particular, the stomach performs biochemical tasks involving complex salts, strong mineral acid and proteolytic enzymes to produce chyme (soft solid, partially digested food) (Kong & Singh, 2008). The stomach also offers a prominent line of defense against pathogenic microorganisms, but more importantly it is the primary site of mechanical action where ingested material is subjected to a complicated unsteady shear flow, dominated by frictional dissipation rates with relatively negligible inertial forces (Pal et al., 2007). For the purpose of developing a simple mathematical model of this action, we shall adopt here the following working definition: “digestion” means the incipient mixing associated with the linear temporal instability of the interface between two immiscible liquids. Agitated away from equilibrium, the morphological evolution of interfacial patterns and the dynamics of viscous interfacial flow are driven by the physical mechanisms of heterogeneous mixing (Pozrikidis, 1997). Despite the absence of inertia-driven turbulence, a combination of chaotic advection and diffusion can promote mixing in Stokes flows (Thiffeault et al., 2011) that are governed by time-reversible equations of motion. With deformable boundaries, a “geometric” mixing mechanism has also been suggested exploiting anholonomy of the system so that flow variables do not recover their original values on negotiating a closed loop in the parameter space (Cartwright et al., 2012).

Developed at the Institute of Food Research (UK), the Dynamic Gastric Model (DGM) is an in-vitro system that automatically simulates human digestion for the first time from a realistic physiological perspective by accounting for the physical, mechanical and biochemical environment experienced in the stomach (Mercuri et al., 2011; Chessa et al., 2014). To establish a reliable predictive relationship between DGM output and physiological stomach behaviour, some quantitative analysis of the device function is required. Motivated by this need, the present work establishes conditions relevant to the hydrodynamics of digestion insofar as they may lead to mixing and may be a precursor for turbulence.

The application of Orr-Sommerfeld perturbation analysis (Drazin, 2002; Charru, 2011) for parallel fluid flows has a rich, mature and growing literature. Linear response theory leads to a generalised eigenvalue problem, which has a nontrivial solution only if the temporal and spatial frequencies are linked by a dispersion relation. In the most general problem, the large number of control parameters (at least six) spawns a host of potentially unstable modes governed by diverse mechanisms of different physical origin. The viscosity-induced interfacial mode instability of two superposed and bounded fluid layers was first discussed by Yih (1967). Subsequently designated as “the thin-layer effect” (Hooper, 1985), a spatially confined film of more viscous fluid is unstable to long waves at all positive Reynolds numbers. For the converse situation of a confined film of lower viscosity, the flow is stable in the limit of weak interfacial tension (Renardy, 1987a). The thin-layer effect is also observed for multiple fluid layer configurations in plane Poiseuille flow (Anturkar et al., 1990). Neglecting interfacial tension entirely, Charru & Hinch (2000) have neatly rationalised Yih’s small wavenumber analysis together with a second instability at low Reynolds number and high frequency (Hooper & Boyd, 1983) that is present between two shearing unbounded fluids. This latter phenomenon has been confirmed by numerical volume-of-fluid studies in the nonlinear regime (Coward et al., 1997; Li & Renardy, 2000) and might be regarded as a viscous analogue of the Kelvin-Helmholtz instability. Hinch (1984) proposed a detailed mechanism and concluded that some small inertial contribution is necessary in order that advection by the main shear flow can drive the disturbance vorticities in each fluid out-of-phase and so allow the induced velocity fields to amplify the interfacial perturbation. By considering the energy budget in low Reynolds number expansions, Albert & Charru (2000) have confirmed that interfacial instability arises from inertia influencing disturbances, at both small and large wavenumber.

It is perhaps because of this conclusion that the stability of superposed liquid layers in strict Stokes flow (at zero Reynolds number) has received far less attention. Pozrikidis (1997) has implemented a boundary integral method to investigate the interfacial behaviour subject to *finite* amplitude perturbations. He showed that sufficiently large amplitude disturbances cause permanent interfacial deformation with a morphology that depends sensitively on the viscosity ratio. In a very recent study of Poiseuille flow of layered *miscible* fluids in the Stokes regime, Talon & Meiburg (2011) have reported that diffusion has a destabilising effect very similar to that induced by inertia at finite Reynolds number. Instead of a macroscopically sharp discontinuity in fluid properties, partial bulk miscibility influences stability by smearing the interface over a finite width (Anderson et al., 1998). This diffuse and inhomogeneous transition zone is typically modelled (Sahu et al., 2009a,b) by a smooth viscosity distribution coupled to a convective-diffusion equation for a scalar concentration field of "friction inducing solute". Formally, this is very similar to our present treatment of Marangoni effects (Johnson & Narayanan, 1997) where spatial variations of interfacial tension are produced, for example, by a temperature field or by a nonuniform distribution of surfactants. This artifice will simplify the differential geometry and obviate a detailed chemical kinetic mechanism of the interfacial adsorption process (Palmer & Berg, 1972; Reichenbach & Linde, 1981; Slavtchev et al., 1998, 2006) that is highly complicated in typical applications, notably the digestion mechanism of the stomach.

In consequence too, we note a formal correspondence between this approach and the analysis of thermal Marangoni effects (Nepomnyashchy et al., 2006). As a rich example of spontaneous pattern formation in nonequilibrium dynamical systems, the classical Rayleigh–Bénard convective instability (Koschmieder, 1974) of a single fluid layer subject to a transverse temperature gradient has been long studied (Normand et al., 1977) but continues to attract attention (Bodenschatz et al., 2000). For a stratified superposition of several immiscible fluids, many new and qualitatively different phenomena arise from the competition of individual layer instabilities (Andereck et al., 1998). By assuming "exchange of stabilities" (Drazin & Reid, 2004), a linear stability analysis of the thermal Marangoni effect was tackled by Zeren & Reynolds (1972), and subsequently extended by Zhao et al. (1995) to account for interfacial deformation. Rasenat et al. (1989) completed a more general treatment to demonstrate that steady convection could be driven either by buoyancy or by Marangoni forces. For thin film flows the mathematical analysis exploits disparity in length scales to simplify the field equations, but microscopic surface forces of van der Waals or electromagnetic origin can also become asymptotically important (Oron et al., 1997; Craster & Matar, 2009). The nonlinear evolution of interfacial deformation arising from a small wavenumber perturbation (the "long-wave" limit) is governed by a Cahn-Hilliard equation that describes the ("phase") transition between monotonic and stationary instabilities, in analogy with thermodynamic spinodal decomposition (Merkt et al., 2005; Nepomnyashchy et al., 2006).

Frenkel and Halpern (Frenkel & Halpern, 2002; Halpern & Frenkel, 2003) have identified a new non-inertial interfacial instability, which was investigated further by Blyth & Pozrikidis (2004a). This is driven by the Marangoni traction that arises from the presence of adsorbed surfactant and velocity shear in two-layer planar flows of Couette-Poiseuille type. A physical mechanism is also proposed where the imbalance of interfacial tension drives flow from troughs to peaks and reinforces the deformation. Notably, in contrast to the interfacial mode of inertial flows, a viscosity jump is not required for instability. Moreover, explicit analytic expressions are obtained for the wave speed and growth rate. Corresponding phenomena are also predicted for surfactant-laden interfaces in gravity driven flow on an inclined plane (Gao & Lu, 2007; Blyth & Pozrikidis, 2004b) and for radially stratified films in concentric two-fluid Taylor–Couette flow (Peng & Zhu, 2010), where there is a complicated interaction of instability mechanisms. The effect of inertia coupled with the Marangoni instability has also been studied by normal-mode analysis (Frenkel & Halpern, 2005; Blyth & Pozrikidis, 2004c) and numerical methods (Pozrikidis, 2004) applicable beyond the linear regime. A wider range of unstable wavenumbers is the chief consequence. After observing that linear analysis of Stokes flow has established insoluble surfactant is unable to destabilise a sheared interface between two semi-infinite fluids, Pozrikidis & Hill (2011) have recently questioned the necessity of a bounded fluid domain to realise the Marangoni instability. They concluded that one wall is required to engage the Marangoni mechanism, but the presence

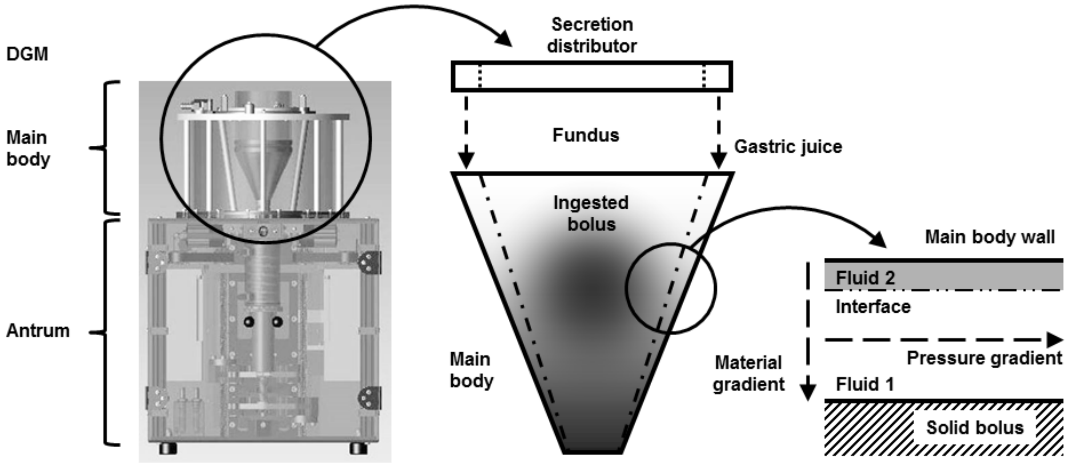

FIG. 1. Cartoon illustrating the modelling abstraction from the physical DGM device to the mathematical idealisation.

of a second wall may stabilise the flow.

Section 2 sets out the physical arguments to establish the appropriate governing equations and boundary conditions. A full mathematical treatment is developed in Section 3, culminating in a dispersion relation. Two special cases are considered in Section 4 before the general solution is presented in Section 5. Results are collected and discussed in Section 6, and the paper concludes in Section 7 with some perspective on applications and future work. Section 9 is an appendix containing comprehensive mathematical details and formal proofs of some results in the text.

2. Mathematical model specification

2.1 *Physical situation: the Dynamic Gastric Model (DGM)*

With its modular design, the DGM separates two primary anatomical features of the human stomach: the proximal cardia/fundus/main-body that receives material from the oesophagus, and the distal pyloric antrum where chyme is produced before discharge to the duodenum (Wickham et al., 2012). The pseudo-main body comprises a thermally jacketted elastic cone, hydraulically driven by cyclic pumping to generate a specific inhomogeneous mixing behaviour and hydration patterns that closely resemble observations in-vivo (Marciani et al., 2001, 2006, 2009). A computer controlled feed-back loop monitors temperature and pH in real time to govern the injection of surfactants, acids/bases and proteolytic solutions that correspond to gastric secretions. An intervening valve regulates residence times before partial emptying into a pseudo-antrum where digesta are subjected to periodic high shear fields that force mechanical breakdown of the food structure.

In operation (Wickham et al., 2012), aqueous gastric solution enters the DGM fundus under gravity from an annular distributor, suspended coaxially above the main body, and flows in a thin film down the interior surface of the conical vessel (Figure 1). The main body is then charged with “ingested” material, typically a heterogeneous viscoelastic food product, but most simply with a Newtonian liquid. Gentle deformations of the elastic main body wall are actuated by driven pressure variation of the external thermal bath. The observed digestion process has the character of “onion peeling” where thin layers of ingested material are progressively sloughed off to enter the lower antral chamber. The DGM main body has geometric and material features in common with the intensively studied core-annular pipe flow (Renardy, 1987b; Joseph et al., 1997) used for the efficient water lubricated transport of heavy crude oils, emulsions or bitumen froths, but differs in the steeply converging tube arrangement with weakly deformable walls and a much lower flow rate.

To simplify the problem, a general non-Newtonian food material of spatially inhomogeneous transport properties is idealised as a discrete ternary mixture of uniform macroscopic phases. Further, the main food bolus is regarded as effectively solid and suspended at neutral buoyancy in the main body device. We assume the “onion-peeling” process is confined to a relatively thin sleeve of liquid material that separates the bolus from the main body wall where most gastric chemistry takes place. This sleeve is treated as a uniform slab confining two immisicible liquids that are possibly subject to a constant longitudinal pressure gradient. Finally, a scalar material field is imposed that interacts with the tension of the interface to represent the biological activity of gastric secretions including acids, enzymes and surfactants. The solid food bolus and the main body wall are supposed porous to the solute material. Although the DGM main body wall is actually impermeable, this last assumption is more realistic in terms of the physiological organ and symmetrises the solute boundary conditions in our analysis. These modelling abstractions are illustrated by the cartoon in Figure 1.

2.2 *Coordinate frame, constitutive relation and nondimensionalisation*

Under isothermal conditions, consider the unidirectional creeping flow of two incompressible Newtonian fluids (indexed by the labels $j = 1,\ 2$), driven by a constant axial pressure gradient $-\tilde{G}_p$ (with $\tilde{G}_p \geqslant 0$) through an infinite channel bounded by stationary parallel walls fixed at separation $2\tilde{h}$ (see Figure 2). It is natural to adopt a Cartesian system $(\tilde{x},\ \tilde{y},\ \tilde{z})$ with the longitudinal coordinate $-\infty < \tilde{x} < \infty$ and the transverse coordinate $-\tilde{h} \leqslant \tilde{y} \leqslant \tilde{h}$. Unit vectors in each coordinate direction are denoted $\mathbf{i}$, $\mathbf{j}$ and $\mathbf{k}$, respectively. Interfacial disturbances are supposed small and are manifest in two spatial dimensions only, so that all the relevant dynamical quantities are independent of the lateral coordinate $\tilde{z}$. The fluid labelled 1 is confined between the lower wall at $\tilde{y} = -\tilde{h}$ and the interface, whose flat equilibrium position is $\tilde{y} = \tilde{\alpha}$ where $\tilde{\alpha}$ is a constant (see Figure 2). Each of the bulk fluids is characterised by a dynamic viscosity $\tilde{\mu}_j$ and a diffusion coefficient $\tilde{D}_j$ for solute species. We observe the Boussinesq approximation and suppose that all $\tilde{\mu}_j$ and $\tilde{D}_j$ are constant and remain unaffected by variations in bulk solute concentration. Furthermore, there is no stratification in mass density $\tilde{\rho}_1 = \tilde{\rho}_2 = \tilde{\rho}$ and the system is assumed free of external body forces, so buoyancy effects are neglected.

The deformable interface located at $\tilde{y} = \tilde{\eta}\left(\tilde{x},\ \tilde{t}\right)$, is a free material boundary with a Newtonian response: explicit effects of interfacial rheology are neglected. Nevertheless, the associated equilibrium interfacial tension is a sensitive function of the local environment, with a complicated dependence on temperature and the presence of solutes in either of the adjoining fluid phases. Spatial inhomogeneities of the interfacial tension can arise from fluctuations in the physical adsorption of surfactants and advective interfacial transport, or from localised chemical activity at the interface. For simplicity, we posit a scalar field $\tilde{\chi}_j = \tilde{\chi}_j\left(\tilde{x},\ \tilde{y},\ \tilde{t}\right)$ to represent the concentration of some surface active species dissolved in fluid j, that is subject to advection and diffusion in the three-dimensional bulk phases only. It is here that our ansatz deviates from other studies of the solutal Marangoni effect (Li & Pozrikidis,

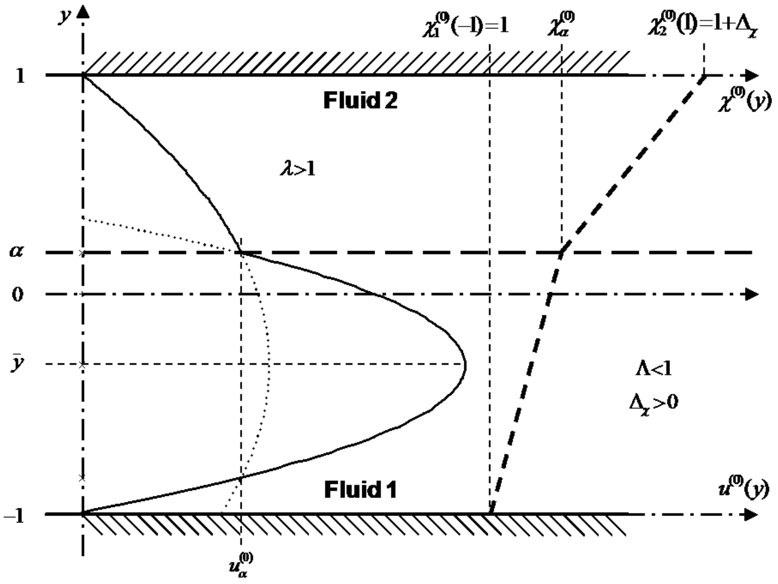

FIG. 2. The basic states of fluid flow and concentration distribution are shown with the geometry and coordinate variables defined in the text.

1997; Frenkel & Halpern, 2002; Halpern & Frenkel, 2003; Frenkel & Halpern, 2005; Blyth & Pozrikidis, 2004a; Pozrikidis, 2004; Blyth & Pozrikidis, 2004c; Gao & Lu, 2007; Pozrikidis & Hill, 2011) where the surfactant is assumed insoluble in bulk, confined strictly to the interface and governed by an appropriate two-dimensional transport equation. In accord with our DGM idealisation, Dirichlet conditions are prescribed on $\tilde{\chi}_j$ at the bounding walls which, although stationary, support a diffusive flux of solute material to adjacent "notional" phases. Thus, under the influence of a concentration gradient, the solute is allowed to spread by Brownian motion but without advection into the food bolus and the gastric mucosa that confine the fluid slab: the static walls are porous to solute but impermeable to solvent.

We undertake a temporal linear stability analysis of steady base state flow with a uniform interfacial tension and concentration fields

$$\tilde{\chi}_j^{(0)} = \tilde{\chi}_j^{(0)}\left(\tilde{y}\right) \ , \ \ j \in \{1,\, 2\} \ , \tag{2.1}$$

that depend only on the transverse coordinate across the channel. For small perturbations of the base state flow, the change in the interfacial tension is proportional to the induced departure of the bulk concentration from $\tilde{\chi}_j^{(0)}$, and proportional to a contribution that arises from displacement of the interface within the static field. We adopt the linear interfacial equation of state

$$\tilde{\gamma} = \tilde{\gamma}\left(\tilde{x},\, \tilde{y},\, \tilde{t}\right) = \tilde{\gamma}_0 \left(1 - \mathrm{Mg} \times \left(\frac{\tilde{\chi}_j\left(\tilde{x},\, \tilde{y},\, \tilde{t}\right) - \tilde{\chi}_j^{(0)}\left(\tilde{\alpha}\right)}{\tilde{\chi}_2^{(0)}\left(\tilde{h}\right) - \tilde{\chi}_1^{(0)}\left(-\tilde{h}\right)}\right)\right) \ , \tag{2.2}$$

with the understanding that physical meaning is attached to this field $\tilde{\gamma}$ only for $\tilde{y} = \tilde{\eta}$. The dimensionless interaction parameter Mg measures the change in interfacial tension with respect to the local

Mg	$=$	$\dfrac{\tilde{\chi}_2^{(0)}(\tilde{h}) - \tilde{\chi}_1^{(0)}(-\tilde{h})}{\tilde{\gamma}_0}\left(\dfrac{\partial\tilde{\gamma}}{\partial\tilde{\chi}_j}\right)$	Dilatational elasticity of interface
Cr	$=$	$\dfrac{\tilde{\mu}_1\tilde{D}_1}{\tilde{h}\tilde{\gamma}_0}$	Crispation number
Eu	$=$	$\dfrac{\tilde{h}^2\tilde{G}_p}{\tilde{\gamma}_0}$	Euler number
Δ_χ	$=$	$\dfrac{\tilde{h}\tilde{\gamma}_0}{\tilde{\mu}_1^2}\left(\tilde{\chi}_2^{(0)}(\tilde{h}) - \tilde{\chi}_1^{(0)}(-\tilde{h})\right)$	Overall solute concentration difference
λ	$=$	$\dfrac{\tilde{\mu}_2}{\tilde{\mu}_1}$	Dynamic viscosity ratio
Λ	$=$	$\dfrac{\tilde{D}_2}{\tilde{D}_1}$	Solute diffusivity ratio
δ	$=$	$\dfrac{1-\tilde{\alpha}/\tilde{h}}{1+\tilde{\alpha}/\tilde{h}}$	Fluid film thickness ratio

Table 1. The seven dimensionless control parameters that feature in this analysis.

concentration of surface active solutes and is related to the dilatational (Gibbs) elasticity that couples the dynamic boundary conditions on interfacial stress and surfactant flux (Edwards et al., 1991). Typically $\mathrm{Mg} > 0$ and the spontaneous physical adsorption of material at the interface will lower the surface free energy relative to the bulk phases. We are also interested, however, in the more complex situation where changes of interfacial tension are driven by chemical activity. For example, denaturation, cross-linking or gelation of proteins at the interface may lead to *increases* of tension compared with the bare surface. Within the ansatz (2.2), this behaviour could be modelled by choosing $\mathrm{Mg} < 0$, that is the solutal analogue of the anomalous thermocapillary effect (Braverman et al., 2000).

To accommodate the analysis of a quiescent base state with a vanishing pressure gradient $\tilde{G}_p = 0$, suitable units of mass, length and time are

$$[\tilde{M}] = \frac{(\tilde{h}\tilde{\mu}_1)^2}{\tilde{\gamma}_0} \ , \ [\tilde{L}] = \tilde{h} \ , \ [\tilde{T}] = \frac{\tilde{h}\tilde{\mu}_1}{\tilde{\gamma}_0} \ . \tag{2.3}$$

Accordingly, the dynamics depends on at most seven dimensionless control parameters listed in Table 1. From now on, all dimensionless quantities will be indicated by the absence of tilde decoration.

2.3 *Governing equations*

In the effective two-dimensional geometry, we have the Stokes stream functions $\psi_j = \psi_j(x,\ y,\ t)$ satisfying biharmonic equations

$$\nabla^4\psi_j = \left(\frac{\partial^4}{\partial x^4} + 2\frac{\partial^4}{\partial x^2\partial y^2} + \frac{\partial^4}{\partial y^4}\right)\psi_j = 0 \ , \tag{2.4}$$

that determine the velocity fields $\mathbf{u}_j = u_j\mathbf{i} + v_j\mathbf{j}$ with longitudinal and transverse components

$$u_j = \frac{\partial\psi_j}{\partial y} \quad \text{and} \quad v_j = -\frac{\partial\psi_j}{\partial x} \ . \tag{2.5}$$

Incorporating the pressure fields $p_j = p_j(x,\ y,\ t)$, the Newtonian stress tensors are

$$\boldsymbol{\sigma}_j = \boldsymbol{\sigma}_j(x,\ y,\ t) = -p_j\mathbf{I} + \lambda_j\left(\nabla\mathbf{u}_j + \left(\nabla\mathbf{u}_j\right)^T\right)\ , \tag{2.6}$$

where $\lambda_1 = 1$ and $\lambda_2 = \lambda$. The concentration fields are subject to fluid advection and bulk diffusion, described as

$$\left(\frac{\partial}{\partial t} + \mathbf{u}_j\cdot\nabla - \mathrm{Cr}\,\Lambda_j\nabla^2\right)\chi_j = 0\ , \tag{2.7}$$

where $\Lambda_1 = 1$ and $\Lambda_2 = \Lambda$.

With the interface position at $y = \eta(x,\ t)$, the field equations (2.4) and (2.7) are supplemented by no-slip and kinematic boundary conditions:

$$\begin{array}{ll}
u_1(x,\ -1,\ t) = 0\ ,\ \ u_2(x,\ 1,\ t) = 0\ , & \left(\text{no slip on walls}\right) \\[2ex]
v_1(x,\ -1,\ t) = 0\ ,\ \ v_2(x,\ 1,\ t) = 0\ , & \left(\begin{array}{c}\text{stationary, solvent}\\ \text{impermeable walls}\end{array}\right) \\[2ex]
\left.\begin{array}{l}(u_1 - u_2)(x,\ \eta,\ t) = 0 \\ (v_1 - v_2)(x,\ \eta,\ t) = 0\end{array}\right\}\ , & \left(\begin{array}{c}\text{flow continuity}\\ \text{on interface}\end{array}\right) \\[2ex]
\dfrac{\partial\eta}{\partial t} + u_j(x,\ \eta,\ t)\dfrac{\partial\eta}{\partial x} - v_j(x,\ \eta,\ t) = 0\ . & \left(\begin{array}{c}\text{moving material}\\ \text{interface}\end{array}\right)
\end{array} \tag{2.8}$$

Given local orthogonal unit vectors perpendicular $\hat{\mathbf{n}} = \hat{\mathbf{n}}(x,\ \eta,\ t)$ (directed from fluid 2 into fluid 1) and tangent $\hat{\mathbf{t}} = \hat{\mathbf{t}}(x,\ \eta,\ t)$ to the interface, the corresponding components of the dynamic stress balances become, respectively:

$$\begin{aligned}
\hat{\mathbf{n}}\cdot\Big((\boldsymbol{\sigma}_1 - \boldsymbol{\sigma}_2)(x,\ \eta,\ t)\Big)\cdot\hat{\mathbf{n}} &= \left(1 + \left(\frac{\partial\eta}{\partial x}\right)^2\right)^{-3/2}\frac{\partial^2\eta}{\partial x^2}\ \gamma(x,\ \eta,\ t)\ , \\
\hat{\mathbf{t}}\cdot\Big((\boldsymbol{\sigma}_1 - \boldsymbol{\sigma}_2)(x,\ \eta,\ t)\Big)\cdot\hat{\mathbf{n}} &= -\left(1 + \left(\frac{\partial\eta}{\partial x}\right)^2\right)^{-1/2}\left(\frac{\partial\gamma}{\partial x}(x,\ \eta,\ t) + \frac{\partial\eta}{\partial x}\frac{\partial\gamma}{\partial y}(x,\ \eta,\ t)\right)\ .
\end{aligned} \tag{2.9}$$

Finally, concentrations are prescribed on the walls, together with interfacial continuity conditions on the χ_j and the material flux according to:

$$\begin{array}{ll}
\left.\begin{array}{l}\chi_1(x,\ -1,\ t) = 1 \\ \chi_2(x,\ 1,\ t) = 1 + \Delta_\chi\end{array}\right\}\ , & \left(\begin{array}{c}\text{prescribed wall}\\ \text{concentration}\end{array}\right) \\[2ex]
(\chi_1 - \chi_2)(x,\ \eta,\ t) = 0\ , & \left(\begin{array}{c}\text{concentration continuity}\\ \text{on interface}\end{array}\right) \\[2ex]
\dfrac{\partial}{\partial y}(\chi_1 - \Lambda\chi_2)(x,\ \eta,\ t) = 0\ . & \left(\begin{array}{c}\text{concentration flux}\\ \text{continuity on interface}\end{array}\right)
\end{array} \tag{2.10}$$

3. General analysis of the mathematical model

3.1 *Base (ground) state: unperturbed flow*

For steady plane Poiseuille flow with a flat interface $\eta(x) = \alpha$, we obtain the pressure fields

$$p_j^{(0)} = p_j^{(0)}(x) = p_0 - \mathrm{Eu}\, x \ , \tag{3.1}$$

where p_0 is a constant background pressure and Eu is the Euler number (Table 1). Similarly, the velocity fields are (see Figure 2)

$$\begin{aligned} u_1^{(0)}(y) &= u_\alpha^{(0)} + \frac{\mathrm{Eu}}{2}(\alpha - y)\left(y - \frac{\delta-\lambda}{\delta+\lambda}\right) = \frac{\partial \psi_1^{(0)}}{\partial y} \ , \quad v_1^{(0)} = 0 \ , \quad (-1 \leqslant y \leqslant \alpha) \ , \\ u_2^{(0)}(y) &= u_\alpha^{(0)} - \frac{\mathrm{Eu}}{2\lambda}(y - \alpha)\left(y - \frac{\delta-\lambda}{\delta+\lambda}\right) = \frac{\partial \psi_2^{(0)}}{\partial y} \ , \quad v_2^{(0)} = 0 \ , \quad (\alpha \leqslant y \leqslant 1) \ , \end{aligned} \tag{3.2}$$

where the horizontal velocity at the interface is

$$u_\alpha^{(0)} = \frac{2\delta\,\mathrm{Eu}}{(1+\delta)(\delta+\lambda)} \ . \tag{3.3}$$

The steady concentration fields are (see Figure 2)

$$\begin{aligned} \chi_1^{(0)}(y) &= \chi_\alpha^{(0)} - G_{\chi,1}(\alpha - y) \ , \quad (-1 \leqslant y \leqslant \alpha) \ , \\ \chi_2^{(0)}(y) &= \chi_\alpha^{(0)} + G_{\chi,2}(y - \alpha) \ , \quad (\alpha \leqslant y \leqslant 1) \ , \end{aligned} \tag{3.4}$$

where the unperturbed interfacial concentration and corresponding gradients are

$$\chi_\alpha^{(0)} = \frac{\delta + \Lambda\left(1+\Delta_\chi\right)}{\delta+\Lambda} \ , \qquad G_{\chi,1} = \frac{\Lambda(1+\delta)\Delta_\chi}{2(\delta+\Lambda)} \ , \qquad G_{\chi,2} = \frac{(1+\delta)\Delta_\chi}{2(\delta+\Lambda)} = \frac{G_{\chi,1}}{\Lambda} \ . \tag{3.5}$$

3.2 *Perturbed interface*

We introduce a plane wave perturbation of the interface

$$y = \eta(x,\, t) = \alpha + \varepsilon\Re\big(\mathscr{A}\exp\big(i(kx - \omega t)\big)\big) \ , \tag{3.6}$$

with a prescribed real and positive wavenumber k. Here, $\Re$ denotes the real part. The real order parameter $\varepsilon > 0$ is assumed small so we seek the linear response to the wave disturbance with amplitude $\mathscr{A} = O(1)$. Evolution of the disturbance in time is governed by the imaginary part $\Im(\omega)$ of the generally complex temporal frequency ω. A stable response decays towards zero $\big(\Im(\omega) < 0\big)$ while unbounded growth $\big(\Im(\omega) > 0\big)$ characterises an instability. All other dynamical variables $\Theta \in \big\{\psi_j,\, u_j,\, v_j,\, p_j,\, \chi_j\big\}$ are supposed to develop similar fluctuations so that

$$\Theta = \Theta(x,\, y,\, t) = \Theta^{(0)}(y) + \varepsilon\Re\big(\Theta^{(1)}(y)\exp\big(i(kx - \omega t)\big)\big) \ . \tag{3.7}$$

To simplify notation, we identify $\mathscr{D} \equiv \mathrm{d}/\mathrm{d}y$ with the differential operator and further adopt the following definitions:

$$k_- \equiv k(1-\alpha) = \frac{2k\delta}{1+\delta} \ , \quad k_+ \equiv k(1+\alpha) = \frac{2k}{1+\delta} \ ,$$

$$c_\xi \equiv \cosh(k\xi) \ , \ \ s_\xi \equiv \sinh(k\xi) \ , \tag{3.8}$$

where ξ is a dummy variable.

By virtue of the linear field equations (2.4), the stream function perturbations each satisfy

$$\left(\mathscr{D}^2 - k^2\right)^2 \psi_j^{(1)} = 0 \ , \tag{3.9}$$

with general solutions of the form

$$\psi_j^{(1)} = \left(\hat{A}_j + \hat{C}_j y\right) c_y + \left(\hat{B}_j + \hat{D}_j y\right) s_y \ , \tag{3.10}$$

where $\hat{A}_j$, $\hat{B}_j$, $\hat{C}_j$ and $\hat{D}_j$ are constants to be determined. The linear advection-diffusion law (2.7) yields

$$\left(\mathscr{D}^2 - \left(k^2 + \frac{i}{\mathrm{Cr}\,\Lambda_j}\left(ku_j^{(0)} - \omega\right)\right)\right)\chi_j^{(1)} + \frac{ikG_{\chi,j}}{\mathrm{Cr}\,\Lambda_j}\,\psi_j^{(1)} = 0 \ . \tag{3.11}$$

With constants $\hat{F}_j$ and $\hat{G}_j$, the general solutions

$$\chi_j^{(1)} = \chi_j^{(1)}(y;\ \omega) = \frac{2\Delta_\chi}{\mathrm{Mg}}\left(\left(\hat{F}_j\Psi_j + \hat{G}_j\Phi_j\right) - ik\,I_j\right) \ , \tag{3.12}$$

each comprise a complementary function of the independent homogeneous solutions $\Psi_j = \Psi_j(y)$ and $\Phi_j = \Phi_j(y)$, together with a particular integral $I_j = I_j\left(y;\ \left[\psi_j^{(1)}\right]\right)$. In this general formulation, the Ψ_j and Φ_j are unknown but will be determined explicitly for various cases discussed in Section 4. The I_j are obtained by the variation of parameters method and depend functionally on the flow perturbation:

$$\begin{aligned} I_j &= \hat{A}_j\mathscr{I}_j\left(y;\ \left[c_y\right]\right) + \hat{B}_j\mathscr{I}_j\left(y;\ \left[s_y\right]\right) + \hat{C}_j\mathscr{I}_j\left(y;\ \left[yc_y\right]\right) + \hat{D}_j\mathscr{I}_j\left(y;\ \left[ys_y\right]\right) \ , \\ \mathscr{I}_j\left(y;\ \left[\Xi\right]\right) &= \frac{\mathrm{Mg}}{\mathrm{Cr}}\left(\frac{G_{\chi,j}}{2\Delta_\chi\Lambda_j}\right)\int^y \Xi(\xi)\left(\frac{\Psi_j(\xi)\Phi_j(y) - \Psi_j(y)\Phi_j(\xi)}{\mathscr{W}\left(\Psi_j(\xi),\ \Phi_j(\xi)\right)}\right)\mathrm{d}\xi \ , \end{aligned} \tag{3.13}$$

in which

$$\mathscr{W}\left(\Theta_1(\xi_1),\ \Theta_2(\xi_2)\right) = \det\begin{pmatrix} \Theta_1(\xi_1) & \mathscr{D}\Theta_1(\xi_2) \\ \Theta_2(\xi_1) & \mathscr{D}\Theta_2(\xi_2) \end{pmatrix} , \tag{3.14}$$

becomes the Wronskian of functions Θ_1 and Θ_2 in case $\xi_1 = \xi_2$. In general, the concentration perturbations $\chi_j^{(1)}$ and the associated quantities in (3.12) will all depend parametrically on the unknown temporal frequency ω.

Substitution of (3.7) into the boundary conditions (2.8), (2.9) and (2.10), followed by linearisation to lowest order in ε obtains:

$$\mathscr{D}\psi_1^{(1)}(-1) = 0 \ , \ \ \mathscr{D}\psi_2^{(1)}(1) = 0 \ , \qquad \left(\text{no slip on walls}\right)$$

$$\psi_1^{(1)}(-1) = 0 \ , \ \ \psi_2^{(1)}(1) = 0 \ , \qquad \left(\begin{array}{c}\text{stationary, solvent}\\ \text{impermeable walls}\end{array}\right)$$

$$\left.\begin{array}{l} \mathscr{D}\left(\psi_1^{(1)} - \psi_2^{(1)}\right)(\alpha) + J_{\mathbf{u}}\mathscr{A} = 0 \\[2ex] \left(\psi_1^{(1)} - \psi_2^{(1)}\right)(\alpha) = 0 \end{array}\right\} , \qquad \left(\begin{array}{c}\text{flow continuity}\\ \text{on interface}\end{array}\right)$$

$$\begin{array}{ll}
k\psi_j^{(1)}(\alpha)+J_\eta\mathscr{A}=0\ , & \left(\begin{matrix}\text{moving material}\\ \text{interface}\end{matrix}\right)\\[2ex]
\mathscr{D}\left(\mathscr{D}^2-3k^2\right)\left(\psi_1^{(1)}-\lambda\,\psi_2^{(1)}\right)(\alpha)-2k^2J_{\perp\boldsymbol{\sigma}}\mathscr{A}=0\ , & \left(\begin{matrix}\text{normal stress}\\ \text{balance on interface}\end{matrix}\right)\\[2ex]
\left(\mathscr{D}^2+k^2\right)\left(\psi_1^{(1)}-\lambda\,\psi_2^{(1)}\right)(\alpha)+2k\left(i\,\mathrm{Mg}\,\dfrac{\chi_2^{(1)}(\alpha)}{2\Delta_\chi}+J_{\parallel\boldsymbol{\sigma}}\mathscr{A}\right)=0\ , & \left(\begin{matrix}\text{tangential stress}\\ \text{balance on interface}\end{matrix}\right)\\[2ex]
\chi_1^{(1)}(-1)=0\ ,\ \ \chi_2^{(1)}(1)=0\ , & \left(\begin{matrix}\text{prescribed wall}\\ \text{concentration}\end{matrix}\right)\\[2ex]
\left(\chi_1^{(1)}-\chi_2^{(1)}\right)(\alpha)+J_\chi\mathscr{A}=0\ , & \left(\begin{matrix}\text{concentration continuity}\\ \text{on interface}\end{matrix}\right)\\[2ex]
\mathscr{D}\left(\chi_1^{(1)}-\Lambda\chi_2^{(1)}\right)(\alpha)=0\ , & \left(\begin{matrix}\text{concentration flux}\\ \text{continuity on interface}\end{matrix}\right)
\end{array}\tag{3.15}$$

where the “jump” terms proportional to the interfacial disturbance amplitude $\mathscr{A}$ are

$$\begin{aligned}
J_{\mathbf{u}}&=\mathscr{D}\left(u_1^{(0)}-u_2^{(0)}\right)(\alpha)=\mathrm{Eu}\,\frac{(1-\lambda)(\lambda-\delta^2)}{\lambda(1+\delta)(\lambda+\delta)}\ ,\\
J_\eta&=ku_\alpha^{(0)}-\omega\ ,\\
J_{\perp\boldsymbol{\sigma}}&=\frac{ik}{2}\ ,\\
J_{\parallel\boldsymbol{\sigma}}&=i\,\mathrm{Mg}\,\frac{G_{\chi,2}}{2\Delta_\chi}=i\,\mathrm{Mg}\,\frac{(1+\delta)}{4(\delta+\Lambda)}\ ,\\
J_\chi&=G_{\chi,1}-G_{\chi,2}=\frac{(1+\delta)(\Lambda-1)\Delta_\chi}{2(\delta+\Lambda)}\ .
\end{aligned}\tag{3.16}$$

The homogeneous linear system (3.15) demands a singular coefficient matrix to deliver non-trivial solutions. Lengthy but straightforward calculation of the determinant leads to the dispersion relation

$$\mathscr{L}_{k,\alpha}(\Lambda)\left(\kappa_{\mathbf{u}}J_{\mathbf{u}}+\kappa_\eta J_\eta+\kappa_{\perp\boldsymbol{\sigma}}J_{\perp\boldsymbol{\sigma}}\right)+\Lambda\mathscr{L}_{k,\alpha}(1)\kappa_{\parallel\boldsymbol{\sigma}}J_{\parallel\boldsymbol{\sigma}}=0\ ,\tag{3.17}$$

where the function $\mathscr{L}_{k,\alpha}$ and the coefficients $\kappa_{\mathbf{u}}$, κ_η and $\kappa_{\perp\boldsymbol{\sigma}}$ all depend parametrically on ω as detailed in the appendix (Section 9.1). The relatively simple coefficient $\kappa_{\parallel\boldsymbol{\sigma}}$ depends only on the wavenumber k and the geometric parameter δ. Further analysis requires solutions of the advection-diffusion equation (2.7) to evaluate the integrals I_j and to determine the functional form of $\mathscr{L}_{k,\alpha}$. As well as the most general case, notable limiting situations are discussed in the following sections.

4. Special cases from the general analysis

4.1 *Case I:* Cr $\to \infty$ *with* $0 < \Lambda < \infty$

For large crispation number and $0 < \Lambda < \infty$, solute diffusion in both films is effectively instantaneous on the time scale of interfacial fluctuations. In this circumstance, the solute transport equation (2.7) then reduces to Laplace's equation and the perturbed concentration fields now satisfy a simple diffusion equation (cf. (3.11))

$$\left(\mathscr{D}^2 - k^2\right)\chi_j^{(1)} = 0 \quad , \tag{4.1}$$

regardless of any base state flow. Solutions of these homogeneous ODEs take the form (3.12) with

$$\Psi_j = c_y \quad \text{and} \quad \Phi_j = s_y \quad , \tag{4.2}$$

independent of ω, and the particular integrals vanish $\left(I_j = 0\right)$. As a consequence, the concentration fields are decoupled from the fluid flows and can be solved independently to yield:

$$\chi_1^{(1)} = -J_\chi \mathscr{A}\, \frac{k\Lambda c_{1-\alpha} s_{1+y}}{\mathscr{L}^{(0)}_{k,\alpha}(\Lambda)} \quad , \qquad \chi_2^{(1)} = J_\chi \mathscr{A}\, \frac{k c_{1+\alpha} s_{1-y}}{\mathscr{L}^{(0)}_{k,\alpha}(\Lambda)} \quad , \tag{4.3}$$

where

$$\mathscr{L}^{(0)}_{k,\alpha}(\Lambda) = k\left(\Lambda c_{1-\alpha} s_{1+\alpha} + c_{1+\alpha} s_{1-\alpha}\right) > 0 \quad , \tag{4.4}$$

and the frequency parameter ω does not enter (see the appendix Section 9.1). In the case of identical mass diffusivities for both films, then $J_\chi = 0$ so that $\chi_1^{(1)} = \chi_2^{(1)} = 0$ and the base state concentration fields $\chi_j^{(0)}$ are maintained everywhere for all time regardless of perturbations to the fluid flows.

A dispersion relation of the form (3.17) is obtained:

$$\kappa_{\mathbf{u}}^{(0)} J_{\mathbf{u}} + \kappa_\eta^{(0)} J_\eta + \kappa_{\perp\boldsymbol{\sigma}}^{(0)} J_{\perp\boldsymbol{\sigma}} + \left(\frac{\Lambda \mathscr{L}^{(0)}_{k,\alpha}(1)}{\mathscr{L}^{(0)}_{k,\alpha}(\Lambda)}\right) \kappa_{\parallel\boldsymbol{\sigma}} J_{\parallel\boldsymbol{\sigma}} = 0 \quad , \tag{4.5}$$

but where the $\kappa^{(0)}$-coefficients are independent of the frequency parameter ω (see the appendix Section 9.1) that now appears only in J_η (see (3.16)). Define the functions

$$g_\xi \equiv \sinh^2(k\xi) - (k\xi)^2 \quad , \qquad \mathscr{D}g_\xi \equiv \sinh(2k\xi) - 2k\xi \quad , \qquad h_\xi \equiv \frac{g_\xi}{\mathscr{D}g_\xi} \quad , \tag{4.6}$$

with a natural extension of our earlier subscript notation (3.8). From (4.5) the disturbance growth rate is

$$\begin{aligned} \Im(\omega) &= \frac{\mathscr{L}^{(0)}_{k,\alpha}(\Lambda)\kappa^{(0)}_{\perp\boldsymbol{\sigma}}\Im\left(J_{\perp\boldsymbol{\sigma}}\right) + \Lambda\mathscr{L}^{(0)}_{k,\alpha}(1)\kappa_{\parallel\boldsymbol{\sigma}}\Im\left(J_{\parallel\boldsymbol{\sigma}}\right)}{\mathscr{L}^{(0)}_{k,\alpha}(\Lambda)\kappa^{(0)}_\eta} \\ &= \frac{kg_{1+\alpha}}{4\kappa_\eta^{(0)}}\left(\mathrm{Mg}\,\mathscr{M}_{k,\alpha}(\Lambda)\left(\lambda\delta^2 - \frac{g_{1-\alpha}}{g_{1+\alpha}}\right) - \mathscr{D}g_{1-\alpha}\left(\lambda + \frac{h_{1-\alpha}}{h_{1+\alpha}}\right)\right) \\ &= \frac{kg_{1-\alpha}}{4\kappa_\eta^{(0)}}\,\lambda\,\left(\mathrm{Mg}\,\mathscr{M}_{k,\alpha}(\Lambda)\delta^2\left(\frac{g_{1+\alpha}}{g_{1-\alpha}} - \frac{1}{\lambda\delta^2}\right) - \mathscr{D}g_{1+\alpha}\left(\frac{1}{\lambda} + \frac{h_{1+\alpha}}{h_{1-\alpha}}\right)\right) \quad , \end{aligned} \tag{4.7}$$

where

$$\mathscr{M}_{k,\alpha}(\Lambda) = \frac{4k\Lambda\mathscr{L}^{(0)}_{k,\alpha}(1)}{(1+\delta)(\delta+\Lambda)\mathscr{L}^{(0)}_{k,\alpha}(\Lambda)} = \frac{2k_+ s_2 \Lambda}{(\delta+\Lambda)\big(c_{1-\alpha}s_{1+\alpha}\Lambda + c_{1+\alpha}s_{1-\alpha}\big)} > 0 \ , \tag{4.8}$$

depends on the excitation wavenumber, the flow composition and the solute diffusivities, but is a manifestly positive quantity. Similarly, from (4.5) the real part of the temporal frequency is

$$\begin{aligned} \Re(\omega) &= ku^{(0)}_{\alpha} + \frac{\kappa^{(0)}_{\mathbf{u}} J_{\mathbf{u}}}{\kappa^{(0)}_{\eta}} \\ &= \frac{\mathrm{Eu}}{\kappa^{(0)}_{\eta}(1+\delta)(\delta+\lambda)} \Big(\tfrac{1}{2}\big(k_+^2 \mathscr{D}g_{1-\alpha} + k_-^2 \mathscr{D}g_{1+\alpha}\big)\big(\lambda-\delta^2\big)(\lambda-1) + 2k\kappa^{(0)}_{\eta}\delta \Big) \ . \end{aligned} \tag{4.9}$$

Consequences of these results are discussed in Section 6.1.

4.2 *Case II:* $0 < \mathrm{Cr} < \infty$ *and* $\mathrm{Eu} = 0$

In the absence of a driving pressure gradient, the base state is quiescent (note especially that $J_{\mathbf{u}} = 0$, while $J_\eta = -\omega$) and the governing equations for the concentration perturbations become

$$\begin{gathered} \big(\mathscr{D}^2 - K_j^2(\omega)\big)\chi^{(1)}_j + \frac{ikG_{\chi,j}}{\mathrm{Cr}\,\Lambda_j}\psi^{(1)}_j = 0 \ , \\ \text{where} \qquad K_j^2(\omega) = k^2 + K_{0j}^2(\omega) \qquad \text{with} \qquad K_{0j}^2(\omega) = -\frac{i\omega}{\mathrm{Cr}\,\Lambda_j} \ . \end{gathered} \tag{4.10}$$

Following our earlier style, the notation is simplified by adopting the definitions:

$$C_{j,\xi} \equiv \cosh\big(K_j\xi\big) \ , \ S_{j,\xi} \equiv \sinh\big(K_j\xi\big) \ . \tag{4.11}$$

Although the ODEs (4.10) are inhomogeneous, the coefficients K_j^2 are constant in space, so explicit solutions are readily obtained. The complementary functions comprise

$$\Psi_j(y) = C_{j,y} \ \text{ and } \ \Phi_j(y) = S_{j,y} \ , \tag{4.12}$$

with the simple spatially uniform Wronskian $\mathscr{W}\big(\Psi_j(\xi),\ \Phi_j(\xi)\big) = K_j(\omega)$. A lengthy but straightforward calculation of the particular integrals leads to the dispersion relation (see the appendix Section 9.2)

$$\mathscr{L}^{(1)}_{k,\alpha}(\Lambda)\Big(-\kappa^{(1)}_{\eta}\omega + \kappa^{(1)}_{\perp\boldsymbol{\sigma}}J_{\perp\boldsymbol{\sigma}}\Big) + \Lambda\mathscr{L}^{(1)}_{k,\alpha}(1)\kappa_{\parallel\boldsymbol{\sigma}}J_{\parallel\boldsymbol{\sigma}} = 0 \ , \tag{4.13}$$

where (cf. (4.4))

$$\mathscr{L}^{(1)}_{k,\alpha}(\Lambda) = K_2\Lambda C_{2,1-\alpha}S_{1,1+\alpha} + K_1 C_{1,1+\alpha}S_{2,1-\alpha} \ . \tag{4.14}$$

The result (4.13) follows the general form (3.17) but with the Poiseuille flow term absent. As the frequency ω is now intimately incorporated into the arguments of transcendental functions, it is not expedient to explicitly extract the growth rate $\Im(\omega)$ or oscillation rate $\Re(\omega)$ despite the ready availability of (4.13). Nevertheless, implementation of (4.13) (MATLAB, 2013) provides a useful verification tool for other numerical solution schemes (see Section 5.2).

5. General solution

5.1 *Case III:* $0 < \mathrm{Cr} < \infty$ *and* $\mathrm{Eu} \neq 0$

The governing equations for the concentration perturbations become

$$\left(\mathscr{D}^2 - \left(K_j^2(\omega) + \frac{iku_j^{(0)}}{\mathrm{Cr}\,\Lambda_j}\right)\right)\chi_j^{(1)} + \frac{ikG_{\chi,j}}{\mathrm{Cr}\,\Lambda_j}\,\psi_j^{(1)} = 0 \ , \tag{5.1}$$

where $u_j^{(0)}$ is quadratic in y as given by (3.2). In the base state, the parabolic velocity profiles of (3.2) share a common symmetry axis located at (see Figure 2)

$$y = \bar{y} = \frac{\delta(1-\lambda)}{(1+\delta)(\delta+\lambda)} \ . \tag{5.2}$$

On applying the transformation

$$Y(y) = \left(\frac{2ik\,\mathrm{Eu}}{\mathrm{Cr}\,\Lambda_j}\right)^{1/4}\left(y - \bar{y}\right) \ , \tag{5.3}$$

the homogeneous equation corresponding to (5.1) is brought into the standard form

$$\left(\frac{\mathrm{d}^2}{\mathrm{d}Y^2} + \left(\tfrac{1}{4}Y^2 - \Upsilon_j(\omega)\right)\right)\chi_j^{(1)} = 0 \ , \tag{5.4}$$

where

$$\Upsilon_j(\omega) = \left(K_j^2(\omega) + \frac{ik\bar{u}_j^{(0)}}{\mathrm{Cr}\,\Lambda_j}\right)\left(\frac{2ik\,\mathrm{Eu}}{\mathrm{Cr}\,\Lambda_j}\right)^{-1/2} \ , \tag{5.5}$$

and we have the complementary solution in terms of a single parabolic cylinder (Weber) function (Abramowitz & Stegun, 1965)

$$\Psi_j(y) = W\left(\Upsilon_j,\, y\right) \ \text{and} \ \Phi_j(y) = W\left(\Upsilon_j,\, -y\right) \ , \tag{5.6}$$

with the constant Wronskian $\mathscr{W} = 1$. These analytic solutions of the transport equations (5.1) lead to a very complicated implicit dispersion relation involving transcendental functions. It appears very difficult (if not impossible) to exactly solve this eigenvalue problem, or merely to establish precisely how many response modes exist. Here we shall consider a numerical scheme instead, that will resolve these issues.

5.2 *A numerical scheme: Chebyshev collocation method*

Recall the stream function perturbations $\psi_j^{(1)}$ satisfy a biharmonic field equation (3.9), that is equivalent to the Orr-Sommerfeld equation at vanishing Reynolds number, and explicit solutions are obtained in the form (3.10). Following Gottlieb & Orszag (1977), the set of orthogonal Chebyshev polynomials $T_n : [-1,1] \to [-1,1]$ provides an appropriate basis for the approximation space of $\chi_j^{(1)}$ and we write the truncated expansions

$$\chi_j^{(1)}(y) = \sum_{n=0}^{N_j} a_{jn} T_n\left(y_j(y)\right) \ , \tag{5.7}$$

where the spanwise coordinate is linearly mapped onto the canonical domain:

$$\begin{aligned} y_1(y) &= (1+\delta)y+\delta \ , \ (-1 \leqslant y \leqslant \alpha) \ , \\ y_2(y) &= \frac{1}{\delta}\Big((1+\delta)y-1\Big) \ , \ (\alpha \leqslant y \leqslant 1) \ , \end{aligned} \tag{5.8}$$

with the differential transformations,

$$\mathscr{D}y_1 = 1+\delta \qquad \text{and} \qquad \mathscr{D}y_2 = 1+\frac{1}{\delta} \ . \tag{5.9}$$

The Gauss-Lobatto points,

$$y_{jn} = \cos\left(\frac{n\pi}{N_j}\right) \ , \ \big(n = 0,\ 1,\ 2,\ \dots,\ N_j\big) \ . \tag{5.10}$$

corresponding to the extrema of the highest order polynomial, are optimal for collocation (Schmid & Henningson, 2001). Altogether with the linearised boundary conditions (3.15), this set of governing equations is assembled into the system

$$\mathbf{Aw} = \omega\mathbf{Bw} \ , \tag{5.11}$$

which we recognise as a generalised eigenvalue problem for the eigenvalue ω and the associated eigenvector

$$\mathbf{w} = \big(a_{10} \quad \dots \quad a_{1N_1} \quad a_{20} \quad \dots \quad a_{2N_2} \quad \hat{A}_1 \quad \hat{B}_1 \quad \hat{C}_1 \quad \hat{D}_1 \quad \hat{A}_2 \quad \hat{B}_2 \quad \hat{C}_2 \quad \hat{D}_2 \quad \mathscr{A}\big)^T \ . \tag{5.12}$$

These N_1+N_2+11 unknowns are determined by the 13 boundary conditions along with the field evaluations at the $\big(N_1-1\big)+\big(N_2-1\big)$ "interior" collocation points corresponding to the turning points of T_{N_1} and T_{N_2}. A Matlab code (MATLAB, 2013) has been implemented using the built-in routine `eig` to solve the generalised eigenvalue problem. To consistently compare results across the wavenumber spectrum, the eigenvectors are uniformly scaled so that the disturbance amplitude of the interface becomes $\mathscr{A} = 1 \in \mathbb{R}$.

5.3 *The situation* $k = 0$ *and* $\mathrm{Eu} \geqslant 0$

At zero wavenumber, it turns out that a base state flow plays no role in the eigenvalue spectrum. The governing equations (3.9) for the stream function perturbations reduce to

$$\mathscr{D}^4\psi_j^{(1)} = 0 \ , \tag{5.13}$$

with general solutions in the form of a cubic polynomial

$$\psi_j^{(1)} = \hat{A}_j y^3 + \hat{B}_j y^2 + \hat{C}_j y + \hat{D}_j \ . \tag{5.14}$$

The concentration field perturbations are also determined by homogeneous ODEs

$$\big(\mathscr{D}^2 - K_{0j}^2(\omega)\big)\,\chi_j^{(1)} = 0 \ , \tag{5.15}$$

with general solutions (cf. (3.12))

$$\chi_j^{(1)} = \frac{2\Delta_\chi}{\mathrm{Mg}}\big(\hat{F}_j\,C_{j,y} + \hat{G}_j\,S_{j,y}\big) \ . \tag{5.16}$$

Furthermore, the interfacial stress boundary conditions are simplified considerably: in particular the tangential coupling between $\psi_j^{(1)}$ and $\chi_j^{(1)}$ is broken so that the dispersion relation is easily recovered

$$\omega\,\mathscr{L}^{(1)}_{0,\alpha}(\Lambda)\left(\frac{\lambda^2+2\delta\left(2\delta^2+3\delta+2\right)\lambda+\delta^4}{(1+\delta)^4}\right)=0\ , \tag{5.17}$$

and the non-trivial modes are determined by (cf. (4.14))

$$\mathscr{L}^{(1)}_{0,\alpha}(\Lambda)=K_0\left(\sqrt{\Lambda}\cosh\left(K_0h_-\right)\sinh\left(K_0h_+\right)+\cosh\left(K_0h_+\right)\sinh\left(K_0h_-\right)\right)=0\ , \tag{5.18}$$

where

$$h_-=\frac{2\delta}{(1+\delta)\sqrt{\Lambda}}=\frac{1-\alpha}{\sqrt{\Lambda}}\ ,\qquad h_+=\frac{2}{1+\delta}=1+\alpha\qquad\text{and}\qquad K_0=\sqrt{-\frac{i\omega}{\mathrm{Cr}}}\ . \tag{5.19}$$

6. Results and discussion

6.1 *Instantaneous solute diffusion* $\mathrm{Cr}\to\infty$, $0<\Lambda<\infty$ *(Case I)*

Explicit expressions for the temporal frequency in Case I (4.7 and 4.9) permit detailed analysis of the linear response. For all physical parameter values, the quantity $\kappa_\eta^{(0)}$ is strictly positive (see the appendix Section 9.3). It follows from (4.7) that the interface is generally stable ($\Im(\omega)<0$) against large wavenumber perturbations ($k\to\infty$). By considering the k-expansion

$$\Im(\omega)=\frac{\mathrm{Mg}\left(\lambda-\delta^2\right)\Lambda\delta^2}{\left(\lambda^2+2\delta\left(2+3\delta+2\delta^2\right)\lambda+\delta^4\right)(\Lambda+\delta)^2}\,k^2+O\left(k^4\right)\ , \tag{6.1}$$

a region of instability exists for $\mathrm{Mg}>0$ provided $\lambda>\delta^2$. Conversely, $\mathrm{Mg}<0$ requires $\lambda<\delta^2$ for this instability to appear. Hence, it is natural to define a *pseudo*-critical viscosity ratio $\lambda_c=\delta^2$. It should be emphasised here that this is a small wavenumber analysis that does not exclude the possibility of instabilities where $\Im(\omega)$ first becomes positive for some wavenumber $k_c>0$.

These response characteristics are confirmed by the family of dispersion curves plotted in Figure 3 where, given $\mathrm{Mg}=100$, panels a), b) and c) consistently exhibit a stable response for $\lambda>\delta^2$, a marginal state at $\lambda=\delta^2$ and instability for $\lambda<\delta^2$. Within the systematic classification scheme of Cross and coworkers (Cross & Hohenberg, 1993; Cross & Greenside, 2009), this is a stationary instability of Type-II universally characterised by a zero growth rate at $k=0$ and maximum amplification rate at intermediate wavenumber $0<k<\infty$. Figure 3 also demonstrates the stability criterion is independent of the mass diffusivity ratio Λ. This is unsurprising in the limit ($\mathrm{Cr}\to\infty$), since equilibration of the concentration profile is fast compared with the flow dynamics: the interface moves in a concentration field that is oblivious to the fluid flows. Despite this decoupling, the concentration field is perturbed nevertheless (see (4.3)) by a stratification of the bulk mass diffusivity (Figure 3d). Throughout Figure 3 the analytic results (Section 4.1) show excellent agreement with the approximate collocation computations (Section 5.2).

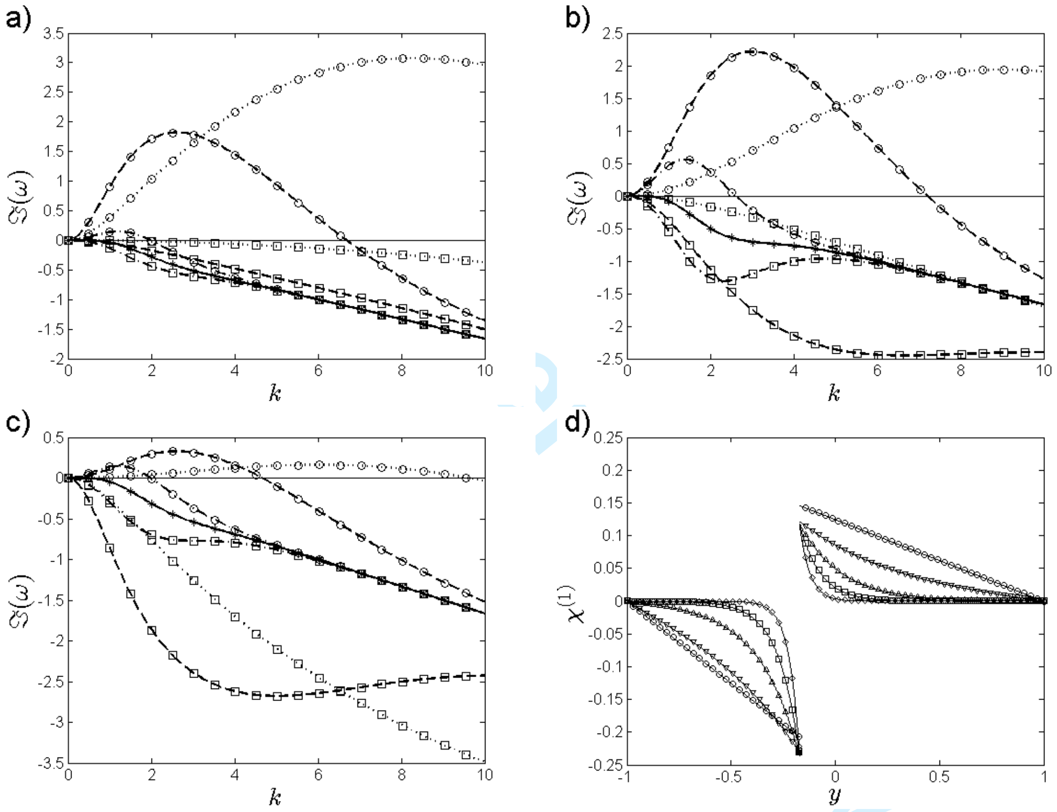

FIG. 3. Growth rate dispersion curves for Case I ($\mathrm{Cr} \to \infty$) are displayed for parameter values $\mathrm{Mg} = 100$, $\lambda = 2$ and $\Delta_\chi = 1$ with a) $\Lambda = 0.1$; b) $\Lambda = 1$ and c) $\Lambda = 10$. Results from the analytic expression (4.7), shown as lines, are compared with isolated point calculations using the numerical collocation method (denoted by symbols) described in Section 5.2 with $N_1 = N_2 = 32$. Entirely stable response is indicated by squares with the flow composition parameter δ set to $40(\cdots)$, $10(--)$ and $2(\cdot-\cdot)$. Circles identify response curves showing the small wavenumber instability with δ set to $1(\cdot-\cdot)$, $0.2(--)$ and $0.05(\cdots)$. The marginally stable response is plotted with asterisk symbols and a full line (——) where $\delta_c = \sqrt{\lambda} = \sqrt{2}$.
At the stability margin ($\lambda = 2$ and $\delta = \sqrt{2}$ with $\mathrm{Mg} = 100$, $\Delta_\chi = 1$ and $\Lambda = 2$), panel d) shows a corresponding comparison of concentration perturbation profiles across the slab where results from (4.3) are plotted as lines and collocation calculations are denoted by symbols with wavenumbers k set to 0.1(○), 2(▽), 5(△), 10(□) and 20(◇).

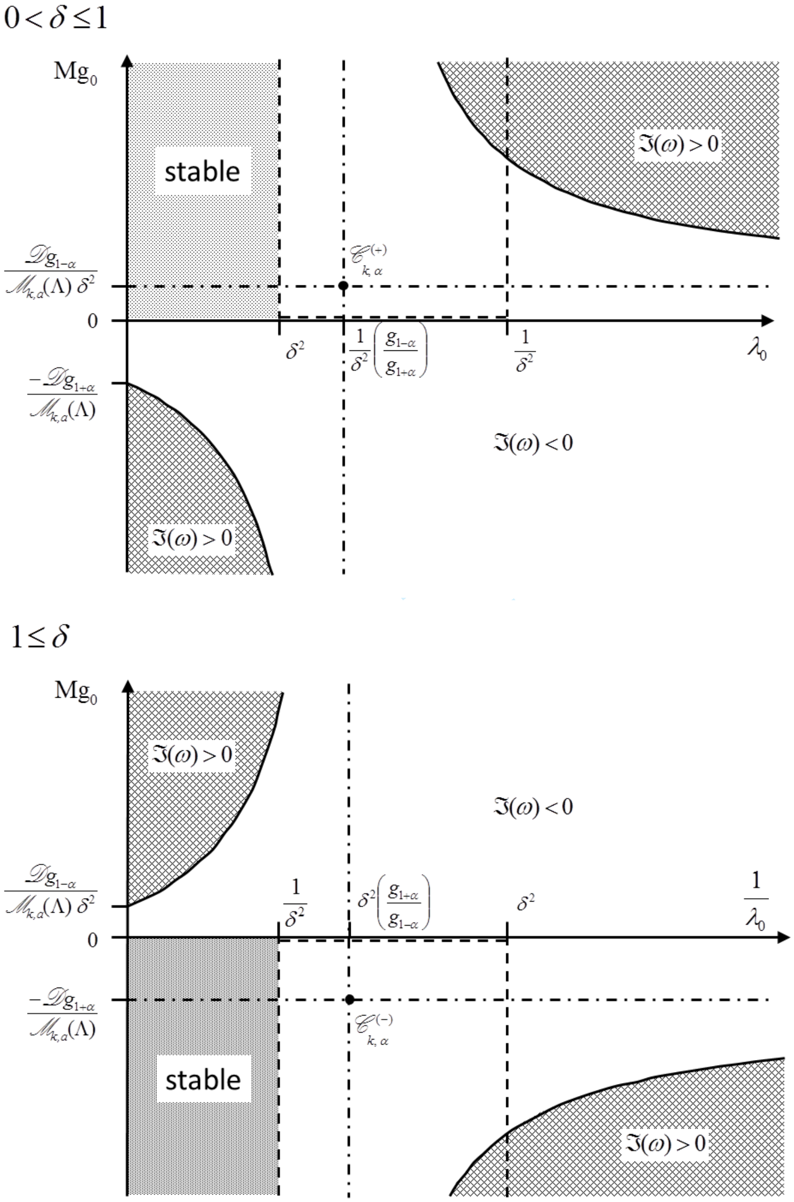

FIG. 4. Stability diagram for Case I $\left(\mathrm{Cr}\to\infty \text{ and } 0<\Lambda<\infty\right)$. Typical marginal stability boundaries $\left(\Im(\omega)=0\right)$ projected into the plane of viscosity ratio λ_0 and Gibbs elasticity Mg_0 appear as a rectangular hyperbola (——). With varying excitation wavenumber k, the asymptotes $(\cdot-\cdot)$ move about the plane but the centre $\mathscr{C}^{(\pm)}_{k,\alpha}$ is confined to the unbounded rectangular region indicated $(--)$. Provided $\lambda_0<\lambda_c=\delta^2$, a domain of stability (shaded area) can be identified where all linear perturbations decay in time.

For arbitrary wavenumber, marginal stability relations $\big(\Im(\omega)=0\big)$ are obtained directly from (4.7), and solving for the interfacial elasticity parameter yields

$$\mathrm{Mg}_0 = \frac{g_{1+\alpha}\mathscr{D}g_{1-\alpha}\,\lambda_0 + g_{1-\alpha}\mathscr{D}g_{1+\alpha}}{\mathscr{M}_{k,\alpha}(\Lambda)\big(g_{1+\alpha}\delta^2\,\lambda_0 - g_{1-\alpha}\big)} = \frac{g_{1+\alpha}\mathscr{D}g_{1-\alpha} + g_{1-\alpha}\mathscr{D}g_{1+\alpha}\,\lambda_0^{-1}}{\mathscr{M}_{k,\alpha}(\Lambda)\big(g_{1+\alpha}\delta^2 - g_{1-\alpha}\,\lambda_0^{-1}\big)} \quad , \tag{6.2}$$

where Mg_0 and λ_0 are marginal values of the corresponding control parameters. This is a special case of the result first obtained by Smith (1966) (see the appendix, Section 9.4) for the analogous thermocapillary situation, but where a neutral stability criterion was imposed *before* solving the eigenvalue problem. Equations (6.2) describe rectangular hyperbolae, centred on a point denoted $\mathscr{C}_{k,\alpha}^{(+)}$ in the $\big(\lambda_0,\ \mathrm{Mg}_0\big)$ plane, or centred on $\mathscr{C}_{k,\alpha}^{(-)}$ in the $\big(\lambda_0^{-1},\ \mathrm{Mg}_0\big)$ plane with coordinates

$$\mathscr{C}_{k,\alpha}^{(+)} = \left(\frac{1}{\delta^2}\left(\frac{g_{1-\alpha}}{g_{1+\alpha}}\right),\ \frac{\mathscr{D}g_{1-\alpha}}{\delta^2\mathscr{M}_{k,\alpha}(\Lambda)}\right) \quad \text{and} \quad \mathscr{C}_{k,\alpha}^{(-)} = \left(\delta^2\left(\frac{g_{1+\alpha}}{g_{1-\alpha}}\right),\ -\frac{\mathscr{D}g_{1+\alpha}}{\mathscr{M}_{k,\alpha}(\Lambda)}\right) \quad . \tag{6.3}$$

Since g is both positive and strictly increasing (see definitions (4.6)), it is easy to verify

$$\begin{aligned} &0<\delta<1 \ \Rightarrow\ 0<\alpha<1 \ \Rightarrow\ \delta^4 < \frac{g_{1-\alpha}}{g_{1+\alpha}} < 1 \ , \\ &1<\delta<\infty \ \Rightarrow\ -1<\alpha<0 \ \Rightarrow \frac{1}{\delta^4} < \frac{g_{1+\alpha}}{g_{1-\alpha}} < 1 \\ &\text{and} \qquad \lim_{k\to\infty}\frac{\mathscr{D}g_{1\pm\alpha}}{\mathscr{M}_{k,\alpha}(\Lambda)}\ \exp\big(-2k_{\pm}\big) = 0 \ , \end{aligned} \tag{6.4}$$

so that the positions $\mathscr{C}_{k,\alpha}^{(\pm)}$ are restricted as shown in Figure 4. It follows that global temporal stability is confined to the λ_0 axis (where $\mathrm{Mg}_0=0$) and either the region $\big(\lambda_0,\ \mathrm{Mg}_0\big)\in\big(0,\ \delta^2\big)\times(0,\ \infty)$ for $0<\delta\leqslant 1$, or the region $\big(\lambda_0^{-1},\ \mathrm{Mg}_0\big)\in\big(0,\ \delta^2\big)\times(-\infty,\ 0)$ for $1\leqslant\delta$. This is consistent with the small wavenumber analysis and confirms the critical viscosity ratio $\lambda_c=\delta^2$. With a more conventional insoluble surfactant ansatz, the same result has been established in the small-k analysis of Frenkel & Halpern (2002) and the lubrication-flow model of Blyth & Pozrikidis (2004a). A similar asymptotic analysis reported by Merkt et al. (2005) has also obtained stability diagrams (their Figure 4) consistent with Figure 4.

A mechanical interpretation of this small wavenumber instability is illustrated in Figure 5. Merkt et al. (2005) have also discussed a similar mechanism in the context of competition between capillary action and the Rayleigh-Taylor instability for systems with mass density stratification. Large scale disturbances are suppressed by a destructive normal fluid velocity component with a π phase shift (Figure 5a and 5b), while changes in γ remain in-phase with the interface profile. At the margin of stability (Figure 5c and 5d) $v^{(1)}(y)$ swaps, on passing through the interface, from constructive in-phase to destructive out-of-phase interference with the disturbance wave. An unstable response is characterised by an in-phase normal velocity component that amplifies the interfacial disturbance (Figure 5e and 5f). In steady Stokes flow, the vorticity

$$\boldsymbol{\varpi}_j = \nabla\times\mathbf{u}_j = \left(\frac{\partial v_j}{\partial x} - \frac{\partial u_j}{\partial y}\right)\mathbf{k} = -\nabla^2\psi_j\,\mathbf{k} \ , \tag{6.5}$$

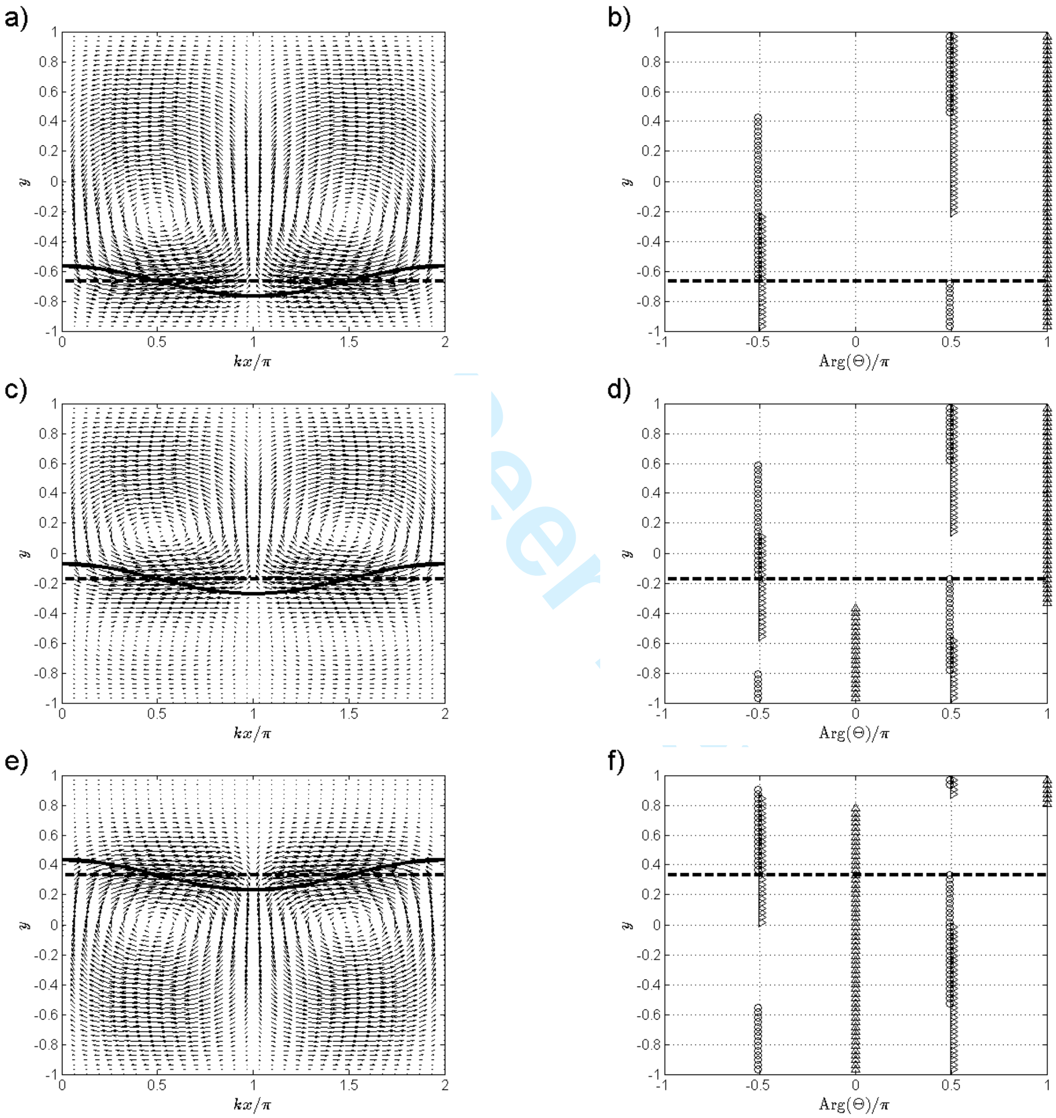

FIG. 5. Flow fields calculated by the collocation method $\left(N_1 = N_2 = 32\right)$ are shown for Case I with $\mathrm{Cr} \to \infty$. Throughout, the control parameter values $\mathrm{Mg} = 5$, $\mathrm{Eu} = 0$, $\lambda = 2$, $\Lambda = 1$, $\Delta_\chi = 1$ are set.

Panels (a), (c) and (e): direction fields associated with the fluid velocity $\mathbf{u}(x,\ y) = u(x,\ y)\mathbf{i} + v(x,\ y)\mathbf{j}$ are plotted. The superimposed lines indicate the quiescent interface position $(--)$ and a harmonic disturbance (——) of arbitrary amplitude $(\varepsilon = 0.1)$.

Panels (b), (d) and (f): show the corresponding principal arguments of the perturbed velocities and vorticity field $\Theta \in \left\{u^{(1)}(y),\ v^{(1)}(y),\ \varpi^{(1)}(y)\right\}$. The tangential $u^{(1)}$ and normal $v^{(1)}$ velocity components are denoted by $(\triangleright)$ and $(\triangle)$, respectively, and the phase of the vorticity $\varpi^{(1)}$ is indicated by $\bigcirc$. Again, the quiescent interface position is shown by $(--)$.

Each pair of panels indicates a stable situation ($\delta = 5$, a and b); a marginal situation ($\delta = \sqrt{2}$, c and d) and an unstable situation ($\delta = 0.5$, e and f).

is harmonic $\nabla^2 \boldsymbol{\varpi}_j = \mathbf{0}$ (cf. (2.4)) and closely related to the pressure so that $\lambda_j \big(\partial \boldsymbol{\varpi}_j / \partial x\big) = \big(\partial p_j / \partial y\big)\mathbf{k}$ and $\lambda_j \big(\partial \boldsymbol{\varpi}_j / \partial y\big) = \big(\partial p_j / \partial x\big)\mathbf{k}$. Consequently, the vorticity is discontinuous at the interface and the phase of the perturbation $\mathrm{Arg}\big(\varpi^{(1)}\big)$ changes abruptly at $y = \alpha$ from a $\pi/2$ lag in the more viscous film to a $\pi/2$ lead in the less viscous layer (Figure 5b, d and f). It appears the pressure is always destructively out of phase with the interface deformation over the whole fluid slab (data not shown). Although four convection cells are evident in the marginal state (Figure 5c and 5d), only two cells develop for states lying deep in either the stable (e.g., Figure 5a and 5b) or unstable (data not shown) regimes. This contrasts with several studies of the analogous thermocapillary problem (Andereck et al., 1998) that focussed on different flow patterns, but where four cells are always generated by imposing a rigid undeformable interface.

In this special Case I, only a single response mode is excited that always remains completely decoupled from the base state flow: the growth rate $\Im(\omega)$ given by (4.7) is independent of Eu. For a quiescent base state flow the disturbance is, of course, stationary in space $\big(\Re(\omega) = 0\big)$, but if a pressure gradient exists $(\mathrm{Eu} > 0)$ it can be deduced from (4.9) that $\Re(\omega) > 0$ (see the appendix Section 9.5) and a propagating wave develops on the interface that travels downstream with the speed

$$\begin{aligned} \frac{\Re(\omega)}{k} &= u_\alpha^{(0)} + \frac{\kappa_{\mathbf{u}}^{(0)} J_{\mathbf{u}}}{k\kappa_\eta^{(0)}} \\ &= \frac{\mathrm{Eu}}{\kappa_\eta^{(0)}(1+\delta)(\delta+\lambda)} \left(\left(\frac{k_+^2 \mathscr{D} g_{1-\alpha} + k_-^2 \mathscr{D} g_{1+\alpha}}{k_+ + k_-} \right) (\lambda - \delta^2)(\lambda - 1) + 2\kappa_\eta^{(0)} \delta \right) \ . \end{aligned} \tag{6.6}$$

Further, by setting $\mathrm{Eu} = \frac{1}{2}(1+\delta)(\delta+\lambda)/\delta$, or equivalently demanding the horizontal fluid velocity component satisfy $u_\alpha^{(0)} = 1$, and also choosing $\delta = 1$ before finally considering the limit $k \to \infty$, we recover the dispersionless result

$$\frac{\Re(\omega)}{k} = 1 + \frac{2(1-\lambda)^2}{\lambda^2 + 14\lambda + 1} \ , \tag{6.7}$$

obtained by Yih (1967) for the plane Poiseuille flow in a finite channel of two superposed fluids with equal depth and density, but different viscosities.

6.2 *Comparable diffusion rates of matter and momentum* $0 < \mathrm{Cr} < \infty$ *(Case II)*

At finite crispation numbers (Case II and III), the response behaviour is qualitatively very different (see Figure 6 for example) from Case I (Section 6.1). Analysis of the $k = 0$ situation (see the appendix Section 9.6) shows that the temporal frequency has zero real part $\big(\Re(\omega) = 0\big)$ and non-positive imaginary part $\big(\Im(\omega) \leqslant 0\big)$. Indeed, the dispersion relation (5.18) reduces to

$$\sqrt{\Lambda} \sin\left(h_+ \sqrt{-\frac{\Im(\omega)}{\mathrm{Cr}}} \right) \cos\left(h_- \sqrt{-\frac{\Im(\omega)}{\mathrm{Cr}}} \right) + \cos\left(h_+ \sqrt{-\frac{\Im(\omega)}{\mathrm{Cr}}} \right) \sin\left(h_- \sqrt{-\frac{\Im(\omega)}{\mathrm{Cr}}} \right) = 0 \ . \tag{6.8}$$

Formally, this defines the nodes of a wave with two harmonic components differing in both frequency and amplitude described by

$$\big(\sqrt{\Lambda} + 1\big) \sin\left(\frac{2}{1+\delta} \left(1 + \frac{\delta}{\sqrt{\Lambda}}\right) \sqrt{-\frac{\Im(\omega)}{\mathrm{Cr}}} \right) + \big(\sqrt{\Lambda} - 1\big) \sin\left(\frac{2}{1+\delta} \left(1 - \frac{\delta}{\sqrt{\Lambda}}\right) \sqrt{-\frac{\Im(\omega)}{\mathrm{Cr}}} \right) = 0 \ . \tag{6.9}$$

A general closed form solution of (6.9) is intractable. If $\Lambda = 1$, however, the second term vanishes in (6.9) and a simple expression, independent of δ, is obtained for the growth rate spectrum

$$\sqrt{-\frac{\Im(\omega)}{\mathrm{Cr}}} = m\,\frac{\pi}{2} \ , \qquad (m = 0,\ 1,\ 2, \ldots) \ . \tag{6.10}$$

Similarly, if $\Lambda = \delta^2$, then

$$\frac{1}{1+\delta}\sqrt{-\frac{\Im(\omega)}{\mathrm{Cr}}} = m\,\frac{\pi}{4} \ , \qquad (m = 0,\ 1,\ 2, \ldots) \ . \tag{6.11}$$

In both these special situations, the mode spacing is proportional to $(2m+1)\mathrm{Cr}$. More generally, expansion of (6.9) to order $\mathrm{Cr}^{-3/2}$ demonstrates that the first harmonic $(m = 1)$ is always shifted from the fundamental $(m = 0)$ by an amount proportional to Cr. This is consistent with the finding from Case I $(\mathrm{Cr} \to \infty)$ where only the single $m = 0$ response remains and all other modes have retreated to infinity.

Figure 6a compares Case II growth rate dispersion curves at control parameter values corresponding to a stable Case I response: $\lambda = 2$ and $\delta = \sqrt{40} > \sqrt{\lambda}$ with $\mathrm{Mg} = 100$, $\Lambda = 1$ and $\Delta_\chi = 1$ (Figure 3b). For $\mathrm{Cr} \geqslant 1$ the dominant mode is stable and qualitatively similar to the Case I situation. The most obvious departure from Case I is the appearance of multiple lower lying modes whose character and interactions sensitively depend on control parameters other than viscosity ratio λ and geometry δ. In particular, at $\mathrm{Cr} = 1$ an avoided crossing is evident between the fundamental and the first harmonic, but for larger crispation number the two highest stationary modes pass through an exceptional point where a pair of spatially propagating waves are excited that travel in opposite directions with phase velocities of equal magnitude. There is also evidence in Figure 6a of a second exceptional point at higher wavenumber $(k \approx 4)$ where the superposed response splits back to two standing wave modes with distinct temporal decay rates. Moreover, at $\mathrm{Cr} = 50$ (see inset of Figure 6a) the combined oscillatory mode exhibits an *instability* of Type I in the classification Cross and coworkers (Cross & Hohenberg, 1993; Cross & Greenside, 2009). In contrast with Type-II behaviour, Type-I is characterised by the onset of instability at a *nonzero* wavenumber. For standing wave modes, Figure 6a also includes direct numerical solutions of the dispersion relation (4.13) obtained with the Matlab `fsolve` routine using the Levenberg-Marquardt algorithm (Fan, 2003). The excellent agreement serves again to verify both the analysis and the collocation method implementation. Conversely, at parameter values corresponding to an unstable response in Case I, $(\lambda = 2,\ \delta = 1/\sqrt{10},\ \mathrm{Mg} = 20,\ \Lambda = 1,\ \Delta_\chi = 1)$ increasing the interfacial tension has a stabilising effect and reduces the maximum temporal growth rate as shown in Figure 6b. The diversity of response behaviour is also apparent here with multiple splittings between states having either monotone or oscillatory time dependence in the decay rate. Excitation of spatially propagating waves is confirmed in Figure 6c where nonzero $\Re(\omega)$ appears and coincides with the linear superposition of two modes to form a stationary solution in space that oscillates in time. At very high surface tension $(\mathrm{Cr} = 0.0002)$, an unstable oscillatory response can be observed as shown in Figure 6d. An example of mode *exchange* is also apparent $(k \approx 3)$ where a single stationary mode emerges to dominate a standing wave pair without passing through an exceptional point.

The previously noted (Figure 6a) avoided-crossing or level-repulsion phenomenon (Lax, 2007) is linked with the likelihood that a given operator has eigenvalues with nontrivial algebraic multiplicity (Betcke & Trefethen, 2004). Figure 7a examines the effect more closely where, at fixed interfacial tension $\mathrm{Cr} = 0.1$, growth rate dispersion curves are plotted for $5 \leqslant \mathrm{Mg} \leqslant 100$ with $\mathrm{Eu} = 0$, $\delta = \lambda = 2$,

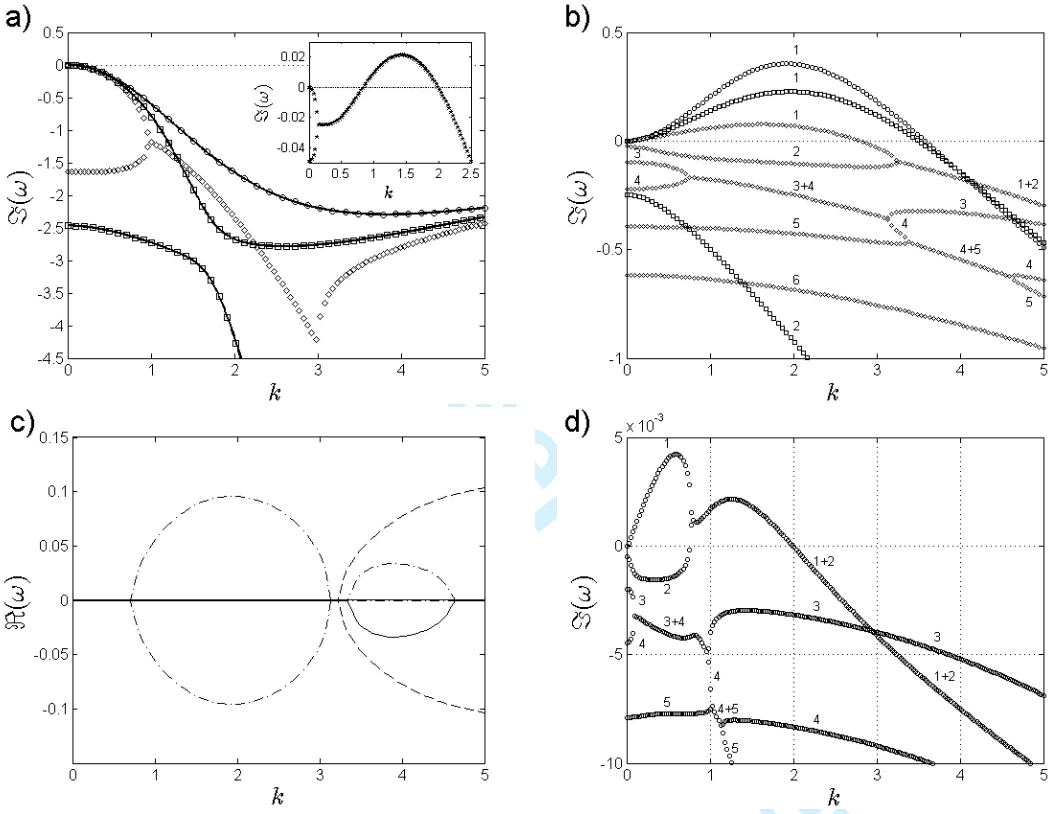

FIG. 6. Temporal frequency dispersion curves $\omega = \omega(k)$ are shown for a fluid slab of uniform mass diffusivity $(\Lambda = 1)$ and unit concentration difference on the bounding walls $(\Delta_\chi = 1)$.
Panel a): at $\mathrm{Mg} = 100$, the growth rate $\Im(\omega)$ is compared between Case I $(\mathrm{Cr} \to \infty)(\bigcirc)$ and Case II $(\mathrm{Eu} = 0)$ with finite Cr set to $1(\square)$, $1.5(\diamond)$ and $50(\star)$, all obtained by the collocation method (Section 5.2). Other control parameters are $\lambda = 2$ and $\delta = \sqrt{40} > \sqrt{\lambda}$ corresponding to a stable response in Case I. Solid lines correspond to evaluation of the explicit result (4.7) in Case I, and to numerical solutions of the dispersion relation (4.13) in Case II.
Panel b): at $\mathrm{Mg} = 20$, the growth rate $\Im(\omega)$ is compared between Case I $(\mathrm{Cr} \to \infty)(\bigcirc)$ and Case II $(\mathrm{Eu} = 0)$ with finite Cr set to $0.1(\square)$ and $0.01(\diamond)$, all obtained by the collocation method (Section 5.2). Other control parameters are $\lambda = 2$ and $\delta = 1/\sqrt{10} < \sqrt{\lambda}$ corresponding to an unstable response in Case I. Modes are identified by number and oscillatory responses are indicated by linear superposition of stationary states between a pair of exceptional points.
Panel c): the spatially propagating wave frequencies $\Re(\omega)$ are shown, corresponding to the data of panel b) for $\mathrm{Cr} = 0.01$. Modes are identified as follows: 1 and 2 $(--)$; 3 and 4 $(\cdot - \cdot)$; and 5 (——).
Panel d): shows the growth rate $\Im(\omega)$ dispersion curves, obtained by the collocation method (Section 5.2), in a situation where mass diffusion is extremely slow $\mathrm{Cr} = 0.0002$. Other control parameters are set as in panel b). Modes are identified by number. An unstable oscillatory state is observed $(k < 1)$ as well as a dominant mode exchange crossing at $k \approx 3$.

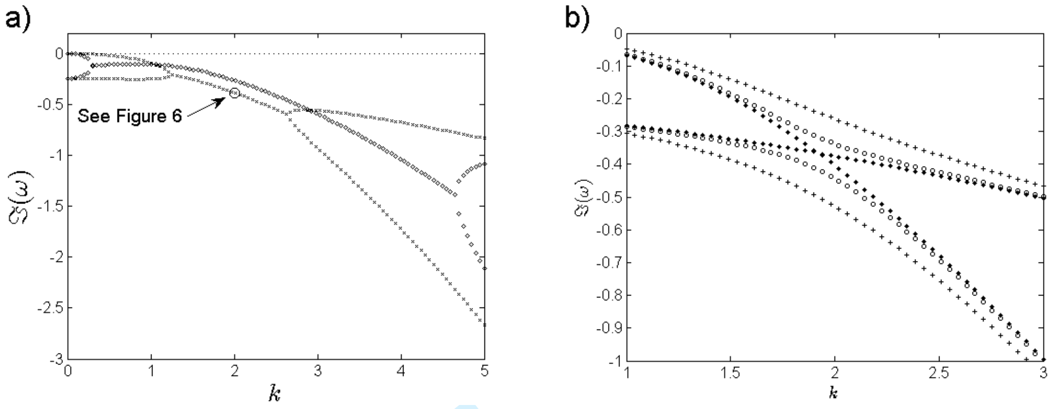

FIG. 7. Collapse of avoided crossing between stationary modes to form oscillatory mode with increasing interfacial elasticity is illustrated. Growth rate dispersion curves $\Im\left(\omega(k)\right)$ are plotted in panel a) for Mg set to $5(+)$, $7(\Box)$, and in panel b) for Mg set to $7.35(\star)$, $10(\times)$ and $100(\Diamond)$. Other control parameters are $\mathrm{Ca} = 0.1$, $\mathrm{Eu} = 0$, $\delta = \lambda = 2$, $\Lambda = 1$ and $\Delta_\chi = 1$.

$\Lambda = 1$ and $\Delta_\chi = 1$. As the interfacial elasticity increases, two distinct avoiding modes approach more and more closely at $k \approx 2$, then merge at a single point near $\mathrm{Mg} = 7.35$ that subsequently decomposes into a pair of exceptional points at higher Mg.

Seyranian et al. (2005) have reported a theory of strong coupling between eigenvalues of a complex valued matrix with respect to the smooth variation of parameters upon which the coefficients depend. In a finite-dimensional vector space, an exceptional point (Kato, 1980) arises where two eigenvalues coalesce to give an algebraic multiplicity of 2, but a smaller geometric multiplicity of 1. Thus, the corresponding eigenvectors also merge, becoming linearly dependent and forming a nontrivial Jordan block that renders the underlying matrix defective (not diagonalizable over $\mathbb{C}$). In the situation where only a single parameter is varied (the wavenumber k for example), the two eigenvalues collide with infinite "speed" (the derivative with respect to the parameter is unbounded) and subsequently diverge in the perpendicular direction with a complete loss of information on the relationship before and after strong coupling (Seyranian et al., 2005). This phenomenon is entirely consistent with the observed behaviour (Figure 6a with $\mathrm{Cr} = 1.5$, for instance) of mode coupling between independent stationary and combined oscillatory states. Furthermore, the theory of Seyranian et al. (2005) explains characteristic properties of singularities in the surfaces representing complex resonance energy eigenvalues of quantum systems (Hernández et al., 2003) that are manifest as level repulsion in the real and imaginary parts. It remains unclear how the details of this analysis relate to avoided crossings and mode exchanges of $\Im(\omega)(k)$ in stationary states where $\Re(\omega) = 0$.

In the absence of a bulk buoyancy mechanism, and allowing for distortion of the interface, counter-rotating fluid cells are consistently observed in the stationary states (see Figure 5, for example) but the oscillatory standing wave state periodically changes the sense of rotation. The temporal evolution of this pattern is illustrated in Figure 8 by snapshots of the fluid velocity direction field over one cycle. The corresponding interfacial disturbance is also indicated and shows that the flow reversal is associated with instants where the interface adopts its unperturbed flat profile. Note that, for clarity here, the exponential decay of the disturbance in this stable response has been artificially suppressed where the spatial amplitude would otherwise be damped out within a fraction of one temporal cycle.

6.3 *Effect of base state flow* Eu > 0 *(Case III)*

Figure 9a demonstrates the effect of a base state flow in a relatively simple situation with no mode interaction (cf. Figure 6b). The growth rates of instabilities are enhanced with increasing Eu, while a stable response is further suppressed. For the particular parameter set corresponding to Figure 6b, which is unstable in Case I, with $\mathrm{Cr} = 0.1$ it appears that the marginal stability boundary is not sensitive to changes in base state flow. At the interface, a spatially propagating wave is excited that always moves faster than the fluid $\Re(\omega)/k > u_\alpha^{(0)}$. Interestingly, we note that the second stable mode travels almost entirely without dispersion, at least over the wavenumber range $0 < k < 5$. For a more complicated situation involving mode interactions, Figure 9b shows that the symmetry-breaking base state flow destroys the standing wave of the oscillatory state. The excited propagating waves are dispersive, and the dominant mode response is always more slowly moving than the base state flow at the interface.

7. Conclusions and Further Work

To investigate necessary conditions for the onset of turbulent mixing in a two-layer fluid system, the present work considers the influence of a scalar concentration field on the linear stability of a fluid interface subject to small deformations under the regime of Stokes flow. The bulk concentration field is convected by the fluid flow and acts to nonuniformly alter the interfacial tension that, in turn, induces flow by the solutal Marangoni mechanism. This treatment of the solutal Marangoni effect is formally analogous to the thermocapillary effect, which arises when an interface is exposed to a spatially-varying temperature field. In both scenarios, Marangoni tractions develop because of the local interfacial tension dependency on the strength of the ambient scalar field through a suitable constitutive relation. Zeren & Reynolds (1972) presented a linear stability analysis for the analogous thermocapillary problem, which also included the effect of buoyancy, but which assumed that the deformation of the interface was negligible. Interfacial deformation has been accounted for in more recent work by Tavener & Cliffe (2002) using a finite-element method. In the present work, three distinct cases were studied, and we summarise these below.

In Case I, the solute diffusion is supposed to be instantaneous (crispation number $\mathrm{Cr} \to \infty$), but a finite Gibbs elasticity ($0 < \mathrm{Mg} < \infty$) permits interfacial displacements to generate a solutal Marangoni effect. Perturbations of the velocity and concentration fields are decoupled in this limit, so that the dispersion relation $\omega = \omega(k)$ between temporal response frequency ω and spatial excitation frequency k is obtained analytically. Furthermore, the stability behaviour is not sensitive to the mass diffusivity ratio Λ, effectively reducing the number of control parameters so that a complete stability diagram can be established. Only a single response mode is allowed where the interface is always stable to large k perturbations, but a region of unstable solutions exists at small wavenumber under certain conditions: that is a Type II instability in the classification of Cross & Hohenberg (1993). The extent of these regions is found to be independent of the base-state flow field. For $\mathrm{Mg} > 0$, the interface is Type II unstable when the viscosity ratio λ exceeds δ^2, where δ is the fluid film thickness ratio. Conversely, for $\mathrm{Mg} > 0$, unstable response is possible when $\lambda < \delta^2$. By determining the marginal stability bounds analytically, it is found that regions of global stability exist when $\mathrm{Mg} = 0$; or when $\mathrm{Mg} > 0$ and $\lambda < \delta^2$; or when $\mathrm{Mg} < 0$ and $1/\lambda < 1/\delta^2$.

Case II permits comparable diffusion rates of matter and momentum but insists on zero Euler number

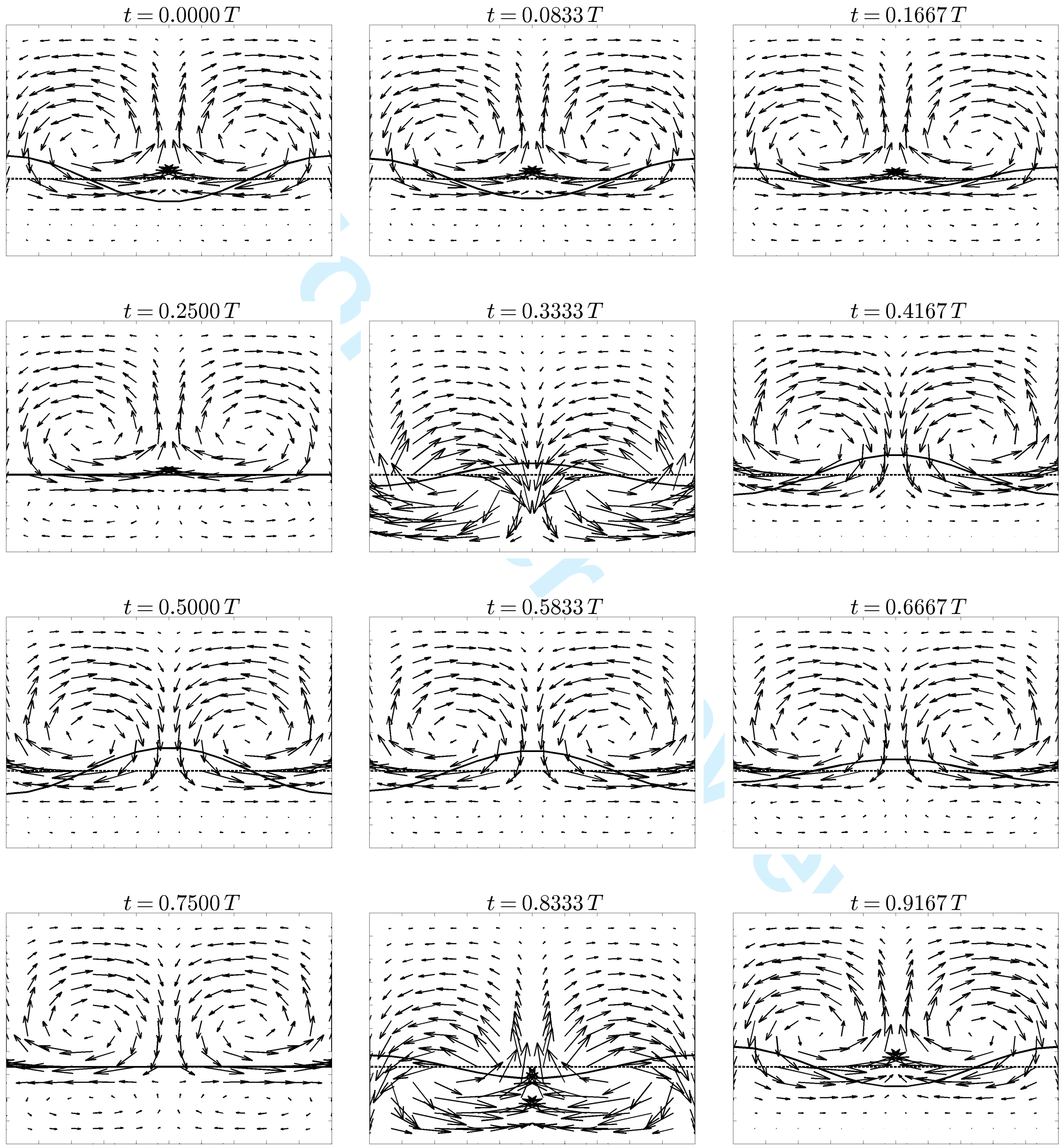

FIG. 8. Temporal evolution of flow pattern in the oscillatory state (identified in Figure 7 at parameter values, $\mathrm{Cr} = 0.1$, $\mathrm{Mg} = 10$, $\mathrm{Eu} = 0$, $\delta = 2$, $\lambda = 2$, $\Lambda = 1$ and $\Delta_\chi = 1$, at the excitation wavenumber $k = 2$. The direction field associated with the fluid velocity $\mathbf{u}(x,\ y) = u(x,\ y)\mathbf{i} + v(x,\ y)\mathbf{j}$ is plotted at time instants t expressed as fractions of the period $T = 2\pi/|\Re(\omega)|$. The superimposed lines indicate the quiescent interface position $(--)$ and the corresponding harmonic disturbance (—–) of arbitrary amplitude $(\varepsilon = 0.1)$. For illustrative purposes, the exponential temporal decay of the disturbance has been suppressed, so that $\Im(\omega)$ is artificially set to zero. Axis labels have been discarded for clarity, though the abscissa ranges over $0 \leqslant kx/\pi \leqslant 2$ and the ordinate ranges over $-1 \leqslant y \leqslant 1$ throughout (cf. Figure 5).

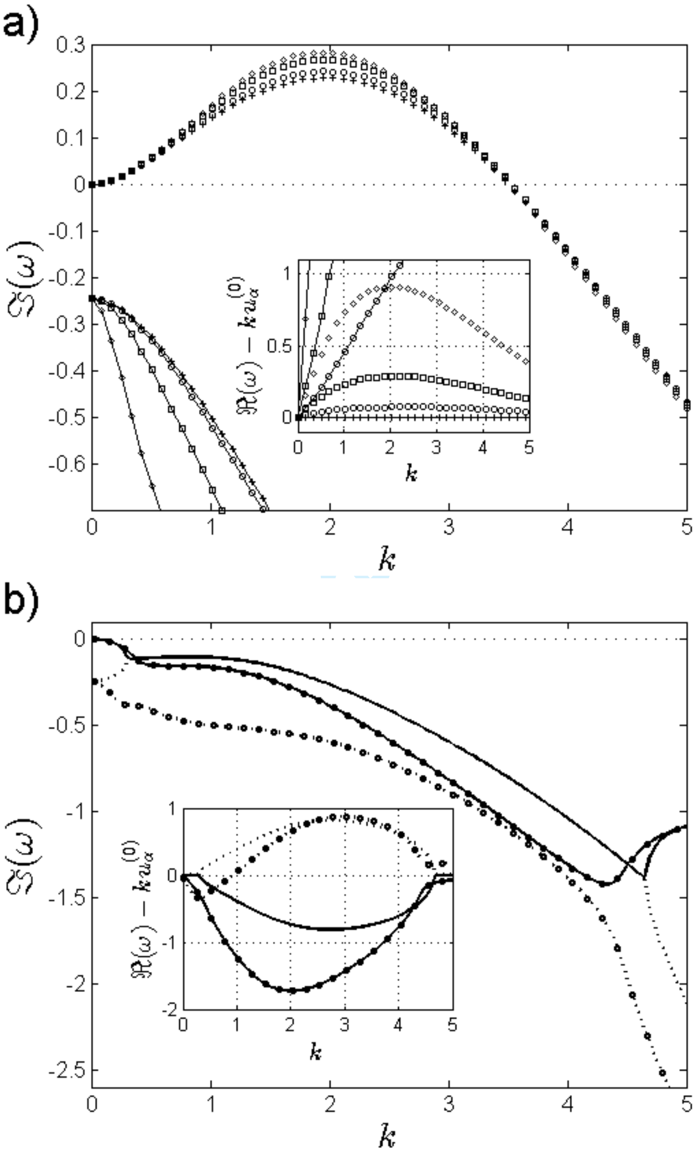

FIG. 9. Temporal frequency dispersion curves $\omega = \omega(k)$ are shown for a fluid slab of uniform mass diffusivity $(\Lambda = 1)$ and unit concentration difference on the bounding walls $\left(\Delta_\chi = 1\right)$ at crispation number $\mathrm{Cr} = 0.1$.
Panel a): the growth rate $\Im(\omega)$ is compared between Case II $(\mathrm{Eu} = 0)(+)$ and Case III with nonzero Eu set to 3(○), 10(□) and 30(◇), all obtained by the collocation method (Section 5.2). The dominant mode $(m = 1)$ is indicated by symbols alone, while the secondary mode $(m = 2)$ is denoted by symbols with solid lines. The inset shows the corresponding effective velocity $c_{\mathrm{rel}}/k = \Re(\omega) - ku_\alpha^{(0)}$ of the spatially propagating wave relative to the base state fluid speed on the interface. Other control parameters are $\lambda = 2$ and $\delta = 1/\sqrt{10} < \sqrt{\lambda}$ corresponding to an unstable response in Case I with $\mathrm{Mg} = 20$ (cf. Figure 6b).
Panel b): a similar growth rate comparison between Case II $(\mathrm{Eu} = 0)$ (no symbols) and Case III $(\mathrm{Eu} = 50)$(○) is shown. The dominant mode $(m = 1)$ is indicated by solid lines (——), while the dotted line $(\cdots)$ refers to the secondary mode $(m = 2)$. Other control parameters are $\lambda = \delta = 2$ (corresponding to a stable response in Case I) with $\mathrm{Mg} = 100$ (cf. Figure 7).

$(Eu = 0)$, thereby removing the external pressure gradient and imposing a quiescent base state. Again, the dispersion relation is obtained, but the expression appears too cumbersome for analytic presentation of the stability diagram. In this case, our treatment is formally analogous to the classical linear stability analysis of the Rayleigh–Bérnard–Marangoni problem, but considers a realistic *deformable* interface leading to more complicated boundary conditions. As with the thermocapillary problem, an extremely rich discrete spectrum of modes is obtained, and several types of mode interaction are found. In particular, exceptional points exist between stationary and oscillatory standing wave solutions, but without the additional coupling between concentration and bulk mass density (that is, the solutal equivalent of the thermal buoyancy mechanism) there is no distinction between co-rotating and counter-rotating flow cells. Rather, the oscillatory state cycles between a counter-rotating pattern of four convection cells and a two-cell pattern. Furthermore, the merging of stationary states and their collapse into an avoided crossing of modes is seen as a function of control parameters, as well as evidence of resonant energy transfer and mode switching interactions between stationary and oscillatory states. Instabilities of both Type II and Type I in the Cross & Hohenberg (1993) classification are observed.

Case III is most general in that both Cr and Eu are unrestricted. A Chebyshev collocation method is implemented to solve the transport equations obeyed by the concentration perturbations. The presence of a background flow is potentially interesting because its impact on the overall system stability is not generally obvious. A surfactant induced instability such as that found in the work of Frenkel & Halpern (2002), for instance, requires a base state shear component in order for unstable solutions to develop. In our analysis, a base-state flow was neither required for unstable solutions to exist nor were the regions of instability found to be extinguished by it. The evidence suggests that an external pressure gradient driving a base state flow generally exaggerates the response: by increasing the base flow speed, unstable growth rates are enhanced, and stable decay is suppressed. By breaking the isotropic symmetry of a quiescent base state, however, standing wave solutions are no longer possible for $\mathrm{Eu} > 0$.

At zero wavenumber, the general problem also yields to exact analysis where an infinite discrete spectrum of purely imaginary eigenvalues is determined and the response is proven to be always stable in this limit. Consequently, Type-III instabilities (Cross & Hohenberg, 1993) are precluded in this model. Furthermore, the mode spacing increases with crispation number so that only the single trivial zero frequency mode survives in the limit $\mathrm{Cr} \to \infty$, consistent with the Case I analysis.

Areas remaining open for further investigation include the following:

- the case of negligibly weak mass diffusion in both films where solute transport is entirely by fluid convection $(\mathrm{Cr} \to 0,\ 0 < \Lambda < \infty)$ (intuition and evidence (e.g. Figure 6b) suggests that instabilities are suppressed by boundary layers developing close to the interface – a matched asymptotic analysis is required to handle the change in order of the advection-diffusion equation in a non-regular limit);

- for the analogous Rayleigh–Bénard–Marangoni thermocapillary problem, the occurrence of Hopf bifurcations has been documented (Colinet & Legros, 1994) where time-dependent convection appears in a narrow transition region between stationary states. Can corresponding marginally stable bifurcation points be found in the present problem?

- in a departure from the thermocapillary analogue, the solutal Marangoni problem can consider the coupling of *many* scalar concentration fields, each with a distinct mass diffusivity in the bulk phases and a different contribution to the dilatational elasticity of the interface – can stability be modulated by tuning the adsorption of each solute type?

- what could be learned from an energy budget analysis to elucidate details of the instability mechanism (Boomkamp & Miesen, 1996; Albert & Charru, 2000; Yecko, 2008; Peng & Zhu, 2010)?
- what is the nature of the mechanism controlling the apparent transition between the appearance of two convection cells and four (see Figure 5), and how does this phenomenon relate to interfacial stability? We speculate that the interface deformation and the proximity of bounding walls are involved as recently suggested by Pozrikidis & Hill (2011).

On-going research is applying this work to exploit the capability of the Dynamic Gastric Model as a physiologically relevant screening tool for evaluating novel and existing foodstuffs, diets and pharmaceutical preparations (Rickett, 2013). This will also inform the development of more realistic prototype machines.

8. Acknowledgement

This work was partially supported by the Biotechnology and Biological Sciences Research Council through its core strategic grant to the Institute of Food Research.

9. Appendix

9.1 *General dispersion relation*

In the result (3.17) the coefficients are given by

$$\begin{aligned}
\kappa_{\mathbf{u}} = \kappa_{\mathbf{u}}^{(0)} &+ k_+^2 \Big(\big(\alpha s_1 s_{1-\alpha} - k_- s_\alpha\big) \Omega_{A2}(1) - \big(\alpha c_1 s_{1-\alpha} - k_- c_\alpha\big) \Omega_{B2}(1) \\
&\qquad - \big(s_1 s_{1-\alpha} - k_- s_\alpha\big) \Omega_{C2}(1) + \big(c_1 s_{1-\alpha} - k_- c_\alpha\big) \Omega_{D2}(1) \Big) \Lambda \\
&- k_-^2 \Big(\big(\alpha s_1 s_{1+\alpha} - k_+ s_\alpha\big) \Omega_{A1}(-1) + \big(\alpha c_1 s_{1+\alpha} + k_+ c_\alpha\big) \Omega_{B1}(-1) \\
&\qquad - \big(s_1 s_{1+\alpha} + k_+ s_\alpha\big) \Omega_{C1}(-1) - \big(c_1 s_{1+\alpha} - k_+ c_\alpha\big) \Omega_{D1}(-1) \Big) \lambda \quad ,
\end{aligned}$$

$$\begin{aligned}
\kappa_{\perp\boldsymbol{\sigma}} = \kappa_{\perp\boldsymbol{\sigma}}^{(0)} &+ \big(s_{1+\alpha}^2 - k_+^2\big) \Big(\big(\alpha s_1 s_{1-\alpha} - k_- s_\alpha\big) \Omega_{A2}(1) - \big(\alpha c_1 s_{1-\alpha} - k_- c_\alpha\big) \Omega_{B2}(1) \\
&\qquad - \big(s_1 s_{1-\alpha} - k_- s_\alpha\big) \Omega_{C2}(1) + \big(c_1 s_{1-\alpha} - k_- c_\alpha\big) \Omega_{D2}(1) \Big) \Lambda \\
&- \big(s_{1-\alpha}^2 - k_-^2\big) \Big(\big(\alpha s_1 s_{1+\alpha} - k_+ s_\alpha\big) \Omega_{A1}(-1) + \big(\alpha c_1 s_{1+\alpha} + k_+ c_\alpha\big) \Omega_{B1}(-1) \\
&\qquad - \big(s_1 s_{1+\alpha} + k_+ s_\alpha\big) \Omega_{C1}(-1) - \big(c_1 s_{1+\alpha} - k_+ c_\alpha\big) \Omega_{D1}(-1) \Big) \quad ,
\end{aligned}$$

$$\kappa_{\parallel\boldsymbol{\sigma}} = k_-^2 \big(s_{1+\alpha}^2 - k_+^2\big) \lambda - k_+^2 \big(s_{1-\alpha}^2 - k_-^2\big) \quad ,$$

$$\begin{aligned}
\kappa_\eta = \kappa_\eta^{(0)} &+ 2(c_1 s_1 - k) \Big(\big(\alpha s_1 s_{1-\alpha} + k_- s_\alpha\big) \Omega_{A1}(-1) - \big(c_1 s_{1-\alpha} + k_- c_\alpha\big) \Omega_{D1}(-1) \\
&\qquad - \big(\alpha s_1 s_{1+\alpha} + k_+ s_\alpha\big) \Lambda \Omega_{A2}(1) - \big(c_1 s_{1+\alpha} + k_+ c_\alpha\big) \Lambda \Omega_{D2}(1) \Big) \\
&+ 2(c_1 s_1 + k) \Big(\big(\alpha c_1 s_{1-\alpha} + k_- c_\alpha\big) \Omega_{B1}(-1) - \big(s_1 s_{1-\alpha} + k_- s_\alpha\big) \Omega_{C1}(-1)
\end{aligned}$$

$$
\begin{aligned}
&\qquad + \left(\alpha c_1 s_{1+\alpha} - k_+ c_\alpha\right) \Lambda \Omega_{B2}(1) + \left(s_1 s_{1+\alpha} - k_+ s_\alpha\right) \Lambda \Omega_{C2}(1)\Big) \\
&+ (\lambda - 1)\Big[2\left(c_1 s_1 - k\right)\Big(\left(\alpha s_1 s_{1-\alpha} + k_- s_\alpha\right)\Omega_{A1}(-1) - \left(c_1 s_{1-\alpha} + k_- c_\alpha\right)\Omega_{D1}(-1)\Big) \\
&\qquad + 2\left(c_1 s_1 + k\right)\Big(\left(\alpha c_1 s_{1-\alpha} + k_- c_\alpha\right)\Omega_{B1}(-1) - \left(s_1 s_{1-\alpha} + k_- s_\alpha\right)\Omega_{C1}(-1)\Big) \\
&\quad - \left(s_{1+\alpha}^2 - k_+^2\right)\Big(\left(\alpha s_1 c_{1-\alpha} + k_- c_\alpha\right)\Omega_{A2}(1) - \left(\alpha c_1 c_{1-\alpha} + k_- s_\alpha\right)\Omega_{B2}(1) \\
&\qquad - \left(s_1 c_{1-\alpha} + k_- c_\alpha\right)\Omega_{C2}(1) + \left(c_1 c_{1-\alpha} + k_- s_\alpha\right)\Omega_{D2}(1)\Big)\Lambda \\
&\quad - \left(s_{1-\alpha}^2 - k_-^2\right)\Big(\left(\alpha s_1 c_{1+\alpha} - k_+ c_\alpha\right)\Omega_{A1}(-1) - \left(\alpha c_1 c_{1+\alpha} + k_+ s_\alpha\right)\Omega_{B1}(-1) \\
&\qquad - \left(s_1 c_{1+\alpha} + k_+ c_\alpha\right)\Omega_{C1}(-1) - \left(c_1 c_{1+\alpha} - k_+ s_\alpha\right)\Omega_{D1}(-1)\Big)\Big] \ ,
\end{aligned}
\tag{9.1}
$$

where the contributions independent of the chemical fields are:

$$
\begin{aligned}
\kappa_{\mathbf{u}}^{(0)} &= -\Big(k_+^2\left(c_{1-\alpha} s_{1-\alpha} - k_-\right) + k_-^2\left(c_{1+\alpha} s_{1+\alpha} - k_+\right)\Big)\lambda \ , \\
\kappa_{\perp\boldsymbol{\sigma}}^{(0)} &= -\Big(\left(s_{1+\alpha}^2 - k_+^2\right)\left(c_{1-\alpha} s_{1-\alpha} - k_-\right)\lambda + \left(s_{1-\alpha}^2 - k_-^2\right)\left(c_{1+\alpha} s_{1+\alpha} - k_+\right)\Big) \ , \\
\kappa_{\eta}^{(0)} &= \mathscr{A}_{k,\alpha}(\lambda - 1)^2 + 2\mathscr{B}_{k,\alpha}(\lambda - 1) + \mathscr{C}_k \ ,
\end{aligned}
\tag{9.2}
$$

$$
\begin{aligned}
\mathscr{A}_{k,\alpha} &= \left(s_{1+\alpha}^2 - k_+^2\right)\left(c_{1-\alpha}^2 + k_-^2\right) \ , \\
\mathscr{B}_{k,\alpha} &= \mathscr{A}_{k,\alpha} + \left(k_+ k_-\right)^2 + \frac{1}{4}\Big(s_{2(1+\alpha)} s_{2(1-\alpha)} - \left(2k_+\right)\left(2k_-\right)\Big) \ , \\
\mathscr{C}_k &= s_2^2 - (2k)^2 \ .
\end{aligned}
$$

Coupling terms between the flow and the chemical field involve the determinant-like functions

$$
\mathscr{L}_{k,\alpha}(\Lambda) = \det \begin{pmatrix} \det\begin{pmatrix} \Psi_1(-1) & \Psi_1(\alpha) \\ \Phi_1(-1) & \Phi_1(\alpha) \end{pmatrix} & \det\begin{pmatrix} \Psi_2(1) & \Psi_2(\alpha) \\ \Phi_2(1) & \Phi_2(\alpha) \end{pmatrix} \\ \mathscr{W}\left(\Psi_1(-1),\ \Phi_1(\alpha)\right) & \Lambda\ \mathscr{W}\left(\Psi_2(1),\ \Phi_2(\alpha)\right) \end{pmatrix} \ , \tag{9.3}
$$

with $\mathscr{W}$ defined by (3.14) and

$$
\begin{aligned}
\Omega_{Xj}(y) = {} & \frac{k}{\Psi_j(y)\mathscr{L}_{k,\alpha}(\Lambda)} \det\begin{pmatrix} \Psi_{3-j}(-y) & \Psi_{3-j}(\alpha) \\ \Phi_{3-j}(-y) & \Phi_{3-j}(\alpha) \end{pmatrix} \\
& \times \det\begin{pmatrix} \det\begin{pmatrix} \Psi_j(y) & \Psi_j(\alpha) \\ \mathscr{I}_{Xj}(y) & \mathscr{I}_{Xj}(\alpha) \end{pmatrix} & \det\begin{pmatrix} \Psi_j(y) & \Psi_j(\alpha) \\ \Phi_j(y) & \Phi_j(\alpha) \end{pmatrix} \\ \mathscr{W}\left(\Psi_j(y),\ \mathscr{I}_{Xj}(\alpha)\right) & \mathscr{W}\left(\Psi_j(y),\ \Phi_j(\alpha)\right) \end{pmatrix} \ .
\end{aligned}
\tag{9.4}
$$

9.2 *Case II dispersion relation*

In the result (4.13) the coefficients are given by:

$$\kappa_{\perp\boldsymbol{\sigma}}^{(1)} = \kappa_{\perp\boldsymbol{\sigma}}^{(0)} - \mathrm{Mg}\,\mathrm{Cr}\,\frac{(1+\delta)\Lambda}{2(\delta+\Lambda)}\,\frac{1}{\mathscr{L}_{k,\alpha}^{(1)}(\Lambda)}\left(\frac{k}{\omega}\right)^{2}\times$$

$$\times\Bigg(S_{1,1+\alpha}\big(s_{1+\alpha}^{2}-k_{+}^{2}\big)\Big(K_2k_{-}\big(C_{2,1-\alpha}-c_{1-\alpha}\big)+\Big(kS_{2,1-\alpha}s_{1-\alpha}-K_2\big(C_{2,1-\alpha}c_{1-\alpha}-1\big)\Big)s_{1-\alpha}\Big)\Lambda$$

$$-S_{2,1-\alpha}\big(s_{1-\alpha}^{2}-k_{-}^{2}\big)\Big(K_1k_{+}\big(C_{1,1+\alpha}-c_{1+\alpha}\big)+\Big(kS_{1,1+\alpha}s_{1+\alpha}-K_1\big(C_{1,1+\alpha}c_{1+\alpha}-1\big)\Big)s_{1+\alpha}\Big)\Bigg)\ ,$$

$$\kappa_{\eta}^{(1)} = \kappa_{\eta}^{(0)} - \mathrm{Mg}\,\frac{(1+\delta)\Lambda}{4(\delta+\Lambda)}\,\frac{1}{\mathscr{L}_{k,\alpha}^{(1)}(\Lambda)}\left(\frac{1}{\omega}\right)\times$$

$$\times\Bigg(\big(K_1C_{1,1+\alpha}S_{2,1-\alpha}+K_2C_{2,1-\alpha}S_{1,1+\alpha}\big)\big(k_{+}^{2}s_{1-\alpha}^{2}-k_{-}^{2}s_{1+\alpha}^{2}\big)\ i$$

$$+(\lambda-1)\Bigg(2kS_{1,1+\alpha}S_{2,1-\alpha}\Big(k_{+}^{2}\big(c_{1-\alpha}s_{1-\alpha}+k_{-}\big)+k_{-}^{2}\big(c_{1+\alpha}s_{1+\alpha}+k_{+}\big)\Big)$$

$$-\big(K_1C_{1,1+\alpha}S_{2,1-\alpha}+K_2C_{2,1-\alpha}S_{1,1+\alpha}\big)k_{-}^{2}\big(s_{1+\alpha}^{2}-k_{+}^{2}\big)\Big)\ i\Bigg)$$

$$-\mathrm{Mg}\,\mathrm{Cr}\,\frac{(1+\delta)\Lambda}{2(\delta+\Lambda)}\,\frac{1}{\mathscr{L}_{k,\alpha}^{(1)}(\Lambda)}\left(\frac{k}{\omega^{2}}\right)\times$$

$$\times\Bigg(2K_2S_{1,1+\alpha}\bigg(\Big(k\big(C_{2,1-\alpha}c_{\alpha}-c_1\big)+K_2S_{2,1-\alpha}s_{\alpha}\Big)\big(c_1s_{1+\alpha}+k_{+}c_{\alpha}\big)\big(c_1s_1-k\big)$$

$$-\Big(k\big(C_{2,1-\alpha}s_{\alpha}-s_1\big)+K_2S_{2,1-\alpha}c_{\alpha}\Big)\big(s_1s_{1+\alpha}-k_{+}s_{\alpha}\big)\big(c_1s_1+k\big)\bigg)\Lambda$$

$$-2K_1S_{2,1-\alpha}\bigg(\Big(k\big(C_{1,1+\alpha}c_{\alpha}-c_1\big)-K_1S_{1,1+\alpha}s_{\alpha}\Big)\big(c_1s_{1-\alpha}+k_{-}c_{\alpha}\big)\big(c_1s_1-k\big)$$

$$+\Big(k\big(C_{1,1+\alpha}s_{\alpha}+s_1\big)-K_1S_{1,1+\alpha}c_{\alpha}\Big)\big(s_1s_{1-\alpha}+k_{-}s_{\alpha}\big)\big(c_1s_1+k\big)\bigg)$$

$$+(\lambda-1)\bigg(K_2S_{1,1+\alpha}\big(s_{1+\alpha}^{2}-k_{+}^{2}\big)\times$$

$$\times\Big(\big(kC_{2,1-\alpha}c_{1-\alpha}-K_2S_{2,1-\alpha}s_{1-\alpha}-k\big)c_{1-\alpha}+k_{-}\big(ks_{1-\alpha}-K_2S_{2,1-\alpha}\big)\Big)\Lambda$$

$$+K_1S_{2,1-\alpha}\big(s_{1-\alpha}^{2}-k_{-}^{2}\big)\times$$

$$\times\Big(\big(kC_{1,1+\alpha}c_{1+\alpha}-K_1S_{1,1+\alpha}s_{1+\alpha}-k\big)c_{1+\alpha}+k_+\big(ks_{1+\alpha}-K_1S_{1,1+\alpha}\big)\Big)$$

$$+K_1S_{2,1-\alpha}\times$$

$$\times\Big(2k^2k_-\big(C_{1,1+\alpha}-c_{1+\alpha}\big)k_+s_{1-\alpha}+\big(kC_{1,1+\alpha}c_{1-\alpha}+K_1S_{1,1+\alpha}s_{1-\alpha}-kc_2\big)k_+s_{1-\alpha}$$

$$-\big(kC_{1,1+\alpha}c_{1+\alpha}-K_1S_{1,1+\alpha}s_{1+\alpha}-k\big)\big(s_2s_{1-\alpha}+k_-s_{1+\alpha}\big)\Big)\Big)\Big) \quad . \qquad (9.5)$$

9.3 *Proof* $\kappa_\eta^{(0)} > 0$

First note the obvious fact, if a, b, $c > 0$ then $a\lambda^2+2b\lambda+c>0$ for all $\lambda>0$. It follows that, if $b>a>0$ and $a-2b+c>0$ then

$$a\lambda^2+2(b-a)\lambda+a-2b+c=a(\lambda-1)^2+2b(\lambda-1)+c>0 \ \text{ for all } \ \lambda>0 \ . \qquad (9.6)$$

For the "jump" term J_η, the coefficient $\kappa_\eta^{(0)}$ is a quadratic function of $(\lambda-1)$ thus

$$\kappa_\eta^{(0)}=\mathscr{A}_{k,\alpha}(\lambda-1)^2+2\mathscr{B}_{k,\alpha}(\lambda-1)+\mathscr{C}_k \quad , \qquad (9.7)$$

where

$$\begin{aligned}\mathscr{A}_{k,\alpha}&=\big(s_{1+\alpha}^2-k_+^2\big)\big(c_{1-\alpha}^2+k_-^2\big) \ ,\\ \mathscr{B}_{k,\alpha}&=\mathscr{A}_{k,\alpha}+\big(k_+k_-\big)^2+\frac{1}{4}\Big(s_{2(1+\alpha)}s_{2(1-\alpha)}-\big(2k_+\big)\big(2k_-\big)\Big) \ ,\\ \mathscr{C}_k&=s_2^2-(2k)^2 \ .\end{aligned} \qquad (9.8)$$

By virtue of the fact that $\xi>0$ implies $\sinh(\xi)>\xi$, we immediately observe

$$\mathscr{B}_{k,\alpha}>\mathscr{A}_{k,\alpha}>0 \ , \ \mathscr{C}_k>0 \ , \qquad (9.9)$$

for all physically relevant parameter values. Furthermore we find

$$\mathscr{A}_{k,\alpha}-2\mathscr{B}_{k,\alpha}+\mathscr{C}_k=\big(c_{1+\alpha}^2+k_+^2\big)\big(s_{1-\alpha}^2-k_-^2\big)>0 \ . \qquad (9.10)$$

So (9.7) satisfies the conditions for inequality (9.6). Hence, $\kappa_\eta^{(0)}>0$ for all $\lambda>0$ as claimed.

9.4 *Equivalence of (6.2) with (23) of Smith (1966)*

Re-casting Smith's result (equation (23) of Smith (1966), see also equation (40) of Merkt et al. (2005) and equation (2.37) of Nepomnyashchy et al. (2006)) in our notation obtains

$$-\frac{\mathrm{Mg}_0}{\mathrm{Cr}}\times\frac{4G_{\chi,1}}{(1+\delta)^2\Delta_\chi}\left[1-\frac{1}{\Lambda}\left(\frac{g_{1+\alpha}s_{1+\alpha}\big(k_-^3c_{1-\alpha}-s_{1-\alpha}^3\big)}{g_{1-\alpha}s_{1-\alpha}\big(k_+^3c_{1+\alpha}-s_{1+\alpha}^3\big)}\right)\right.$$

$$- \frac{\mathrm{Cr}(1+\delta)^3}{(\mathrm{Bo}+k^2)} \left(\frac{k_+^3 c_{1+\alpha} s_{1+\alpha}^2}{k_+^3 c_{1+\alpha} - s_{1+\alpha}^3} \right) \left(1 + \frac{c_{1-\alpha} s_{1+\alpha}}{c_{1+\alpha} s_{1-\alpha}} \right) \left(1 - \lambda_0 \, \frac{g_{1+\alpha} s_{1-\alpha}^2}{g_{1-\alpha} s_{1+\alpha}^2} - (1-\lambda_0) \frac{g_{1+\alpha}}{s_{1+\alpha}^2} \right) \Bigg]$$

$$= -4 \left(\frac{k_+^2 c_{1+\alpha} \mathscr{D} g_{1+\alpha}}{k_+^3 c_{1+\alpha} - s_{1+\alpha}^3} \right) \left(1 + \Lambda \, \frac{c_{1-\alpha} s_{1+\alpha}}{c_{1+\alpha} s_{1-\alpha}} \right) \left(1 + \lambda_0 \, \frac{g_{1+\alpha} \mathscr{D} g_{1-\alpha}}{g_{1-\alpha} \mathscr{D} g_{1+\alpha}} \right) \quad , \qquad (9.11)$$

where $\mathrm{Bo} = (\tilde{\rho}_1 - \tilde{\rho}_2)\tilde{g}\tilde{h}^2/\tilde{\gamma}_0$ is the Bond number that measures the relative importance of capillary and gravitational forces (with acceleration $\tilde{g}$). By ignoring mass density stratification to set $\mathrm{Bo} = 0$ and taking the limit $\mathrm{Cr} \to \infty$ in accord with our Case I, then (9.11) becomes

$$\mathrm{Mg}_0 \times \frac{4G_{\chi,1} k_+ s_2}{(1+\delta)\Delta_\chi} \left[s_{1+\alpha}^2 - g_{1+\alpha} + \lambda_0 g_{1+\alpha} \left(1 - \frac{s_{1-\alpha}^2}{g_{1-\alpha}} \right) \right] = \mathrm{Mg}_0 \times \frac{2\Lambda k_+ s_2}{(\delta+\Lambda)} \left(k_+^2 - \lambda_0 k_-^2 \, \frac{g_{1+\alpha}}{g_{1-\alpha}} \right)$$

$$= -k_+^2 \mathscr{D} g_{1+\alpha} \left(c_{1+\alpha} s_{1-\alpha} + \Lambda c_{1-\alpha} s_{1+\alpha} \right) \left(1 + \lambda_0 \, \frac{g_{1+\alpha} \mathscr{D} g_{1-\alpha}}{g_{1-\alpha} \mathscr{D} g_{1+\alpha}} \right) \quad , \qquad (9.12)$$

or

$$\mathrm{Mg}_0 = \frac{(\delta+\Lambda)\left(c_{1+\alpha} s_{1-\alpha} + \Lambda c_{1-\alpha} s_{1+\alpha} \right)}{2\Lambda k_+ s_2} \left(\frac{g_{1+\alpha} \mathscr{D} g_{1-\alpha} \lambda_0 + g_{1-\alpha} \mathscr{D} g_{1+\alpha}}{g_{1+\alpha} \delta^2 \lambda_0 - g_{1-\alpha}} \right) \quad , \qquad (9.13)$$

and using (4.8) recovers (6.2) as required.

9.5 *Proof in Case I* $\Re(\omega) \geqslant 0$

The argument follows the same structure as Section 9.3. Recall, in case $\mathrm{Cr} \to \infty$, the real part of the temporal frequency may be written proportional to a quadratic function in $(\lambda - 1)$ thus

$$\Re(\omega) = \frac{\mathrm{Eu}}{\kappa_\eta^{(0)} (1+\delta)(\delta+\lambda)} \left(\mathscr{A}'_{k,\alpha} (\lambda-1)^2 + 2\mathscr{B}'_{k,\alpha} (\lambda-1) + \mathscr{C}'_k \right) \quad , \qquad (9.14)$$

where

$$\mathscr{A}'_{k,\alpha} = \mathscr{U}_{k,\alpha} + 2k\delta\mathscr{A}_{k,\alpha} \quad , \quad \mathscr{B}'_{k,\alpha} = \tfrac{1}{2}\left(1-\delta^2\right)\mathscr{U}_{k,\alpha} + 2k\delta\mathscr{B}_{k,\alpha} \quad , \quad \mathscr{C}'_k = 2k\delta\mathscr{C}_k \quad ,$$
$$\text{with} \qquad \mathscr{U}_{k,\alpha} = k_+^2 \left(c_{1-\alpha} s_{1-\alpha} - k_- \right) + k_-^2 \left(c_{1+\alpha} s_{1+\alpha} - k_+ \right) \quad . \qquad (9.15)$$

Evidently, $\mathscr{U}_{k,\alpha} > 0$ and we find

$$k_+^2 \left(\mathscr{B}'_{k,\alpha} - \mathscr{A}'_{k,\alpha} \right) = k_+ k_- \left(\mathscr{U}_{k,\alpha} + \left(k_+ + k_-\right) \left(\left(k_+ k_-\right)^2 + \left(c_{1-\alpha} s_{1-\alpha} - k_- \right) \left(c_{1+\alpha} s_{1+\alpha} - k_+ \right) \right) \right)$$
$$+ \left(k_+ k_-\right)^2 \left(k_+ + k_-\right) \left(k_+ - k_-\right)^2 \sum_{n=0}^{\infty} \frac{2^{2n+1}}{(2n+1)!} \sum_{m=0}^{2n} k_+^{2n-m} k_-^m$$
$$> 0 \quad , \qquad (9.16)$$

whence

$$\mathscr{B}'_{k,\alpha} > \mathscr{A}'_{k,\alpha} > 0 \quad . \qquad (9.17)$$

Furthermore,

$$\mathscr{A}'_{k,\alpha} - 2\mathscr{B}'_{k,\alpha} + \mathscr{C}'_k = \delta^2 \mathscr{U}_{k,\alpha} + 2k\delta \left(\mathscr{A}_{k,\alpha} - 2\mathscr{B}_{k,\alpha} + \mathscr{C}_k \right) > 0 \quad , \qquad (9.18)$$

where the result of Section 9.3 has been used. Hence, as claimed $\mathrm{Eu} > 0$ implies $\Re(\omega) > 0$ for all $\lambda > 0$, while $\Re(\omega) = 0$ if $\mathrm{Eu} = 0$.

9.6 *Proof* $k=0$ *implies* $\Re(\omega)=0$ *and* $\Im(\omega)\leqslant 0$

From the dispersion relation (5.18), we will deduce restrictions on the temporal frequency ω in the situation of vanishing wavenumber ($k=0$). First recall the definitions (5.19):

$$\begin{gathered} h_- = \frac{2\delta}{(1+\delta)\sqrt{\Lambda}} = \frac{1-\alpha}{\sqrt{\Lambda}} > 0 \ ; \ h_+ = \frac{2}{1+\delta} = 1+\alpha > 0 \\ \text{and} \quad K_0 = \sqrt{-i\omega/\mathrm{Cr}} = \Re\big(K_0\big) + i\,\Im\big(K_0\big) \in \mathbb{C} \end{gathered} \tag{9.19}$$

In particular,

$$\Re\big(K_0\big) = \sqrt{\frac{|\omega| + \Im(\omega)}{2\,\mathrm{Cr}}} \ , \tag{9.20}$$

so that

$$\begin{gathered} \Re\big(K_0\big) = 0 \quad \Rightarrow \quad |\omega| + \Im(\omega) = 0 \\ \Rightarrow \quad \Im(\omega) \leqslant 0 \qquad \text{and} \qquad \big(\Im(\omega)\big)^2 = \big(\Re(\omega)\big)^2 + \big(\Im(\omega)\big)^2 \quad \Rightarrow \quad \Re(\omega) = 0 \ , \end{gathered} \tag{9.21}$$

since $|\omega| \geqslant 0$. Thus, it suffices to show that the dispersion relation (5.18) implies $\Re\big(K_0\big) = 0$.

For the sake of contradiction, suppose that $\Re\big(K_0\big) \neq 0$ while (5.18) holds. Now define

$$\hat{\mathscr{L}}^{(1)}_{0,\alpha} = \frac{\mathscr{L}^{(1)}_{0,\alpha}}{K_0 \cosh\big(\Re(K_0)h_-\big)\cosh\big(\Re(K_0)h_+\big)} \ , \tag{9.22}$$

so that

$$\begin{aligned} \Re\big(\hat{\mathscr{L}}^{(1)}_{0,\alpha}\big) &= T_-\big(c_-c_+ - s_-s_+\sqrt{\Lambda}\big) + T_+\big(c_-c_+\sqrt{\Lambda} - s_-s_+\big) \ , \\ \Im\big(\hat{\mathscr{L}}^{(1)}_{0,\alpha}\big) &= T_-T_+\big(c_+s_-\sqrt{\Lambda} + c_-s_+\big) + \big(c_-s_+\sqrt{\Lambda} + c_+s_-\big) \ , \end{aligned} \tag{9.23}$$

where

$$T_\pm = \tanh\big(\Re(K_0)h_\pm\big) \ , \ c_\pm = \cos\big(\Im(K_0)h_\pm\big) \ , \ s_\pm = \sin\big(\Im(K_0)h_\pm\big) \ . \tag{9.24}$$

Since $\Re(K_0) \neq 0$ implies $T_-T_+ > 0$, then $\hat{\mathscr{L}}^{(1)}_{0,\alpha} = 0$ demands the bracketed factors in (9.23) either both vanish or are non-zero with opposite sign, so that

$$\begin{aligned} \Re\big(\hat{\mathscr{L}}^{(1)}_{0,\alpha}\big) = 0 \quad &\Rightarrow \quad \big(c_-c_+ - s_-s_+\sqrt{\Lambda}\big)\big(c_-c_+\sqrt{\Lambda} - s_-s_+\big) \leqslant 0 \ , \\ &\Rightarrow \quad 0 \leqslant \frac{\sqrt{\Lambda}}{1+\Lambda}\Big(\big(c_-c_+\big)^2 + \big(s_-s_+\big)^2\Big) \leqslant c_-s_-c_+s_+ \ , \end{aligned} \tag{9.25}$$

$$\begin{aligned} \Im\big(\hat{\mathscr{L}}^{(1)}_{0,\alpha}\big) = 0 \quad &\Rightarrow \quad \big(c_+s_-\sqrt{\Lambda} + c_-s_+\big)\big(c_-s_+\sqrt{\Lambda} + c_+s_-\big) \leqslant 0 \ , \\ &\Rightarrow \quad c_-s_-c_+s_+ \leqslant -\frac{\sqrt{\Lambda}}{1+\Lambda}\Big(\big(c_-s_+\big)^2 + \big(c_+s_-\big)^2\Big) \leqslant 0 \ . \end{aligned} \tag{9.26}$$

Together, the conditions (9.25) and (9.26) require

$$c_-s_-c_+s_+ = 0 \ . \tag{9.27}$$

Now consider the magnitude

$$\begin{aligned} \left|\hat{\mathscr{L}}^{(1)}_{0,\alpha}\right|^2 &= \left(c_-c_+\right)^2\left(T_- + T_+\sqrt{\Lambda}\right)^2 + \left(c_-s_+\right)^2\left(T_-T_+ + \sqrt{\Lambda}\right)^2 \\ &\quad + \left(c_+s_-\right)^2\left(T_-T_+\sqrt{\Lambda} + 1\right)^2 + \left(s_-s_+\right)^2\left(T_-\sqrt{\Lambda} + T_+\right)^2 \ , \end{aligned} \tag{9.28}$$

where (9.27) has been used, and observe that $\left|\hat{\mathscr{L}}^{(1)}_{0,\alpha}\right| = 0$ requires

$$c_-c_+ = c_-s_+ = c_+s_- = s_-s_+ = 0 \ , \tag{9.29}$$

again because $T_-T_+ > 0$. Finally, define

$$\Delta = \Im\left(K_0\right)\ \left(h_+ - h_-\right)\ \in\ \mathbb{R}\ , \tag{9.30}$$

and deduce that

$$\begin{aligned} c_-c_+ = s_-s_+ = 0 \quad &\Rightarrow \quad \cos\Delta = 0\ , \\ c_-s_+ = c_+s_- = 0 \quad &\Rightarrow \quad \sin\Delta = 0\ . \end{aligned} \tag{9.31}$$

But there is no real number Δ simultaneously satisfying both conditions (9.31). Hence, by contradiction, we conclude $\Re\left(K_0\right) = 0$ as required.

REFERENCES

Abramowitz, M. & Stegun, I. A. (1965) *Handbook of Mathematical Functions*. Dover Publications, New York, ninth edition.

Albert, F. & Charru, F. (2000) Small Reynolds number instabilities in two-layer Couette flow. *Eur. J. Mech. B: Fluids*, **19**, 229–252.

Andereck, C. D., Colovas, P. W., Degen, M. M. & Renardy, Y. Y. (1998) Instabilities in two layer Rayleigh–Bénard convection: overview and outlook. *Int. J. Eng. Sci.*, **36**, 1451–1470.

Anderson, D. M., McFadden, G. B. & Wheeler, A. A. (1998) Diffuse-interface methods in fluids mechanics. *Annu. Rev. Fluid Mech.*, **30**, 139-165.

Anturkar, N. R., Papanastasiou, T. C. & Wilkes, J. O. (1990) Linear stability analysis of multilayer plane Poiseuille flow. *Phys. Fluids A*, **2**, 530–541.

Betcke, T. & Trefethen, L. N. (2004) Computations of eigenvalue avoidance in planar domains. *Manchester Inst. Math. Sci., MIMS EPrint*, 2006.366.

Blyth, M. G. & Pozrikidis, C. (2004a) Effect of surfactants on the stability of two-layer channel flow. *J. Fluid Mech.*, **505**, 59–86.

Blyth, M. G. & Pozrikidis, C. (2004b) Effect of surfactant on the stability of film flow down an inclined plane *J. Fluid Mech.*, **521**, 241–250.

Blyth, M. G. & Pozrikidis, C. (2004c) Effect of inertia on the Marangoni instability of two-layer channel flow, part II: normal-mode analysis. *J. Eng. Math.*, **50**, 329–341.

Bodenschatz, E., Pesch, W. & Ahlers, G. (2000) Recent developments in Rayleigh–Bénard convection. *Ann. Rev. Fluid Mech.*, **32**, 709–778.

Boomkamp, P. A. M. & Miesen, R. H. M. (1996) Classification of instabilities in parallel two-phase flow. *Int. J. Multiphase Flow*, **22**, S67–S88.

Braverman, L. M., Eckert, K., Nepomnyashchy, A. A., Simanovskii, I. B. & Thess, A. (2000) Convection in two-layer systems with an anomalous thermocapillary effect. *Phys. Rev. E*, **62**, 3619–3631.

Cartwright, J. H. E., Gouillart, E., Piro, N., Piro, O. & Tuval, I. (2012) Geometric mixing. `http://arxiv.org/abs/1206.6894`.

Charru, F. (2011) *Hydrodynamic Instabilities*. Cambridge University Press, Cambridge.

Charru, F. & Hinch, E. J. (2000) 'Phase diagram' of interfacial instabilities in a two-layer Couette flow and mechanism of the long-wave instability. *J. Fluid Mech.*, **414**, 195–223.

Chessa, S., Huatan, H., Levina, M., Mehta, R. Y., Ferrizzi, D. & Rajabi-Siahboomi, A. R. (2014) Application of the Dynamic Gastric Model to evaluate the effect of food on the drug release characteristics of a hydrophilic matrix formulation. *Int. J. Pharmaceutics*, **466**, 359-367.

Craster, R. V. & Matar, O. K. (2009) Dynamics and stability of thin liquid films. *Rev. Mod. Phys.*, **81**, 1131–1198.

Colinet, P. & Legros, J. C. (1994) On the Hopf bifurcation occurring in the two-layer Rayleigh–Bénard convective instability. *Phys. Fluids*, **6**, 2631–2639.

Coward, A. V., Renardy, Y. Y., Renardy, M. & Richards, J. R. (1997) Temporal evolution of periodic disturbances in two-layer Couette flow. *J. Comp. Phys.*, **132**, 346–361.

Cross, M. & Greenside, H. (2009) *Pattern Formation and Dynamics in Nonequilibrium Systems*. Cambridge University Press, Cambridge.

Cross, M. C. & Hohenberg, P. C. (1993) Pattern formation outside of equilibrium. *Rev. Mod. Phys.*, **65**, 851–1112.

Drazin, P. G. (2002) *Introduction to Hydrodynamic Stability*. Cambridge University Press, Cambridge.

Drazin, P. G. & Reid, W. H. (2004) *Hydrodynamic Stability*. Cambridge University Press, Cambridge, second edition.

Edwards, D. A., Brenner, H. & Wasan, D. T. (1991) *Interfacial Transport Processes and Rheology*. Butterworth-Heinemann, Boston.

Fan, J.-Y. (2003) A modified Levenberg-Marquardt algorithm for singular system of nonlinear equations. *J. Comp. Math.*, **21**, 625–636.

Frenkel, A. L. & Halpern, D. (2002) Stokes-flow instability due to interfacial surfactant. *Phys. Fluids*, **14**, L45–L48.

Frenkel, A. L. & Halpern, D. (2005) Effect of inertia on the insoluble-surfactant instability of a shear flow. *Phys. Rev. E*, **71**, 016302, 1–10.

Gao, P. & Lu, X.-Y. (2007) Effect of surfactants on the inertialess instability of a two-layer film flow. *J. Fluid Mech.*, **591**, 495–507.

Gottlieb, D. & Orszag, S. A. (1977) *Numerical Analysis of Spectral Methods: Theory and Applications*. SIAM, Bristol.

Halpern, D. & Frenkel, A. L. (2003) Destabilization of a creeping flow by interfacial surfactant: linear theory extended to all wavenumbers. *J. Fluid Mech.*, **485**, 191–220.

Hernández, E., Jáuregui, A. & Mondragón, A. (2003) Unfolding a degeneracy point: crossings and anticrossings of unbound states in parameter space. *Rev. Mex. Fis.*, **49**, 60–72.

Hinch, E. J. (1984) A note on the mechanism of the instability at the interface between two shearing fluids. *J. Fluid Mech.*, **144**, 463–465.

Hooper, A. P. (1985) Long-wave instability at the interface between two viscous fluids: thin layer effects. *Phys. Fluids*, **28**, 1613–1618.

Hooper, A. P. & Boyd, W. G. C. (1983) Shear-flow instability at the interface between two viscous fluids. *J. Fluid Mech.*, **128**, 507–528.

Johnson, D. & Narayanan, R. (1997) Geometric effects on convective coupling and interfacial structures in bilayer convection. *Phys. Rev. E*, **56**, 5462–5472.

Joseph, D. D., Bai, R., Chen, K. P.& Renardy, Y. Y. (1997) Core-annular flows. *Annu. Rev. Fluid Mech.*, **29**, 65–90.

Kato, T. (1980) *Perturbation Theory for Linear Operators*. Springer-Verlag, Berlin, second edition.

Kong, F. & Singh, R. P. (2008) Disintegration of solid foods in human stomach. *J. Food Sci.*, **73**, R67–R80.

Koschmieder, E. L. (1974) Bénard convection. *Adv. Chem. Phys.*, **26**, 177–212.

Lax, P. D. (2007) *Linear Algebra and its Applications*. Wiley and Sons, New York, second edition.

Li, X. & Pozrikidis, C. (1997) The effect of surfactants on drop deformation and on the rheology of dilute emulsions in Stokes flow. *J. Fluid Mech.*, **341**, 165–194.

Li, J. & Renardy, Y. (2000) Numerical study of flows of two immiscible liquids at low Reynolds number. *SIAM Review*, **42**, 417–439.

Marciani, L., Gowland, P. A., Spiller, R. C., Manoj, P., Moore, R. J., Young, P. & Fillery-Travis A. J. (2001) Effect of meal viscosity and nutrients on satiety, intragastric dilution, and emptying assessed by MRI. *Am. J. Physiol. Gastrointest. Liver Physiol.*, **280**, G1227-G1233.

Marciani, L., Wickham, M. S. J., Bush, D., Faulks, R., Wright, J., Fillery-Travis, A. J., Spiller, R. C. & Gowland, P. A. (2006) Magnetic resonance imaging of the behaviour of oil-in-water emulsions in the gastric lumen of man. *Brit. J. Nutrition*, **95**, 331–339.

Marciani, L., Faulks, R., Wickham, M. S. J., Bush, D., Pick, B., Wright, J., Cox, E. F., Fillery-Travis, A. J., Gowland, P. A. & Spiller, R. C. (2009) Effect of intragastric acid stability of fat emulsions on gastric emptying, plasma lipid profile and postprandial satiety. *Brit. J. Nutrition*, **101**, 919–928.

MATLAB (2013) *Version R2013a (8.1.0.604)*. The Mathworks Inc., Natick, Massachusetts.

Mercuri, A., Passalacqua, A., Wickham, M. S. J., Faulks, R. M., Craig, D. Q. M. & Barker, S. (2011) The effect of composition and gastric conditions on the self-emulsification process of ibuprofen-loaded self-emulsifying drug delivery systems: a microscopic and Dynamic Gastric Model study. *Pharm. Res.*, **28**, 1540–1551.

Merkt, D., Pototsky, A., Bestehorn, M. & Thiele, U. (2005) Long-wave theory of bounded two-layer films with a free liquid-liquid interface: Short- and long-time evolution. *Phys. Fluids*, **17**, 064104.

Nepomnyashchy, A., Simanovskii, I. & Legros, J. C. (2006) *Interfacial Convection in Multilayer Systems* Springer-Verlag, New York.

Normand, C., Pomeau, Y. & Velarde, M. G. (1977) Convective instability: a physicist's approach. *Rev. Mod. Phys.*, **49**, 581–624.

Oron, A., Davis, S. H. & Bankoff, S. G. (1997) Long-scale evolution of thin liquid films. *Rev. Mod. Phys.*, **69**, 931–980.

Pal, A., Brasseur, J. G. & Abrahamsson, B. (2007) A stomach road or "Magenstrasse" for gastric emptying. *J. Biomech.*, **40**, 1202–1210.

Palmer, H. J. & Berg, J. C. (1972) Hydrodynamic stability of surfactant solutions heated from below. *J. Fluid Mech.*, **51**, 385–402.

Peng, J. & Zhu, K.-Q. (2010) Linear instability of two-fluid Taylor–Couette flow in the presence of surfactant. *J. Fluid Mech.*, **651**, 357–385.

Pozrikidis, C. (1997) Instability of two-layer creeping flow in a channel with parallel-sided walls. *J. Fluid Mech.*, **351**, 139–165.

Pozrikidis, C. (2004) Effect of inertia on the Marangoni instability of two-layer channel flow, part I: numerical simulations. *J. Eng. Math.*, **50**, 311–327.

Pozrikidis, C. & Hill, A. I. (2011) Surfactant-induced instability of a sheared liquid layer. *IMA J. Appl. Math.*, **76**, 859–875.

Rasenat, S., Busse, F. H. & Rehberg, I. (1989) A theoretical and experimental study of double-layer convection. *J. Fluid Mech.*, **199**, 519–540.

Reichenbach, J. & Linde, H. (1981) Linear perturbation analysis of surface-tension-driven convection at a plane interface (Marangoni instability). *J. Coll. Interface Sci.*, **84**, 433–443.

Renardy, Y. (1987) The thin-layer effect and interfacial stability in a two-layer Couette flow with similar liquids. *Phys. Fluids*, **30**, 1627–1637.

Renardy, Y. (1987) Viscosity and density stratification in vertical Poiseuille flow. *Phys. Fluids*, **30**, 1638–1648.

Rickett, L. (2013) *A Mathematical Analysis of Digestive Processes in a Model Stomach*. PhD thesis, University of East Anglia.

Sahu, K. C., Ding, H., Valluri, P. & Matar, O. K. (2009a) Linear stability analysis and numerical simulation of miscible two-layer channel flow. *Phys. Fluids*, **21**, 042104, 1–18.

Sahu, K. C., Ding, H., Valluri, P. & Matar, O. K. (2009b) Pressure-driven miscible two-fluid channel flow with density gradients. *Phys. Fluids*, **21**, 043603, 1–10.

Schmid, P. J. & Henningson, D. S. (2001) *Stability and Transition in Shear Flows*. Springer Verlag, New York.

Seyranian, A. P., Kirillov, O. N. & Mailybaev, A. A. (2005) Coupling of eigenvalues of complex matrices at diabolic and exceptional points. *J. Phys. A.: Math. Grn.*, **38**, 1723–1740.

Slavtchev, S., Hennenberg, M., Legros, J.-C. & Lebon, G. (1998) Stationary solutal Marangoni instability in a two-layer system. *J. Coll. Interface Sci.*, **203**, 354–368.

Slavtchev, S., Kalitzova-Kurteva, P. & Mendes, M. A. (2006) Marangoni instability of liquid-liquid systems with a surface-active solute. *Coll. Surfaces A: Physiochem. Eng. Aspects*, **282-283**, 37–49.

Smith, K. A. (1996) On convective instability induced by surface-tension gradients. *J. Fluid Mech.*, **24**, 401–414.

Talon, L. & Meiburg, E. (2011) Plane Poiseuille flow of miscible layers with different viscosities: instabilities in the Stokes flow regime. *J. Fluid Mech.*, **686**, 484–506.

Tavener, S. J. & Cliffe, K. A. (2002) Two-fluid Marangoni-Bénard convection with a deformable interface. *J. Comp. Phys.*, **182**, 277–300.

Thiffeault, J.-L., Gouillart, E. & Dauchot, O. (2011) Moving walls accelerate mixing. *Phys. Rev. E*, **84**, 036313.

Wickham, M. J. S., Faulks, R. M., Mann, J. & Mandalari G. (2012) The design, operation, and application of a Dynamic Gastric Model. *Dissolution Tech.*, **19**, 15–22.

Yecko, P. (2008) Disturbance growth in two-fluid channel flow: the role of capillarity. *Int. J. Multiphase Flow*, **34**, 272–282.

Yih, C.-S. (1967) Instability due to viscosity stratification. *J. Fluid Mech.*, **27**, 337–352.

Zeren, R. W. & Reynolds, W. C. (1972) Thermal instabilities in two-fluid horizontal layers. *J. Fluid Mech.*, **53**, 305–327.

Zhao, A. X., Wagner, C., Narayanan, R. & Friedrich, R. (1995) Bilayer Rayleigh-Marangoni convection: transitions in flow structures at the interface. *Proc. Roy. Soc. Lond. A*, **451**, 487–502.

List of Figures

List of Tables